SYNTHESIS AND CHARACTERIZATION OF GEOPOLYMERS USING LOCALLY AVAILABLE FLY ASHES

by

SHIXIN ZENG

JIALAI WANG, COMMITTEE CHAIR

SRIRAM AALETI
MARK E. BARKEY
KENNETH J. FRIDLEY
JAMES A. RICHARDSON

A DISSERTATION

Submitted in partial fulfillment of the requirements
for the degree of Doctor of Philosophy
in the Department of Civil, Construction and Environmental Engineering
in the Graduate School of
The University of Alabama

TUSCALOOSA, ALABAMA

2014

ABSTRACT

Geopolymer can be synthesized using industrial wastes such as fly ash, making it a promising material to replace Ordinary Portland Cement (OPC) as a green binder for concretes. In this study, four locally available fly ashes were used to synthesize geopolymers. These fly ashes were carefully selected to include both the high calcium and low calcium fly ashes. Two of the fly ashes have very similar chemical compositions. Comprehensive experimental programs have been carried out to characterize these fly ashes, to examine the critical factors affecting the mechanical properties of geopolymers, and to evaluate the potentials of these fly ashes as source materials for geopolymers. Testing results show all these fly ashes can be used to synthesize geopolymer. Among them, the fly ash from Gaston was found to be the most suitable source material for geopolymer. Fracture behavior of the produced geopolymer mortar was studied using splitting wedge testing together with digital image correlation technique. The measured full-field displacement clearly shows that a fracture process zone (FPZ) exists ahead of the major crack, suggesting that the fracture of the geopolymer mortar follows a nonlinear behavior. The bi-linear constitutive law of the FPZ was then obtained through an inverse analysis. To gain insight into the geopolymerization process, the electrical properties of the produced geopolymers were measured. It has been found that both the magnitude of the electric impedance or the electric resistance can be used as an indicator of the degree of geopolymerization. The bulk resistance of all geopolymers increases with age over one year, suggesting that the

polymerization is a very long process. Finally, to explore the possibility to reinforce the brittle matrix such as geopolymer with Carbon Nanotubes, a model of shear force transfer from CNTs to the matrix is developed to understand and optimize the reinforcing effect of CNTs.

DEDICATION

This dissertation is dedicated to everyone who helped me and guided me through the trials and tribulations of creating this manuscript. In particular, my family and close friends who stood by me throughout the time taken to complete this masterpiece.

LIST OF ABBREVIATIONS AND SYMBOLS

CNT Carbon NanoTube

COD Crack Opening Displacement

C-S-H Calcium Silicate Hydrate

CT Compact Tension

CZM Cohesive Zone Model

DIC Digital Imagine Correlation

EDX Energy-Dispersive X-ray spectroscopy

EIS Electrical Impedance Spectroscopy

FEA Finite Element Analysis

FPZ Fracture Process Zone

FTIR Fourier Transform Infrared Spectroscopy

LEFM Linear Elastic Fracture Mechanics

MTS Material Testing System

NMR Nuclear Magnetic Resonance

OPC Ordinary Portland Cement

SEM Scanning Electron Microscopy

TPBT Three Point Bending Test

WST Wedge Splitting Test

XRD X-Ray Diffraction

ACKNOWLEDGMENTS

I am pleased to have this opportunity to thank many colleagues, friends, and faculty members who have helped me with this research project.

I would like first thank my advisor Dr. Jialai Wang for his patience and encouragement to help me through my study and research, and for his guidance and inspiration that helped to materialize this dissertation. I would thank Dr. Mark Barkey for help conducting the fracture testing. Thank Dr. James Richardson for help compressive strength testing. I also thank other committee members for your suggestions and time.

I gratefully acknowledge financial support from National Science Foundation Awards #1000580

In addition, I thank Wei Pan and other students in the group for help me conduct the testing.

I thank my wife and my family for their encouragement, support and love throughout my life.

TABLE OF CONTENTS

LIST OF TABLES

INTRODUCTION

Article 1

Article 2

Article 3

LIST OF FIGURES

INTRODUCTION

Article 1

Article 3

Article 3

INTRODUCTION

1. HISTORY OF ALKALI-ACTIVATED AND ALKALINE CEMENTS

1.1. Research Need

OPC-based concrete is the most widely used construction material. The global use of concrete is only second to water, accounting for 70% of all building and construction materials. Although OPC has many advantages such as easy of application, availability of the raw materials all over the world, it has two disadvantages when sustainability is a central concern of building materials.

Firstly, the production of OPC releases large amount of green-house gases. One ton of OPC clinker production emits at least 1.5 tons of CO_2, 60% of which is emitted from the calcination process of limestone and 40% is from the combustion of fuel in kiln (Kuhlmann and Paschmann, 1997) Cement production in US accounts for up to 7% of nation's total CO_2 emission (Van Oss and Padovani, 2003). Globally, Portland cement manufacture creates much more CO_2 emission, sometimes even up to 10% of the total CO_2 emission in some nations (Van Oss and Padovani, 2003). Secondly, OPC based concretes are susceptible to deterioration when exposed to severe environments. Low tensile strength, high brittleness, and low volume stability make them vulnerable to cracking. Higher permeability, porous microstructure, and thermodynamically unstable chemical compounds such as calcium silicate hydrate (C-S-H) (Phair, 2006) make them susceptible to corrosion and sulfate attack.

Deterioration of these OPC-based concretes has emerged as one of the biggest challenges in maintaining and protecting the US infrastructure system. According to 2013 ASCE report card for America's infrastructure (ASCE, 2013), the average grade of America's infrastructure was D+ (poor). $3.6 trillion is needed by year 2020 to bring the infrastructure system back to a serviceable condition.

The above two issues are inherent to OPC and difficult to address. This issues an urgent call for new materials to replace OPC for applications leading to more sustainable infrastructure. Geopolymer is such a material which has the potential to replace OPC to produce more environmentally infrastructure materials.

1.2. Geopolymer

Geopolymer, the word coined by Davidovotes (Davidovits, 1989), refers to mineral polymer resulting from geochemistry or geosynthesis. In simple words, geopolymer is generally a synthetic alkali aluminosilicate material that is produced from the reaction of a solid aluminosilicate with a highly concentrated aqueous alkali hydroxide or silicate solution (Davidovits, 2008a). Davidovits has also deposited that the Great Pyramid in ancient Egypt was built on site through geopolymerization, rather than made from the natural stones (Davidovits and Morris, 1988). Geopolymer has some other alternative names, by different researchers: Inorganic polymers and the products are called Inorganic Polymer Concrete (IPC), Aluminosilicate Inorganic Polymer (AIP), or Inorganic Phosphate Cement (IPC). It also might be referred as "Alkai-activated cement", which has a history starting from 1940s (Roy, 1999), "geocement", "alkali-bonded ceramic", "inorganic polymer concrete" and "hydroceramic" (Duxson et al., 2007a).

Although the history of application of geopolymer could be quite long, the research history of geopolymer is not that long. Table 1 shows the literature history of geopolymer researches (including geocements/ancient analogs) (Roy, 1999; Li et al., 2010)

Table 1. Literature history of geopolymer researches

Feret	1939	Slags used for cement.
Purdon	1940	Alkali–slag combinations.
Glukhovsky	1959	Theoretical basis and development of alkaline cements.
Glukhovsky	1965	First called "alkaline cements".
Davidovits	1979	"Geopolymer" term.
Malinowski	1979	Ancient aqueducts characterized.
Forss	1983	F-cement (slag–alkali–superplasticizer).
Langton and Roy	1984	Ancient building materials characterized.
Davidovits and Sawyer	1985	Patent of "Pyrament" cement.
Krivenko	1986	DSc thesis, R_2O–RO–SiO_2–H_2O.
Malolepsy and Petri	1986	Activation of synthetic melilite slags.
Malek et al.	1986	Slag cement-low level radioactive wastes forms.
Davidovits	1987	Ancient and modern concretes compared.
Deja and Malolepsy	1989	Resistance to chlorides shown.
Kaushal et al.	1989	Adiabatic cured nuclear wastes forms from alkaline mixtures.
Roy and Langton	1989	Ancient concretes analogs.
Majundar et al.	1989	$C_{12}A_7$–slag activation.
Talling and Brandstetr	1989	Alkali-activated slag.
Wu et al.	1990	Activation of slag cement.
Roy et al.	1991	Rapid setting alkali-activated cements.
Roy and Silsbee	1992	Alkali-activated cements: an overview.
Palomo and Glasser	1992	CBC with metakaolin.
Roy and Malek	1993	Slag cement.
Glukhovsky	1994	Ancient, modern and future concretes.
Krivenko	1994	Alkaline cements.
Wang and Scivener	1995	Slag and alkali-activated microstructure.
Shi	1996	Strength, pore structure and permeability of alkali-activated slag.
Fernández-Jiménez and Puertas	1997	Kinetic studies of alkali-activated slag cements.
Katz	1998	Microstructure of alkali-activated fly ash.
Davidovits	1999	Chemistry of geopolymer systems, technology.
Roy	1999	Opportunities and challenges of alkali-activated cements.
Palomo	1999	Alkali-activated fly ash — a cement for the future.
Gong and Yang	2000	Alkali-activated red mud–slag cement.

Puertas	2000	Alkali-activated fly ash/slag cement.
Bakharev	2001–2002	Alkali-activated slag concrete.
Palomo and Palacios	2003	Immobilization of hazardous wastes.
Grutzeck	2004	Zeolite formation.
Sun	2006	Sialite technology.
Duxson	2007	Geopolymer technology: the current state of the art.
Hajimohammadi, Provis and Devente	2008	One-part geopolymer.
Provis and Deventer	2009	Geopolymers: structure, processing, properties and industrial applications.

Other notable contributions to the geopolymer researches that are not included in this table are: Alkali-activated cements and concretes by Shi et al. (Shi et al., 2006), which is the first English book that reviews and summarizes worldwide research advances in alkali-activated cements and concrete; Geopolymer Chemistry and Applications by Davidovits (Davidovits, 2008a), which is the first book that systematically discussed the chemistry of geopolymer.

2. PROPERTIES OF GEOPOLYMER

Beside the above mentioned advanced properties of geopolymer, compared with OPC, here are some other superior properties of geopolymer (depending on the source materials used for the synthesis, these properties may vary):

High compressive strength: This is one of critical properties of geopolymer to replace OPC since all OPC concrete members are designed to carry the compressive load. Geopolymer concrete has a comparable or higher compressive strength. The highest strength currently available in the literature is 160 MPa (Shi and Day, 1995). Others also reported quite high strength such as 76 MPa (Chindaprasirt et al., 2010), 65 MPa (Chindaprasirt et al., 2007).

High early strength: 70% strength could be gained in the first 4 hours of setting (van Jaarsveld et al., 1997).

Low shrinkage: The shrinkage of geopolymer was reported to be around 100 microstrain (Wallah, 2009), which is around 1/5 ~ 1/6 of that of OPC (van Jaarsveld et al., 1997).

Resistance to acid attack: Due to the low content of calcium in geopolymer, it has a superior acid resistance (Bakharev, 2005a).

Resistance to sulfate: Unlike the OPC-based concrete that deteriorates when exposed to the sulfate environment, the strength of geopolymer could increase when it is immersed in sulfate solution (Bakharev, 2005b).

Low permeability: Its permeability could be two orders of magnitude lower than that of OPC, and thus it has a potential to protect the Portland cement concrete as coating (Zhang et al., 2010).

Fire resistance: It's generally believed that the strength of OPC plummets above 300 °C because the dehydration of $Ca(OH)_2$ at about 500 °C. While geopolymer does not suffer from this problem because it has no $Ca(OH)_2$. Ca in geopolymer could be in the form of C-S-H. Therefore it could potentially resist a much higher temperature. Kong et al. (Kong et al., 2007) compared the performance between the fly ash-based geopolymer and metakaolin-based geopolymer at the elevated temperature up to 800 °C. They found that the strength of fly ash based geopolymer increased while the metakaolin based geopolymer decreased its strength.

Low thermal conductivity: Cheng conducted an experiment by exposing one side of a 10 mm thick geopolymer panel to an 1100 °C flame and measuring the temperature of the

reverse-side of the panel, and found that after 35 min, the temperature was still under 350 °C (Cheng and Chiu, 2003).

3. APPLICATIONS OF GEOPOLYMER

Geoplolymer has found applications in many areas, including:

Immobilization of toxic metallic cations and nuclear residues: In early 1990s, Davidovits et al. started to investigate the possibilities of heavy metal immobilization by commercial geopolymeric products (Davidovits, 1991). Their efforts were then followed by van Jaarsveld et al. (van Jaarsveld et al., 1997), Perera et al (Perera et al., 2005) and Zhang et al (Zhang, J. et al. 2008).

Replacement of Portland cement: As stated before, geopolymer satisfies the requirements on a structural material and can be used to replace OPC.

Fire resistance: Because of its excellent fire resistance, geopolymer has been studied to coating the substrates to improve their fire resistance (Varela and Privorotskaya, 2005; Temuujin et al., 2009; Giancaspro et al., 2006).

Coating OPC concrete for various purposes: Geopolymer coating can be used to protect marine structure (Zhang et al., 2010), or to prevent surface deterioration of the strengthening (Balaguru, 1998).

Hydrothemal barrier in engine/turbine: This application is based on its excellent fire resistance and the low thermal conductivity as summarized by Boxley et al. (Boxley et al., 2008).

Science applied to archaeology: It is proven that the microstructure and chemical compositions of hardened geopolymer materials are quite similar to that of ancient constructions such as Egyptian pyramid, Roman amphitheater (Davidovits and Morris,

1988; Davidovits, 2008b). Many researchers then followed and many papers (Baines, 1994; Verner and Rendall, 2002; Harrell and Penrod, 1993) were published.

4. SYNTHESIS OF GEOPOLYMERIZATION

Unlike Portland cement, there are no standard ways to synthesize geopolymer. Basically there are two kinds of methods: Two-part methods and one-part methods. For the two-part methods, the Al/Si suppliers and the activators are stored separately. They are mixed together during the synthesis of the geopolymer. In one-part methods, the synthesis of geopolymer mortar/concrete is much like the Portland cement mortar/concrete. The Al/Si suppliers and the dry activators are mixed and stored together. Only water is needed to start the geopolymerization (Koloušek et al., 2007; Hajimohammadi et al., 2008).

4.1. The Choice of the Alkali Metal

Sodium (Na) and potassium (K) are the most commonly used alkali metal to synthesize geopolymers. Their effects on the geopolymerization have been investigated by van Jaarsveld and Xu (van Jaarsveld et al., 1999; Xu et al., 2001). The conclusion from their tests is that the choice of alkali metal mainly depends on the source material and the intended application.

4.2. The Alkalinity of the Solution

This is a widely investigated factor and the most significant factor controlling the compressive strength of geopolymer concrete. High alkalinity of the solution accelerates the dissolution of the raw materials, which shortens the setting time. It also enhances the compressive strength of geopolymers. The higher the alkaline concentration is, the higher the compressive strength is obtained.

4.3. The Role of Aluminum

Fernández-Jiménez et al (Fernández-Jiménez et al., 2006) synthesized geopolymer from different fly ashes, which had similar chemical composition, with regarding to the overall content of silica and alumina, but different reactive alumina. They found that the quantity of reactive alumina played an important role on the reaction rate and the final mechanical strength. In the first stage, the strength increased as the Al-rich aluminosilicate gel coating fly ash particles, and it increased further in the second stage when the Si-rich aluminosilicate gel formed. In the first stage, fly ashes had similar release rate of Al^{3+}, and then it varied as the lack of reactive alumina.

4.4. The SiO_2/Al_2O_3 Ratio

A lot of researchers (Rowles and O'Connor, 2003; Fletcher et al., 2005; Peter Duxson et al., 2005; P. Duxson et al., 2007b; Songpiriyakij et al., 2010) investigated the effect of SiO_2/Al_2O_3 ratio on the compressive strength of the geopolymer.

Rowles et al. (Rowles and O'Connor, 2003) investigated the effect of SiO_2/Al_2O_3 molar ratio within the range of 2~6 for metakaolin based geopolymers, and concluded that the optimal ratio was 5 with a compressive strength of 64 MPa.

Duxson et al. (Duxson et al., 2005) examined the metakaolin based geopolymer with an initial SiO_2/Al_2O_3 molar ratio in the range of 2.3~4.3, and found the optimal ratio to be 3.8 with an ultimate compressive strength over 70MPa. They also compared the microstructures of the geopolymers from different mixtures, and concluded that higher SiO_2/Al_2O_3 ratio gave a more homogenous structure, leading to a higher compressive strength. However, if a ratio higher than 3.8 was used, more unreacted fly ashes could be found in the resultant

product, increasing the defeat ratio and decreasing the strength of the geopolymer. This optimal value was confirmed by another study (Duxson et al., 2007b).

Fletcher et al. (Fletcher et al., 2005) extended the ratio of SiO_2/Al_2O_3 from the usual 1~4, as used by the aforementioned researchers, to 1~150, and hardened their samples at the ambient temperature (40°C) for 1 hour and cured at 90°C overnight. They found that geopolymer features started to show up only for $SiO_2/Al_2O_3 >= 1$. The ratio of SiO_2/Al_2O_3 also affected the setting and compressive strength of the produced geopolymer. Normal setting/hardening of geopolymers could only happen when $SiO_2/Al_2O_3 < 24$. With higher ratio, the geopolymer samples only deformed rather than failed, upon the compressive load. They found that the optimal ratio, with respect to the compressive strength, was 16, which gave an ultimate strength of 10.9 MPa.

Songpiriyakij et al. (Songpiriyakij et al., 2010) examined the role of SiO_2/Al_2O_3 by mixing Fly Ash with rice husks and bark ashes. They found the optimal ratio for the maximum compressive strength was 16 too. Expansion and cracks were also found for specimen with high ratio of SiO_2/Al_2O_3 (>16) after some period of curing. In the extreme case ($SiO_2/Al_2O_3 = 1035$), the specimen cracked within the first day after demolding.

Silva et al. (Silva et al., 2007) investigated the influence of Al/Si ratio on the setting time of geopolymer. Their tests showed that final setting time decreased with the increasing Al content in the initial composition, and that the shortest final setting time was 30 minutes for a molar ratio of 2.5 for SiO_2/Al_2O_3; and the longest final setting time was 220 minutes for a molar ratio of 5 for SiO_2/Al_2O_3. The preferable molar ratio of SiO_2/Al_2O_3 for high compressive strength at 24h was 3.4~3.8. The microstructure of these specimens showed significant difference. At low SiO_2/Al_2O_3 ratio, the produced geopolymer had highly

inhomogeneous microstructure full of loosely structured grains. At high SiO_2/Al_2O_3 ratio, the microstructure was highly homogeneous and dense. This phenomenon that Al content was responsible for shorter setting time, and that Si was responsible for high compressive strength can be explained as following: The Al component in the source material tended to dissolve faster than Si. As a result, there were plenty of $Al(OH)_4$ in the solution at low initial SiO_2/Al_2O_3 ratio. Condensation was likely to occur between aluminate and silicate species, producing poly(sialate) polymer structures. As the reaction developing, or with the increased initial Si in the solution, the condensation between oligomeric silicates became dominant. Further condensation between oligomeric silicates and aluminates generated a rigid 3D network of poly(sialate–siloxo) and poly (sialate–disiloxo) 3D rigid polymeric structures, which gave a high strength.

4.5. The Role of Calcium

Granizo et al. (Granizo et al., 2002) analyzed the effect of calcium hydroxide in the products of geopolymerization. The source materials were metakaolin, calcium hydroxide, and 5 M/12 M sodium hydroxide solution. According to their findings, calcium silicate hydrate (C-S-H) was the predominant product when the hydroxyl concentration was low. With the increase of the concentration of hydroxyl, the geopolymerization degree increased, and both C-S-H and geopolymer gels could be found in the reaction products.

Yip and van Deventer (Yip and van Deventer, 2003) did the macroanalysis of the C-S-H in the geopolymer binder. They found that two separate phases – calcium rich (C-S-H) and aluminosilicate rich (Geopolymer) – could co-exist in the product, depending on the alkalinity of the solution and the calcium concentration in the raw materials, and that the long-term durability of the binder depended on the stability of the interfacial phase between

these two phases. Later in 2005, they (Yip et al., 2005) conducted other tests showing that the compressive strength of geopolymer could be enhanced when C-S-H worked as micro-aggregates and that the compressive strength of the binder could be reduced when C-S-H competed with geopolymer for growth space and soluble silicates. They also found that two phases only co-existed at low alkalinity (NaOH concentration < 7.5 M). In higher alkalinity environment, calcium precipitated and scattered in the binder predominated by the geopolymer phase.

Van Jaarsveld et al. (van Jaarsveld et al., 2003) compared the characteristics of the geopolymer synthesized from different sources. They believed that the content of the calcium affected the compressive strength of the specimen. According to their experiments, higher calcium content gave a greater compressive strength. Note that the source materials used in their experiments were all class F fly ash, with a highest CaO content of 9.4%.

Winnefeld et al (Winnefeld et al., 2010) assessed the phases formed in the geopolymers synthesized from both low and high calcium fly ashes. They found that the higher strength was reached by geopolymers made from low calcium fly ash, which showed a dense low porosity microstructure; while the geopolymers made from the high calcium fly ash exhibited a high porosity, a low content of gel-like hydration products and a poor interlocking between fly ash particles. This might be partially due to relatively low content of the vitreous phase in the raw material and the much higher water/fly ash ratio needed for this kind of fly ashes to gain proper workability. The CaO content range in the high calcium fly ashes in their experiments was 27~36%.

4.6. Other Factors

Other factors that could affect the properties of geopolymers include the curing temperature. Puertas et al. (Puertas et al., 2000) showed that At room temperature the geopolymerization was really slow. Higher temperature could accelerate the reaction and extend the degree of reaction (Sindhunata et al., 2006). Palomo et al. (Palomo et al., 1999) found that temperature at the first 2~5 hours of curing is very important.

Longer curing time could improve the geopolymerization and improve the strength, but longer than 48 hours might not help significantly (Hardjito et al., 2004). Longer curing time at high temperature could break the granular of geopolymer, due to dehydration and excessive shrinkage (Khale and Chaudhary, 2007).

5. MECHANISM OF GEOPOLYMERIZATION

Due to its wide variation in raw material, synthesis processes and curing conditions, the geopolymerization process is a very complex chemical and physical process, which has not been fully understood so far.

5.1. Source Materials for Geopolymer

There are two main kinds of materials for the geopolymer: Si and Al supplier and the activator.

The Si and Al suppliers include:

1) Kaolinitic clays
2) Metokaolin
3) Fly ash
4) Blast furnace slag
5) Mix of above or other materials like stilbite or rice husks.

The activators include:

1) Caustic alkalis: MOH
2) Non-silicate weak acid salts: M_2CO_3, M_2SO_3, M_3PO_4, etc
3) Silicates: $M_2O{\cdot}nSiO_2$
4) Aluminates: $M_2O{\cdot}Al_2O_3{\cdot}2\text{-}6SiO_2$
5) Non-silicate strong acid salts: M_2SO_4

where M represents a metal cation, such as Na, K.

The most widely used activators are: NaOH, Na_2CO_3, $Na_2O{\cdot}nSiO_2$ and Na_2SO_4.

5.2. Properties of Fly Ashes

Fly ash is a by-product from the coal combustion, e.g. in the power plants, or in the production of iron. It has various chemical compositions based on the source coals. The main oxide components are SiO_2, Al_2O_3, CaO, Fe_2O_3, and SO_3. Typically, silica usually varies from 40 to 60 % and alumina from 20 to 30% (Khale and Chaudhary, 2007). Based on the content of calcium, ASTM categorizes fly ashes into two classes (ASTM 2005): C and F, as shown in Table 2.

5.3. The Geopolymerization Process

The exact chemical reaction in geopolymer synthesis is still unclear. The Glukhovsky model is deployed to explain the geopolymerization process, which includes three stages: (a) destruction–coagulation; (b) coagulation–condensation; (c) condensation–crystallization.

Table 2. Chemical Requirements of Fly Ash Classes (ASTM C618)

Chemical difference	Class F	Class C
Silicon dioxide (SiO_2) + aluminum oxide (Al_2O_3) + iron oxide (Fe_2O_3), min. %	70.0	50.0
Sulfur trioxide (SO_3), max. %	5.0	5.0
Moisture content, max. %	3.0	3.0
Loss on ignition, max. %	6.0	6.0
Available alkalis (as Na_2O), max. %	1.5	1.5

The simplified conceptual scheme is shown in Fig. 1(a) (Duxson et al., 2007a). Fig. 1(b) shows the geopolymerization sequence of metakaolin. It illustrates two phases in geopolymer: an amorphous phase and nanocrystalline phase with 'zeolite' like structure (Provis et al., 2005).

A descriptive model of the process of geopolymerization of fly ash is given by Fernández-Jiménez et al (Fernández-Jiménez et al., 2005) and is illustrated in Fig. 2. First, the fly ash particle is attacked by the activator and breaks; then the activator begins to attack the particle from both the inside and the outside; so geopolymer forms from both sides. With the growth of geopolymer gel, a uniform binder will be generated and some unreacted fly ash particles still remain as fillers.

Duxson and Provis (Duxson and Provis, 2008) showed the dissolution process of silicalumino in fly ash in details as in Fig. 3. It depicted how the chemical bonds were broken by the activators. The first step of the mechanism of glass dissolution at moderately high PH resembles that observed under acidic conditions; it was initialized by the ion exchange of H^+ for Na^+ or Ca^{2+}. While in the high PH values approaching 14, this was mainly due to the breakage of Si-O-Si and Si-O-Al chain by OH^-. The presence of alkaline

earth cations in fly ashes also gave an increased tendency toward framework disorder, which made the dissolution faster, and that also partially explained the difference between the furnace slags, class C and class F fly ashes.

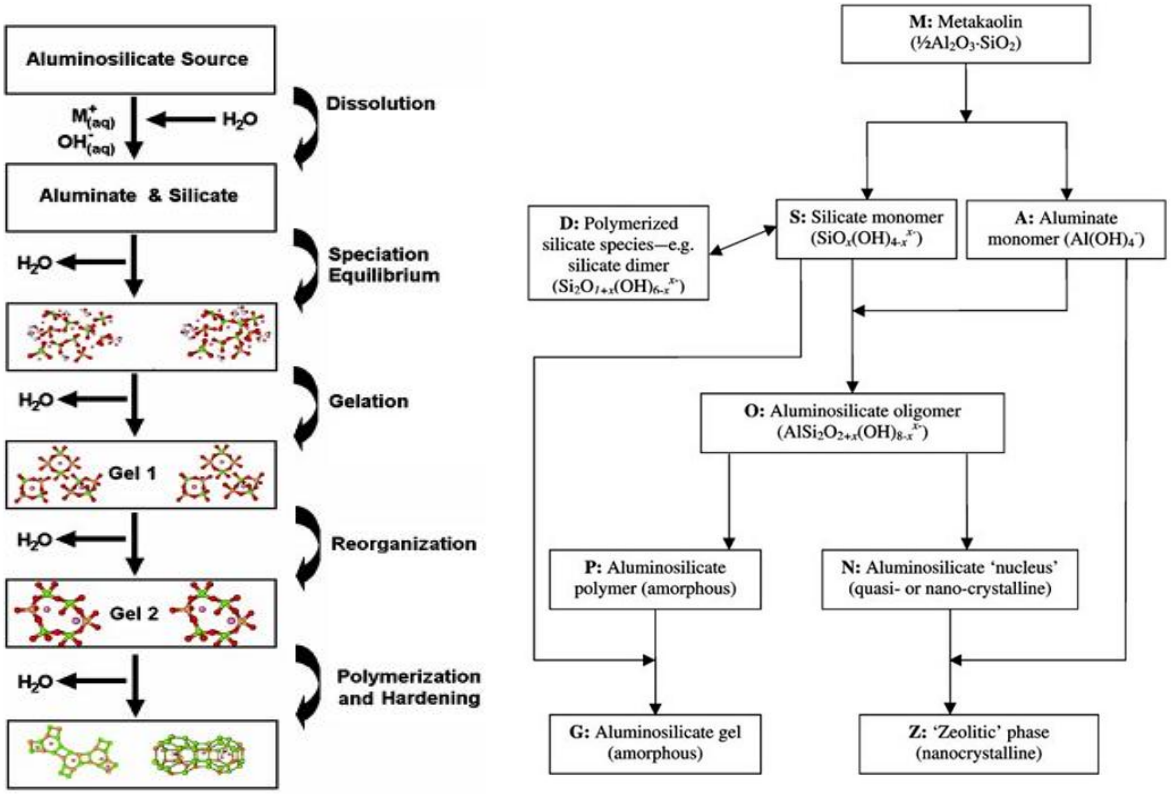

(a) (b)

Fig. 1. Process of Geopolymerization: (a) Conceptual Model of Geopolymerization; (b) Geopolymerization Sequence of Metakaolin

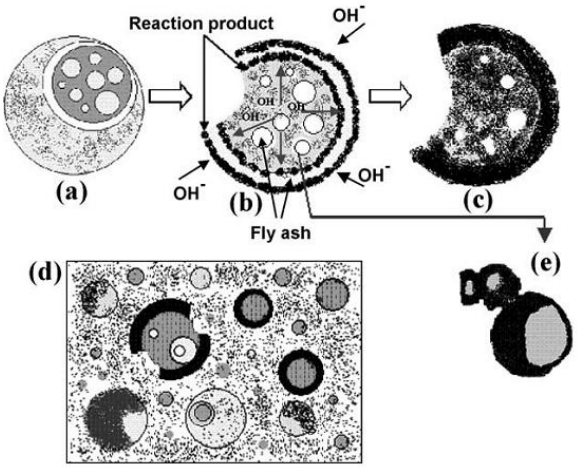

Fig. 2. Descriptive Model of Geopolymerization

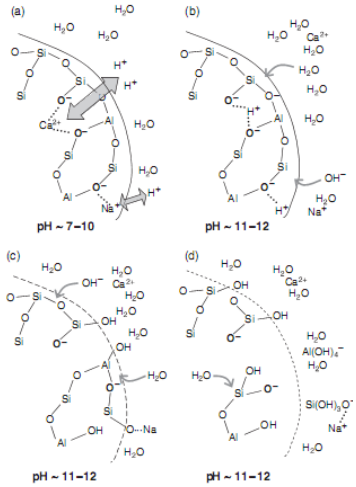

Fig. 3. Dissolution of Fly Ash

5.4. Chemistry of Geopolymer

For the chemical designation of the geopolymer, Davidovits suggests the name "polysialates", in which sialate is an abbreviation for aluminosilicate oxide. The sialate network is composed of tetrahedral anions $[SiO_4]^{4-}$ and $[AlO_4]^{5-}$ sharing the oxygen which need positive ions such as Na^+, K^+, Li^+, Ca^{2+} to compensate the electric charge of Al^{3+} in tetrahedral coordination. The proposed formula for polysialates is given by (Pacheco-Torgal et al., 2008):

$$M_n\{-(SiO_2)_z\text{-}AlO_2\}_n \cdot wH_2O.$$

where M is a cation K, Na, or Ca; *n* is degree of polycondensation; *z* is 1, 2, or 3 and *w* is amount of bound water.

Depending on the value of *z*, Davidovits (Davidovits, 2008a) proposed applications for geopolymers as shown in Table 3.

Table 3. Applications of geopolymers

Si/Al	Applications
1	Bricks, ceramics, fire protection
2	Low CO_2 cements, concrete, radioactive & toxic waste encapsulation
3	Heat resistance composites, foundry equipments, fiber glass composites
>3	Sealants for industry
20<Si/Al<35	Fire resistance and heat resistance fiber composites

The molecular structures of polysialates are shown as in Fig. 4 (www.geopolymer.org). Existing chemical models for the geopolymerization are: Davidovit's Model, Rahier's Model and Deventer's Model (Sun, 2005).

(1) Davidovit's Model:

$$(Si_2O_5, Al_2O_2)_n + 3nH_2O \rightarrow n(OH)_3Si-O-\overset{(-)}{Al}(OH)_3$$

$$n(OH)_3Si-O-\overset{(-)}{Al}(OH)_3 \xrightarrow{NaOH/KOH} (-\underset{O}{\overset{|}{Si}}-O-\underset{O}{\overset{|}{Al^{(-)}}}-O-)_n + 3nH_2O$$

orthosiala te poly(siala te)

$$(Si_2O_5, Al_2O_2)_n + nSiO2 + 4nH_2O \rightarrow n(OH)_3Si-O-\underset{(OH)_2}{\overset{(-)}{Al}}-O-Si(OH)_3$$

$$n(OH)_3Si-O-\underset{(OH)_2}{\overset{(-)}{Al}}-O-Si(OH)_3 \xrightarrow{NaOH/KOH} (-\underset{O}{\overset{|}{Si}}-O-\underset{O}{\overset{|}{Al^{(-)}}}-O-\underset{O}{\overset{|}{Si}}-O-)_n + 4nH_2O$$

ortho(sial ate - silixo) poly(siala te - siloxo)

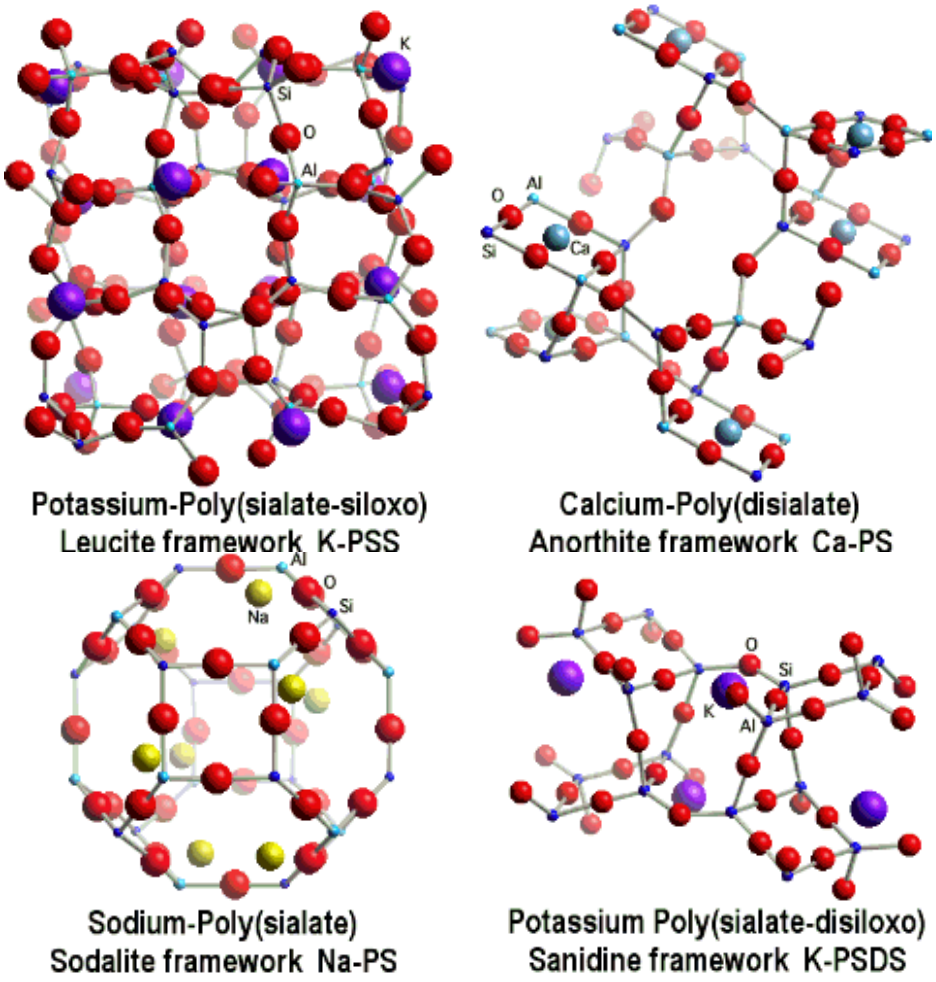

Fig. 4. Molecular Structure of Polysialate

This model is based on geopolymerization of metakaolin activated by sodium (and/or potassium) hydroxide and sodium (and/or potassium) silicate.

(2) Rahier's Model:

$$(R_2O)(SiO_2)_s(H_2O)_x + (Al_2O_3)(SiO_2)_2(H_2O)_{0.05} \xrightarrow{\text{aq.}(<100^oC)} (R_2O)(Al_2O_3)(SiO_2)_y(H_2O)_z$$

where y=$SiO_{2,\ total}/Al_2O_3$=(2+s) and z is the amount of bound water in the aluminosilicate (the approximate value of z is 0.4 if s=1.4). A fundamental assumption in

Rahier's model is that all of the metakaolin must be dissolved and react with alkali silicate solution.

(3) Deventer's Model:

$$\text{Al-Si Materials (s)} + \text{MOH (aq)} + \text{Na}_2\text{SiO}_3\text{ (s or aq)}$$
$$\Downarrow$$
$$\text{Al-Si Materials (s)} + [\text{M}_z(\text{AlO}_2)_x(\text{SiO}_2)_y \cdot \text{nMOH} \cdot \text{mH}_2\text{O}]\text{(gel)}$$
$$\Downarrow$$
$$\text{Al-Si Materials (s)} + [\text{M}_a((\text{AlO}_2)_a(\text{SiO}_2)_b) \cdot \text{nMOH} \cdot \text{mH}_2\text{O}]$$
$$\text{(Geopolymers with amorphous structure)}$$

In this model, partial dissolution of the Al-Si minerals or industrial waste was allowed, and the un-dissolved Al-Si solids contained in the geopolymer could behave as reinforcement of the matrix.

5.5. Microstructure of Geopolymer

To investigate the microstructure of the geopolymer, various chemical analysis instruments were used, such as SEM (Scanning Electron Microscopy), XRD (X-Ray Diffraction), NMR (Nuclear Magnetic Resonance), FTIR (Fourier Transform Infrared Spectroscopy).

5.5.1. SEM images

SEM images are mainly used to analysis the morphology of the geopolymer gel. A typical secondary electron image is shown in Fig. 5. (Duxson et al., 2005). Depending on the source materials and the curing condition, geopolymer could be either loose and inhomogeneous (Fig. 5(a)), which gives a lower compressive strength; or dense and homogeneous (Fig. 5(b)), which gives a higher compressive strength.

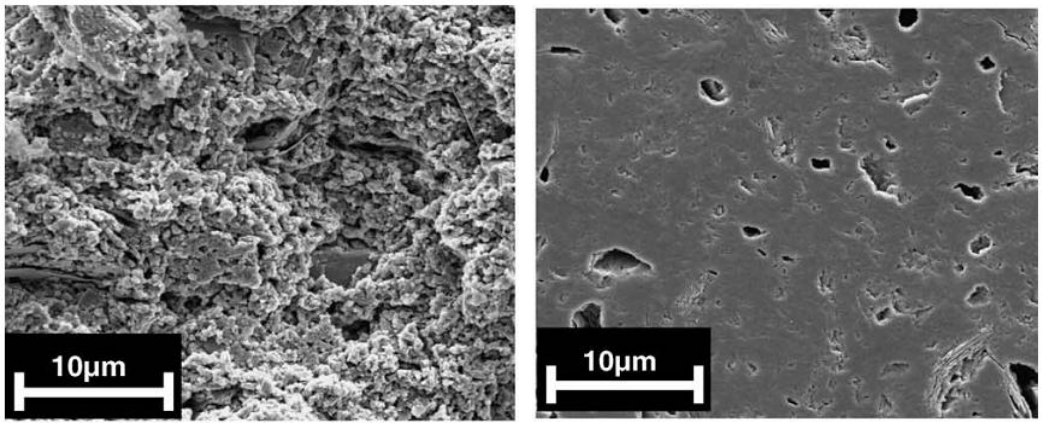

(a) (b)

Fig. 5. SEM Images of Geopolymer

5.5.2. NMR analysis

NMR analysis is used both to find out the microstructure of the geopolymer and to track the reaction progress. ^{29}Si and ^{27}Al NMR spectrum are most widely used. The Si^{4+} and Al^{3+} cations in the framework of aluminosilicate geopolymeric gels (often referred to as ‘‘T atoms’’) are tetrahedrally coordinated and linked by oxygen bridges. Fig. 6 and Fig. 7 (Duxson et al., 2007a) show typical NMR spectra of the raw material and the synthesized geopolymer.

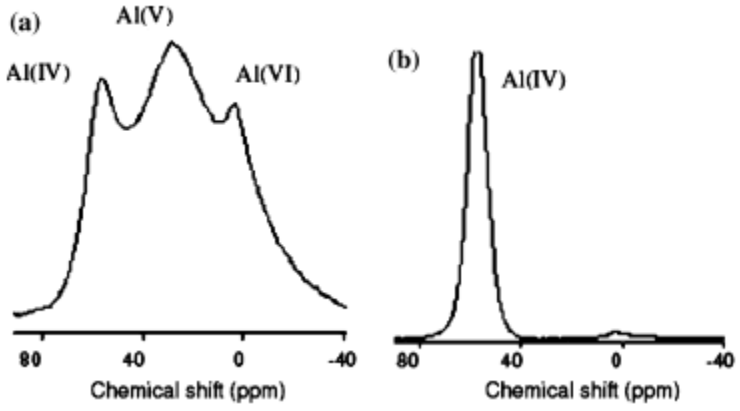

Fig. 6. ^{27}AL NMR Spectra: a) Metakaolin, b)Metakaolin Based Geopolymer

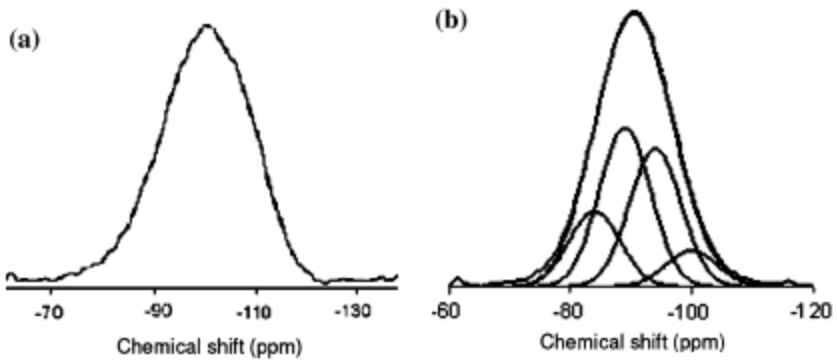

Fig. 7. ^{29}Si NMR Spectra: a) Metakaolin, b)Metakaolin Based Geopolymer

6. FRAME OF THIS DISSERTATION

Although geopolymer possesses many advantages compared with OPC, it suffers from a major drawback: its properties largely depend on its source materials such as fly ashes. Unfortunately, fly ashes vary from source to source in either physical properties, like particle sizes, amorphous proportion, or chemical compositions. Even from the same source, these properties could change significantly too. The difference in the properties of fly ash is resulted from the difference in coals and the way the coal is burned. Therefore, no standard method exists which can predict the properties of geopolymers based on their mix design. In this dissertation study, a compressive experimental program has been carried out to synthesize and characterize geopolymers made fly ash from different sources. Fly ashes from four power plants were used to synthesize geopolymers. These fly ashes were carefully selected to include both the high calcium and low calcium fly ashes and two fly ashes with very similar chemical compositions. Two low-calcium fly ashes have very similar chemical compositions. This will allows us not only to compare the properties of geopolymers based on high and low calcium fly ashes, but also to examine whether similar properties can be reached by geopolymers synthesized from fly ashes with similar chemical compositions.

This dissertation is arranged in this way. The first paper focuses on the synthesizing, mix design, and mechanical properties of geopolymer made of four different fly ashes. In the second paper, the nonlinear fracture behavior of the fly ash-based geopolymer has been studied using splitting wedge testing and digital image correlation technique. In the third paper, the electrical properties of four geopolymers are studied to gain fundamental understanding of the geopolymerization process. Because geopolymer is very brittle, carbon nanotubes (CNTs) are explored in theory to toughen this material. To this end, an analytical solution is developed to describe the shear force transfer between CNTs and the matrix. The findings of this dissertation research are summarized in the overall conclusion of this dissertation.

SYNTHESIS AND CHARACTERIZATION OF GEOPOLYMERS USING FOUR LOCALLY AVAILABLE FLY ASHES

ABSTRACT

Geopolymer can be synthesized using industrial wastes such as fly ash, making it a promising material to replace Ordinary Portland Cement (OPC) as a green binder for concrete materials. One major barrier preventing the wide application of geopolymer is that its properties heavily depend on the source materials. In this study, fly ashes from four power plants were used to synthesize geopolymers. These fly ashes were carefully selected to include both the high calcium and low calcium fly ashes, and two of the fly ashes have very similar chemical compositions. Comprehensive experimental programs have been carried out to characterize these fly ashes, to examine the critical factors affecting the mechanical properties of geopolymers, and to evaluate the potentials of four locally available fly ashes as source materials for geopolymers. Experimental results show all these fly ashes can be used to synthesize geopolymer. Among them, the fly ash from Gaston is found to be the most suitable source material for geopolymer because it has the highest reactive content.

1. INTRODUCTION

Ordinary Portland Cement (OPC) based concrete is the most widely used construction material. The global use of concrete is only second to water, accounting for 70% of all building and construction materials. Although OPC has many advantages such as ease of

application, availability of the raw materials all over the world, it has two disadvantages when sustainability is a central concern of building materials.

Firstly, the production of OPC releases large amount of green house gases. One ton of OPC clinker production emits at least 1.5 tons of CO_2, 60% of which is emitted from the calcinations process of limestone and 40% is from the combustion of fuel in kiln (Kuhlmann and Paschmann, 1997). Cement production in US accounts for up to 7% of nation's total CO_2 emission (Van Oss and Padovani, 2003). Globally, Portland cement manufacturing creates much more CO_2 emission, up to 10% of the total CO_2 emission in some nations (Van Oss and Padovani, 2003). Secondly, OPC based concretes are susceptible to deterioration when exposed to severe environments. Low tensile strength, high brittleness, and low volume stability make them vulnerable to cracking. Higher permeability, porous microstructure, and thermodynamically unstable chemical compounds such as calcium silicate hydrate (C-S-H) (Phair, 2006) make them susceptible to rebar corrosion and sulfate attack. Deterioration of these OPC-based concretes has emerged as one of the biggest challenges in maintaining and protecting the US infrastructure system. According to 2013 ASCE report card for America's infrastructure (ASCE, 2013), the average grade of America's infrastructure is D+ (poor). $3.6 trillion is needed by year 2020 to bring the infrastructure system back to a serviceable condition.

The above two issues are inherent to OPC and difficult to address. This issues an urgent need for new materials to replace OPC in applications leading to a more sustainable infrastructure. Geopolymer is such a material which has the potential to replace OPC to produce more environmentally infrastructure materials. Geopolymers are amorphous three-dimensional alumino-silicate binder materials. They can be synthesized by mixing source

material (alumino-silicate reactive materials such as metakaolin, fly-ashes) and an alkaline activator (strong alkaline solutions such as NaOH or KOH) and then curing them at room or elevated temperature. Compared with OPC, geopolymer possesses the following advantages: a) less energy consumption and CO_2 emission (20% of the carbon dioxide emissions produced in the manufacturing of OPC) during manufacturing, b) higher strength and much less shrinkage, c) lower permeability (comparable to natural granite), and d) substantially higher resistance to fire and acid attacks. Geopolymers are considered as "green materials" and strong candidates to replace OPC in selected applications leading to more sustainable infrastructure system.

Despite its many advantages compared with OPC, geopolymer suffers from a major drawback: its properties largely depend on the source materials such as fly ashes. Unfortunately, fly ashes vary from source to source in either physical properties, like particle sizes, amorphous proportion, or chemical compositions. Even from the same source, these properties could change significantly too. The difference in the properties of fly ash is resulted from the difference in coals and the way the coal is burned. Therefore, no standard method exists which can predict the properties of geopolymers based on their mix design. In this study, a compressive experimental program has been carried out to synthesize and characterize geopolymers made fly ash from different sources. Fly ashes from four power plants were used to synthesize geopolymers. These fly ashes were carefully selected to include both the high calcium and low calcium fly ashes and two fly ashes with very similar chemical compositions. Two low-calcium fly ashes have very similar chemical compositions. This will allows us not only to compare the properties of geopolymers based

on high and low calcium fly ashes, but also to examine whether similar properties can be reached by geopolymers synthesized from fly ashes with similar chemical compositions.

2. MATERIALS AND METHODS

2.1. Characterization of Source Fly Ashes

Fly ashes used to synthesize geopolymer are usually different both chemically and physically, leading to different properties of the produced geopolymers. With an aim to relate the properties of geopolymer to that of the fly ashes, an experimental program has been carried out to characterize the fly ashes used in this study. Fly ashes from four power plants, Gaston, Miller, Orlando and Martin Lake, were used as source materials to synthesis geopolymer. These characterization tests include:

2.1.1. Chemical Composition

The chemical composition of these fly ashes can be very different because of the different sources of coals and different burning techniques. The chemical compositions of these fly ashes were analyzed following ASTM C618-05 (ASTM C618-05, 2005) and are shown in Table 1. Fly ash from Miller has high calcium content and can be classified as class C fly ash. The rest of the fly ashes are class F (low calcium). Fly ashes from Gaston and Orlando have very similar chemical compositions

Table 1. Chemical Composition of Fly Ashes

Source	SiO_2	Al_2O_3	Fe_2O_3	SO_3	CaO	Moisture	LOI	Na_2O
Orlando	54.48%	27.72%	8.14%	0.11%	1.29%	0.15%	4.11%	0.67%
Miller	36.23%	19.41%	6.45%	1.84%	23.11%	0.11%	0.61%	1.50%
Martin Lake	54.88%	19.31%	8.46%	0.45%	8.03%	0.10%	0.04%	0.62%
Gaston	50.38%	27.20%	9.14%	0.30%	2.49%	0.14%	2.95%	0.69%

2.1.2. Dissolution Degree of Fly Ashes

Even with the same chemical composition, the reactivity of these chemical compounds could be different. Only the amorphous phases in fly ashes participate in the geopolymerization, while the crystalline phases become fillers in the resulting geopolymer. The dissolution test was designed and carried out to determine the content of this reactive content in fly ash samples. Five samples were tested for each fly ash following the testing procedure outlined below:

1) Weigh specified amount of fly ashes.

2) Make NaOH aqueous solution with specified concentration (14M).

3) Mix well the fly ash and NaOH aqueous solution in a testing bottle.

4) Vibrate the bottle in oven at 75°C for 24 hours.

5) Filter the solution for the residue.

6) Weigh the residue and calculate the dissolution degree of the fly ash. The dissolution degree is defined as the mass ratio in percentage between the materials dissolved in the NaOH solution and the total mass of the virgin fly ashes.

2.1.3. Micro-Structure of Fly Ashes

Scanning electron microscopy (SEM) and Energy-dispersive X-ray spectroscopy (EDX) were used to examine the morphology of the fly ashes before and after dissolution testing. The X-Ray Diffraction (XRD) spectrum was used to determine the change of the crystalline materials within the fly ashes before and after dissolution testing.

2.2. Synthesis of Geopolymers

A standard mix design method is not available for geopolymers due to the differences of the source materials. A systematic experimental program has been carried out to determine

the optimal mix of the geopolymers based on these locally available fly ashes. A mix of Sodium Hydroxide (NaOH) solution and Sodium Silicate solution was chosen as the activator of the geopolymer. Sodium Silicate solution is of lab level from Fisher Scientific containing 29.4 wt% of SiO_2, 9.1 wt% of Na_2O, and 61.5 wt% of water. Only fine aggregates are used to synthesize geopolymer mortars. Superplasticizer is also used to enhance the workability.

Two major methods are commonly used to produce geopolymers: a) two-part method, and b) one-part method. In the two-part method, the Al/Si suppliers and the activators are stored separately, and are mixed together during synthesizing geopolymer; while in the one-part method, the Al/Si suppliers and the dry activators are mixed together as a whole. Only water is needed later to initiate geopolymerization process (Hajimohammadi et al., 2008). It is rather difficult to use dry activators in geopolymer. Therefore, the two-part method is much more popular that the one-part method.

In this study, geopolymer was synthesized using the two-part method as shown in Fig. 1. NaOH aqueous solution and Sodium Silicate were mixed together and stood still for 24 hours to ensure thoroughly mixing of these two solutions. A hand mixer with rotation speeding varying from 80~1200 RPM was used to mix the alkaline solution with fly ashes for 3 minutes. Then sands were added and mixed for additional 5 minutes before the fresh geopolymer mortar was cast in 2×4 in. cylindrical molds. A vibration table (Syntron® Jogger J-1-B from FMC Technologies, Inc) was used to consolidate the geopolymer mortar specimens. After vibration, the produced fresh mortar specimens were stored in the laboratory for 2 hours, which is referred to as delay time, and then put into an oven to cure

at 75°C. The two-hour delay has been found beneficial to the strength development (Chindaprasirt et al., 2007).

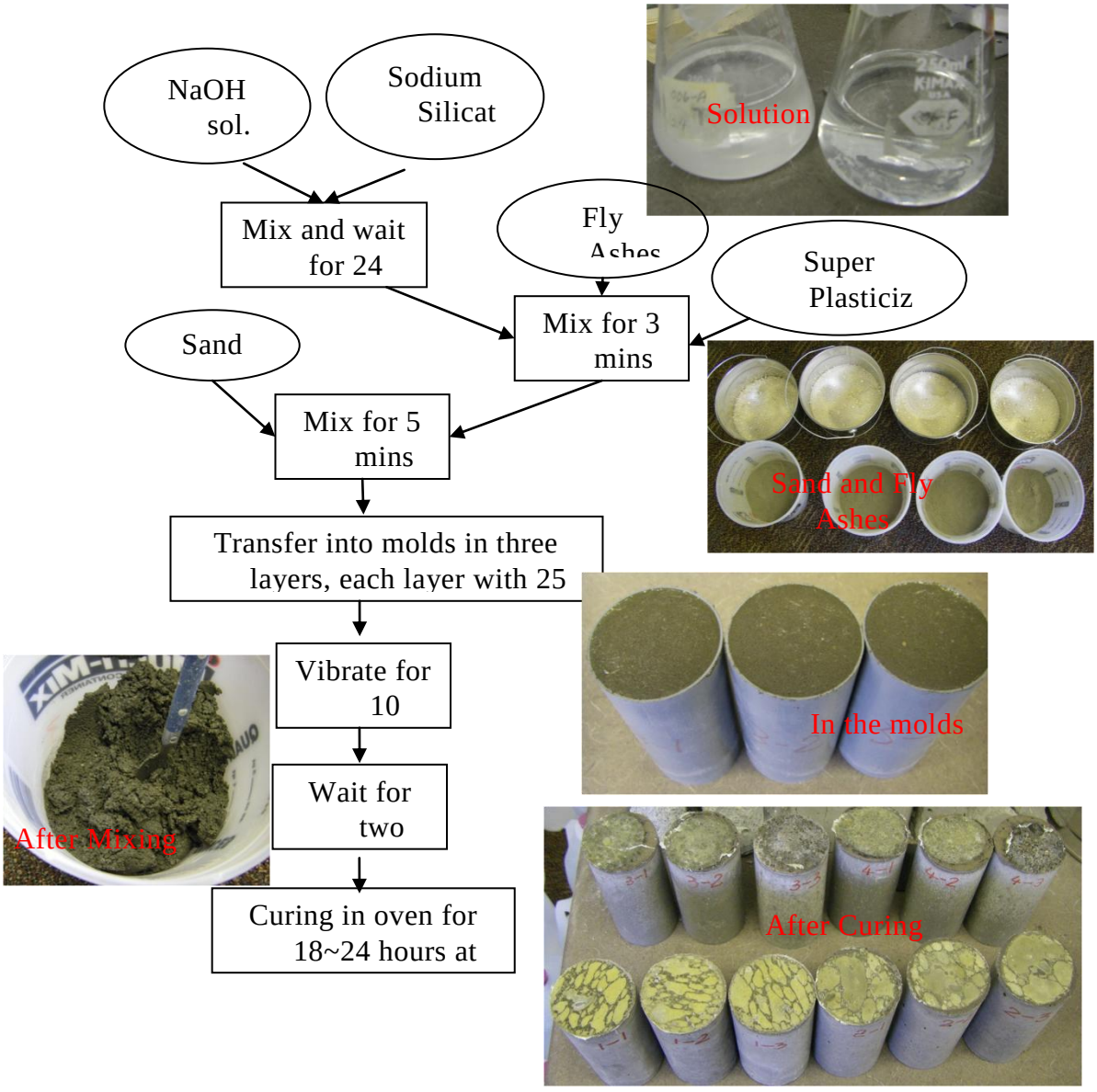

Fig. 1. Synthesis Procedure of Geopolymer Mortar Specimens

Cylindrical samples of geopolymer with size of 2×4 in. were manufactured to measure the compressive strength in compliance with ASTM C39-05 (ASTM C39-05, 2005). The loading rate was chosen as 0.03 in/min so that the stress rate was within 35×10^7 psi/s as

specified by ASTM C39-05 (Figs. 3 and 4). Before testing, specimens were capped with sulfate cement so that both surfaces were flat and parallel (Fig. 2). The compressive strength and Young's modulus were recorded for each specimen.

Fig. 2. Specimens with Capping

Fig. 3. Setup of Strength Testing

Fig. 4. Specimens after Testing

2.3. Factors Affecting Properties of Geopolymer and Mix Design

The properties of geopolymers largely depend on the properties of their source materials, the fly ashes and the alkaline activator. Since there is no standard mix design method existing for fly ash-based geopolymers, an experimental program has been carried out to examine the effects of important mix design parameters on the properties of produced geopolymers based on locally available fly ashes. To this end, geopolymers based on locally available fly ashes have been made with different mix design parameters. The strength and elastic modulus of these geopolymers were measured so that the effects of these parameters on the properties of geopolymers can be determined, based on which, the optimal mix design can be obtained. All geopolymer mortar made in this study contains 60% sand by weight. Silva et al. (Silva et al., 2007) found that the preferable molar ratio of SiO_2/Al_2O_3 for high compressive strength at 24h was 3.4~3.8. The microstructure of these specimens showed significant difference. At low SiO_2/Al_2O_3 ratio, the produced geopolymer had

highly inhomogeneous microstructure full of loosely structured grains. At high SiO_2/Al_2O_3 ratio, the microstructure was highly homogeneous and dense. Duxson et al. (Duxson et al., 2005) also found that the optimal molar ratio of SiO_2/Al_2O_3 was 3.8 for metakaolin based geopolymer. Therefore, in this study the molar ratio of SiO_2/Al_2O_3 was chosen as 3.8 and the molar ratio of Na_2O/Al_2O_3 was chosen as 0.8 if not specified. High alkalinity of the activator solution accelerates the dissolution of the source materials, reducing the setting time and enhancing the compressive strength of geopolymers. However, too high alkalinity of the activator means higher material cost and lower workability. Therefore, the concentration of NaOH was chosen as 14M in this study. In such a case, the mix design of the geopolymer using fly ash from Gaston can be obtained and shown in Table 2 (Note that super plasticizer is not counted in percentage computation). The produced specimens were cured in oven for 48 hours at 75°C.

Table 2. Mix Design of Geopolymer Using Fly Ashes from Gaston (in Mass)

Ingredients	**fly ash**	**Sodium silicate**	**NaOH solution**	**super plasticizer**	**Sand**
Content (wt%)	24.48%	8.68%	6.84%	2.00% of fly ash	60%

2.3.1. The Effect Alkalinity of the Activator

Four concentrations of NaOH solution (8M, 10M, 14M and 16M) were used to manufacture geopolymer specimens using fly ash from Gaston. The mix of these geopolymer specimens were obtained by adjusting activator contents in the mix design shown in Table 2. Their strength and elastic modulus were measured to determine the effect of the alkalinity of the activator.

2.3.2. Effect of the Ratio of Na_2O/Al_2O_3

Gaston fly ash was used in this test. Four different ratios of Na_2O/Al_2O_3 based on the gross chemical composition of the fly ash were used to manufacture geopolymer specimens. Their strength and elastic modulus were measured to determine the effect of the gross ratio of Na_2O/Al_2O_3.

2.3.3. Effect of the Ratio of SiO_2/Al_2O_3

Geopolymer specimens were made with Gaston fly using different ratio of SiO_2/Al_2O_3 (3.2, 3.4, 3.6, 3.8, 4.0 and 4.2). Their strengths and elastic modulus were measured to determine the effect of the gross ratio of SiO_2/Al_2O_3.

2.3.4. Effect of Age

Two groups of geopolymer specimens were made (with SiO_2/Al_2O_3=3.6, 3.8) using Gaston fly ashes. The average compressive tests of three duplicated samples were measured at the age of 1, 2, 7, 14, 28, 56 and 84 days.

2.3.5. Effect of Effective Ratios of Na_2O/Al_2O_3 and SiO_2/Al_2O_3

Various reaction kinetic models for the geopolymerization have been proposed (Provis et al., 2005; Provis and van Deventer, 2007). They all share a similar procedure: 1) dissolution of the fly ashes in the basic condition to form mobile precursors; (2) part of these precursors reconstructed to form alkali polysilicates; and (3) reprecipitation that forms an inorganic polymeric structure and hardens the whole system (van Jaarsveld et al., 2002). It can be seen that the dissolution of the fly ashes is critical to the geopolymerization process. It determines the amount of available precursors and thus the final products. Since only the dissoluble portion of the fly ashes could participate in the geopolymerization, we refer the molar ratio of Na_2O/Al_2O_3 and SiO_2/Al_2O_3 based on the dissoluble components to as

effective molar ratio. It is anticipated that such a molar ratio may be independent of the source of the fly ash.

2.3.6. Effect of the Source of the Fly Ash

To determine fly ash types affect the properties of the geopolymer, fly ashes from different sources (Gaston, Orlando, Miller and Martin Lake) were used to synthesize geopolymers. The weight percentage of source materials is specified as in Table 2. This percentage is chosen to make the SiO_2/Al_2O_3=3.8 and Na_2O/Al_2O_3=0.8 for the fly ashes from Gaston. This mix is adjusted for other fly ashes based on their chemical compositions to ensure SiO_2/Al_2O_3=3.8 and Na_2O/Al_2O_3=0.8 in all geopolymers. Three duplicated geopolymer specimens were made for each type of fly ashes.

3. RESULTS AND DISCUSSIONS

3.1. Dissolution of Fly Ashes

Dissolution tests have been carried out in 14M NaOH solution, which is used in most geopolymer specimens that were manufactured and tested. Five samples were tested for each fly ash. The fly ash from Gaston was tested first. In the initial dissolution testing, about 5g of fly ash samples were taken to mix into 156g 14M NaOH solution. Test results are presented in Table 3. The fifth sample was opened during the vibration, resulting in significant carbonation of the solution and loss of water. Therefore, its result is not available. This testing shows that the average dissolution degree of four fly ash samples is only 30%, which is quite low. This may be caused by the high amount of fly ash used in the testing. If too much fly ash is used in the dissolution testing, there will be no sufficient NaOH solution to dilute the materials leached out of the fly ash. These dissolved materials will form precipitants, which cannot be filtered out by the filter papers used in this testing, leading to

a low dissolution degree. To reduce the precipitant during the dissolution test, we reduced the amount of fly ash used in the test and measured the corresponding dissolution degree. It has been observed that the dissolution degree increased with the decrease of the amount of fly ash. Finally, it was determined that 1.5g is the optimal amount of fly ash to be used in the dissolution testing because with this small amount of fly ash, the dissolution testing results are very consistent. Table 4 shows that when 1.5g of fly is used, the dissolution degree of the fly ash from Gaston increases to 57.5%, significantly higher than the dissolution result obtained using 5g fly ash.

Similarly, dissolution results of fly ashes from Orlando, Miller, and Martin Lake are presented in Tables 5, 6, and 7, representatively. It can be seen that fly ash from Orlando has a very similar dissolution degree as that of the fly ash from Gaston, suggesting these two fly ashes may have similar amount of amorphous material which can participate in the geopolymerization. The dissolution degree of fly ash from Martin Lake is only 48.6%, significantly lower than other two low-calcium fly ashes, indicating that less amorphous material is available in this fly ash. The only high-calcium fly ash, the fly ash from Miller exhibits the lowest dissolution degree, which may be caused by the fast precipitants induced by the calcium in the fly ash during the dissolution testing. It may also indicate that significant difference exists between the high calcium and low calcium fly ashes in geopolymerization process.

Table 3. Dissolution of Gaston Fly Ashes (5g Fly Ash)

No.	**1**	**2**	**3**	**4**	**5**
FA(g)	4.99	5	5	4.99	5
Weighing pan	1.75	1.74	1.62	1.58	NA
Filter paper	2.71	2.7	2.7	2.66	NA
Final	8.09	7.68	7.98	7.68	NA

Dissolution	27.25%	35.20%	26.80%	31.06%	NA
Average	30.08%				

Table 4. Dissolution of Gaston Fly Ashes (1.5g Fly Ash)

No.	**1**	**2**	**3**	**4**	**5**
FA(g)	1.55	1.51	1.5	1.52	1.5
Weighing pan	1.72	1.62	1.72	1.59	1.73
Filter paper	1.33	1.33	1.33	1.98	1.98
Final	3.72	3.6	3.71	4.22	4.3
dissolution	56.77%	56.95%	56.00%	57.24%	60.67%
average	57.52%				

Table 5. Dissolution of Orlando Fly Ashes

No.	**1**	**2**	**3**	**4**	**5**
FA(g)	1.5	1.5	1.5	1.5	1.5
Weighing pan	1.69	1.66	1.65	1.67	1.59
Filter paper	1.3	1.32	1.33	1.32	1.31
Final	3.61	3.55	3.62	3.61	3.46
dissolution	58.67%	62.00%	57.33%	58.67%	62.67%
average	59.87%				

Table 6. Dissolution of Miller Fly Ashes

No.	**1**	**2**	**3**	**4**	**5**
FA(g)	1	1	1	1	1
Weighing pan	1.68	1.57	1.7	1.58	1.68
Filter paper	1.44	1.44	1.46	1.45	1.43
Final	3.66	3.64	3.71	3.69	3.76
dissolution	46.00%	37.00%	45.00%	34.00%	35.00%
average	39.40%				

Table 7. Dissolution of Martin Lake Fly Ashes

No.	**1**	**2**	**3**	**4**	**5**
FA(g)	1	1	1	1	1
Weighing pan	1.67	1.61	1.69	1.59	1.68
Filter paper	2.9	2.2	1.43	1.47	1.45
Final	5.02	4.42	3.66	3.57	3.59
dissolution	55.00%	39.00%	46.00%	49.00%	54.00%
average	48.60%				

3.2. Microstructure of Fly Ashes and Their Residues

The X-Ray Diffraction (XRD) spectra of all four types of fly ashes before and after dissolution testing have been collected and are shown in Figs. 5 to 8. All these figures show that significant amount of amorphous phases existing in all fly ashes, as indicated by the bumps between 20° to 40° on the XRD spectra. After dissolution testing, these bumps were reduced significantly or disappeared, suggesting that amorphous phases in fly ash were dissolved in the alkaline solution in the dissolution test. XRD spectra show that the major crystalline materials existing in the fly ash samples are mullite, hematite, quartz, maghemite, and portlandite as shown in Figs. 5–8.

By comparing the reduction of the bumps, we can find that fly ash from Gaston has the highest content of amorphous phases; fly ash from Orlando comes next; and the high calcium fly ash from Miller seems to contain lowest amorphous materials. This seems to contradict with the dissolution testing results presented in Tables 4 and 5, which show that fly ashes from Gaston and Orlando have similar dissolution degrees. However, by examining the XRD spectra of these two fly ashes, we can see that significant amount of zeolite exists in the fly ash from Gaston after dissolution testing, as shown in Fig. 5; while very little can be found in the fly ash from Orlando after dissolution testing even though it has very similar chemical composition as the fly ash from Gaston, as shown in Fig. 6. Since no zeolite can be identified from the XRD spectrum of the fly ash before the dissolution testing, the zeolite must be produced by the chemical reaction between the alkaline solution and the amorphous phases of the fly ash dissolved in the solution. These zeolites could not be dissolved in the alkaline solution and precipitated on the surface of the fly ash, increasing

the residual mass of the fly ash. As a result, the calculated dissolution degree in Table 4 is lower than it actually is. In such a case, dissolution testing is not reliable to determine the amorphous phase content in the fly ash.

Compared with low-calcium fly ashes, high calcium fly ash from Miller shows a different XRD spectrum after dissolution testing. As shown in Fig. 8, the intensity of most peaks on the XRD spectrum is weaker and considerable amount of amorphous phases still exist after the dissolution testing. This is because that the calcium content in the fly ash can produce fast precipitant (which is very likely portlandite as shown in Fig. 8) covering the surface of the fly ash, which not only prevents further dissolving of the fly ash, but also reduces the intensity of the peaks of the crystalline phases.

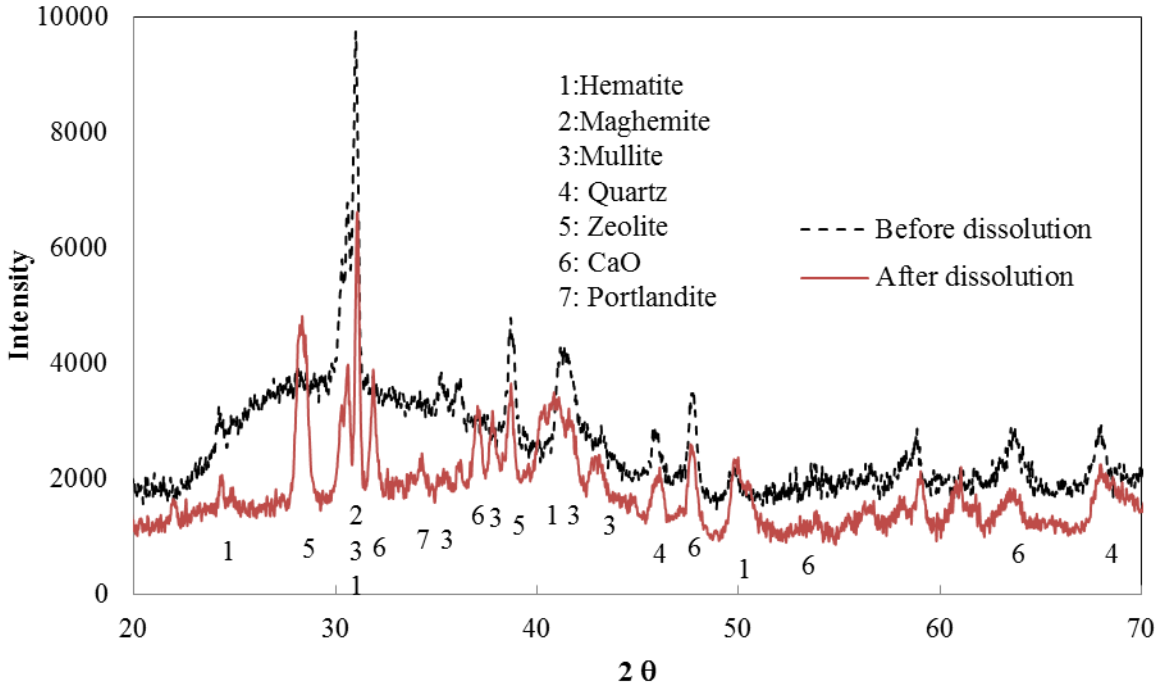

Fig. 5. XRD of Fly Ash from Gaston before and after Dissolution Testing

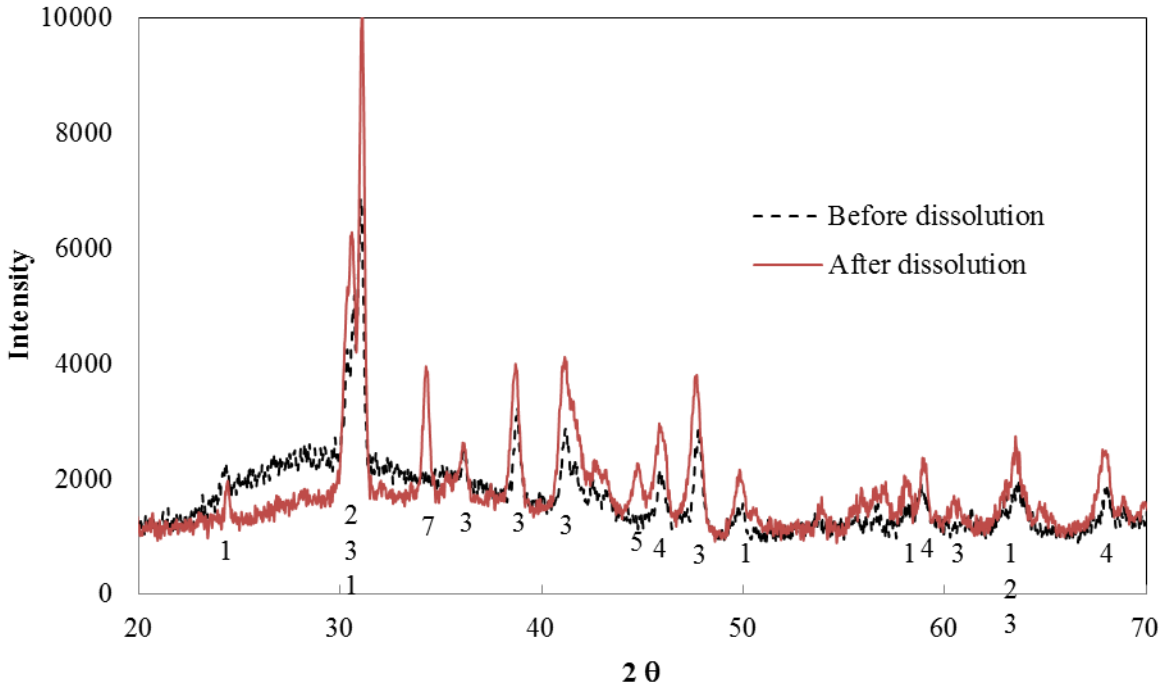

Fig. 6. XRD of fly ash from Orlando before and after dissolution testing

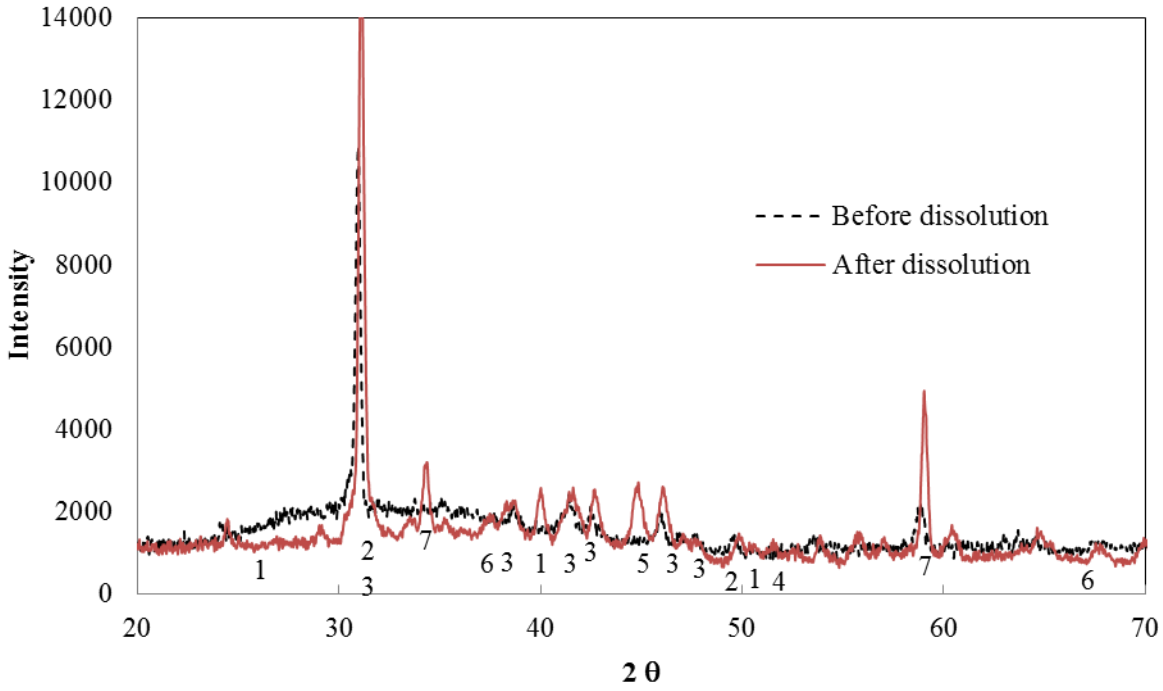

Fig. 7. XRD of Fly ash from Martin Lake before and after Dissolution Testing

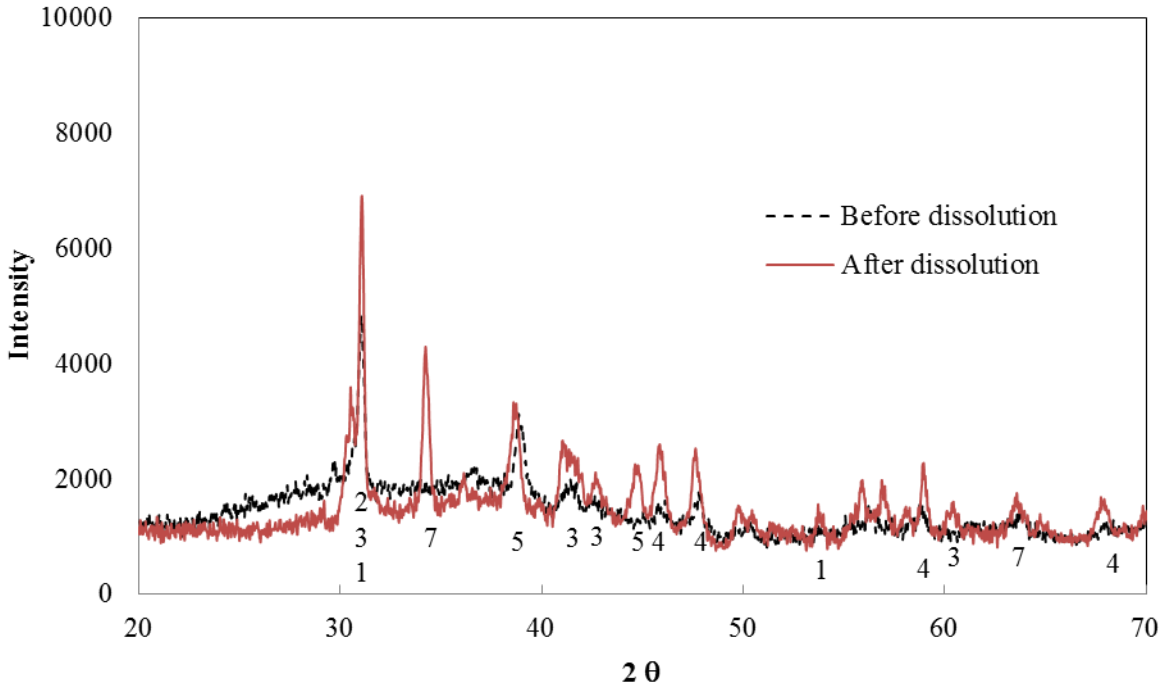

Fig. 8. XRD of Fly Ash from Miller before and after Dissolution Testing

The Scanning Electric Microscopy (SEM) images of fly ashes are shown in Fig. 9. From SEM images, there is no significant difference existing among these fly ashes. They all contain some large and some much smaller spherical particles. The large particles from Gaston and Orlando are larger than those in fly ashes from Martin Lake and Miller.

Figure 10 shows the SEM image of the fly ash from Gaston after dissolution. After dissolving of the amorphous phases in the fly ash by the alkaline solution, crystalline phases were exposed and some new precipitant was produced. For example, part *A* indicated in Fig. 10(a) shows that zeolite was produced during the dissolution testing, which agrees with the finding obtained by the XRD analysis as shown in Fig. 5. The Part *B* indicated in Fig. 10(b) is the mullite, which has been found existing in all fly ashes as shown in Figs. 5–8. Another mineral existing in all fly ash is hematite, which is identified and labeled as *C* in Fig. 10(c).

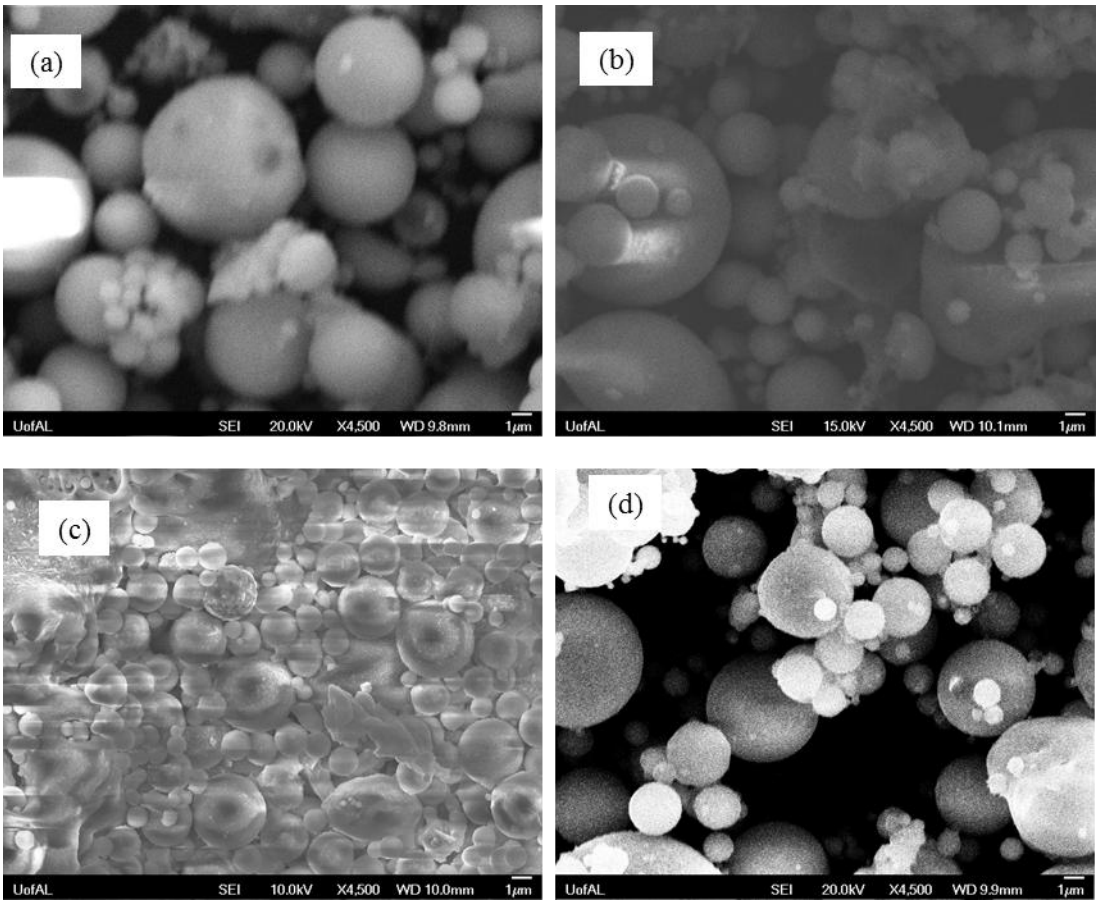

Fig. 9. SEM Images of Fly Ashes from: (a) Gaston; (b) Orlando; (c) Martin Lake; (d) Miller

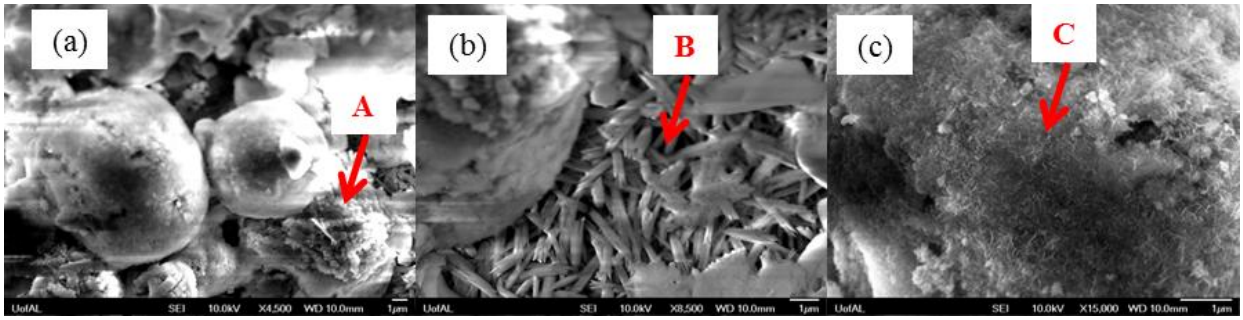

Fig. 10. SEM Images of Residue of Fly Ashes from Gaston after Dissolution Testing

Figure 11 shows the SEM images of the residue of the fly ash from Orlando after dissolution testing. It can be seen that amorphous phases on the surface of the fly ash particles were dissolved, and the crystalline phases of the fly ash are therefore exposed. The majority of these crystalline phases are mullite, as also shown by XRD analysis (Figs. 5–8).

As shown in Fig. 11, the residue minerals covers the surface of the fly ash particle, which may prevent further dissolving of amorphous materials from this fly ash. Some precipitant can be identified in Fig. 11(a), which is very likely the portlandite as indicated in XRD spectrum (Fig. 6) induced by the reaction of calcium content in the fly ash with the alkaline solution.

Figure 12 shows the SEM images of the residue of the fly ash from Martin Lake after dissolution testing. Similar to the fly ashes from Gaston and Orlando, mullite is the major mineral residue of this fly ash after dissolution testing, as shown in Fig. 12(c). However, much more precipitants (portlandite) can be seen (Figs. 12(a) and 12(b)), which is caused by the relatively high content of CaO (8.03%) in this fly ash. These precipitants may be also responsible for the low dissolution degree of this fly ash (Table 7).

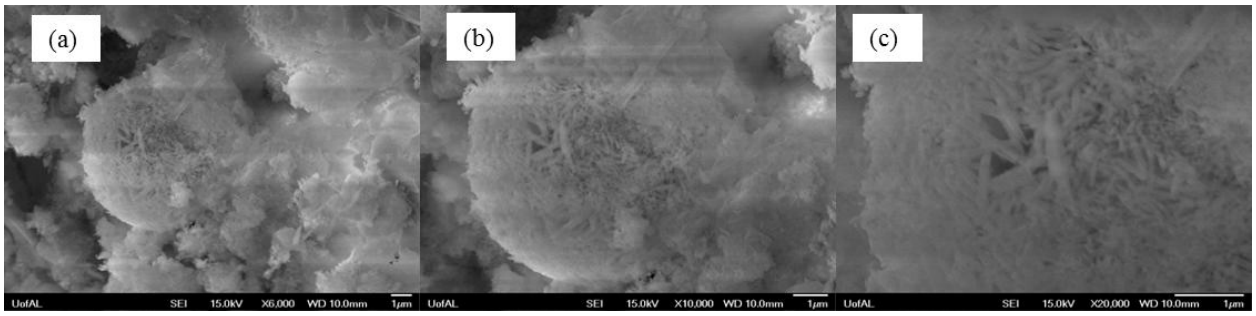

Fig. 11. SEM Images of Residue of Fly Ashes from Orlando after Dissolution Testing

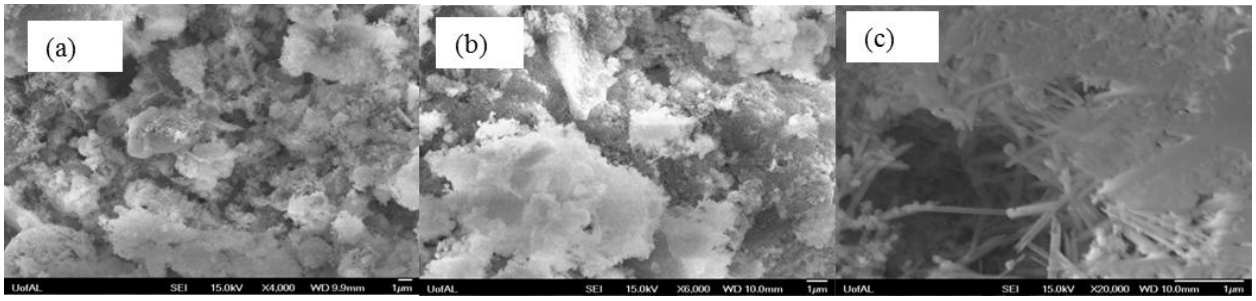

Fig. 12. SEM Images of Residue of Fly Ashes from Martin Lake after Dissolution Testing

The SEM images of the high calcium fly ash from Miller are shown in Fig. 13. It can be seen that significant amount of precipitant (portlandite) was produced (Fig. 13(a)) due to the high calcium content. For this reason, the dissolution degree measured for this fly ash is much lower than low-calcium fly ashes. Figure 13(c) also shows that the major mineral residue of this fly ash is mullite, same as other fly ashes.

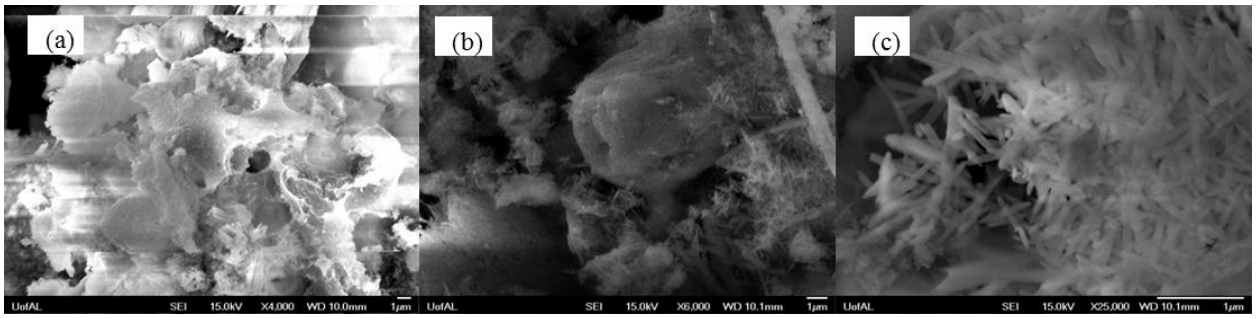

Fig. 13. SEM Images of Residue of Fly Ashes from Miller after Dissolution Testing

3.3. Effect of Alkalinity

Figure 14 shows the effects of the alkalinity of the activator on the produced geopolymers. In this figure and thereafter, normalized strength and modulus are calculated by dividing the compressive strength and modulus of a geopolymer specimen by that of the geopolymer made of fly ash from Gaston with the mix shown in Table 2. A clear correlation between the concentration of NaOH and the elastic modulus/compressive strength can be identified from this figure. Both the compressive strength and modulus increase with the concentration of NaOH, which echoes other researchers' results (Khale and Chaudhary, 2007).

3.4. Effect of Na_2O/Al_2O_3 Ratio

Figure 15 shows that both the compressive strength and the elastic modulus of the geopolymer specimens decrease very fast with the molar ratio of Na_2O/Al_2O_3 if molar ratio

Na_2O/Al_2O_3 is less than 0.9. Lower molar ratio of Na_2O/Al_2O_3 implies high content of Al_2O_3 in the system which can provide Al needed to form more geopolymer chains. Once the molar ratio Na_2O/Al_2O_3 is greater than 0.9, its effect on the strength of the produced geopolymer is very little, as shown in Fig. 15.

Because only the dissoluble portion of the fly ashes could have participated in the geopolymerization, it may be more accurate to express mechanical properties of the geopolymer specimens in term of the effective molar ratio of Na_2O/Al_2O_3, as shown in Fig. 16. The effective molar ratio of Na_2O/Al_2O_3 in Fig.16 is recalculated with only the dissolvable portion of fly ashes taken into account, and therefore.

3.5. Effect of SiO_2/Al_2O_3 Ratio

The relationship between the compressive strength/elastic modulus and the molar ratio of SiO_2/Al_2O_3 is shown in Fig.17. This relationship is more complicated than previous two cases shown in Figs.14 and 15. Both the compressive strength and the elastic modulus decreases with SiO_2/Al_2O_3 at small ratio (less than 3.4) and then increases sharply to their maximum somewhere between 3.6~3.8. After 3.8, both the compressive strength and the elastic modulus decrease with the molar ratio of SiO_2/Al_2O_3. This result agrees very well with the aforementioned study of Duxson et al. (Duxson et al., 2005). Their study showed that the compressive strength of the metakaolin based geopolymer reaches its maximum when the molar ratio of SiO_2/Al_2O_3 is 3.8. Figure 17 suggests that this optimal molar ratio of SiO_2/Al_2O_3 is also valid for fly ash based geopolymer. Similar to Fig.16, we can relate the mechanical properties of the geopolymer to its effective molar ratio of Na_2O/Al_2O_3 as shown in Fig. 18.

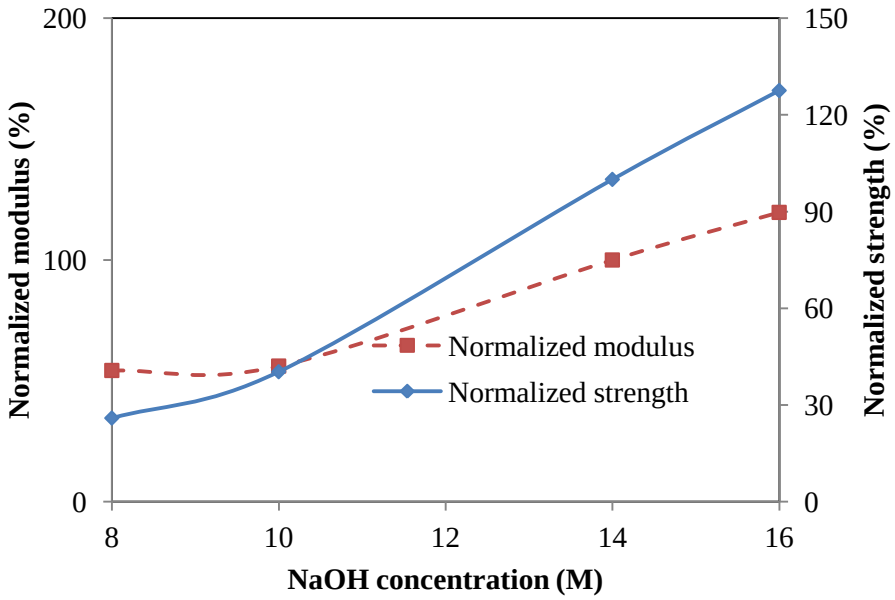

Fig. 14. Effect of Alkalinity of Activator on the Compressive Strength of the Produced Geopolymer

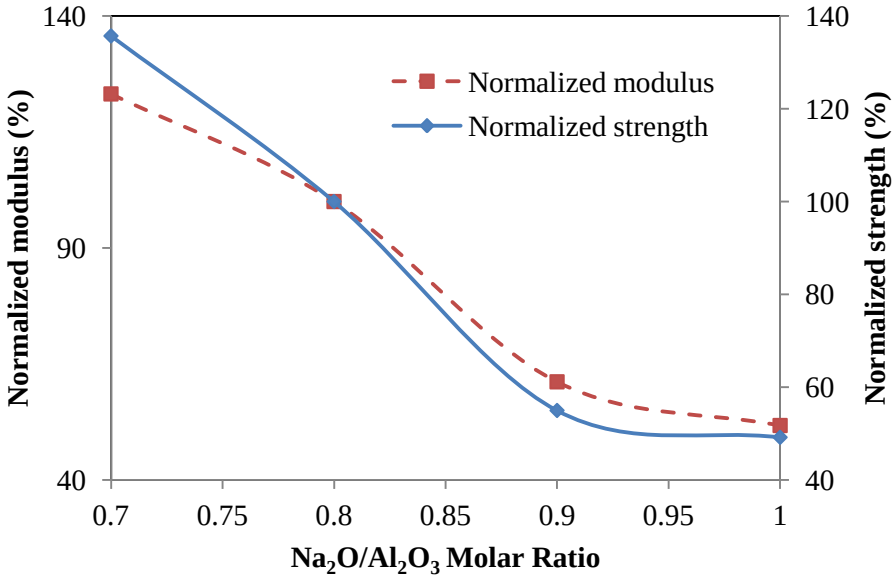

Fig. 15. Effect of Na_2O/Al_2O_3 Molar Ratio of Activator on the Compressive Strength of the Produced Geopolymer

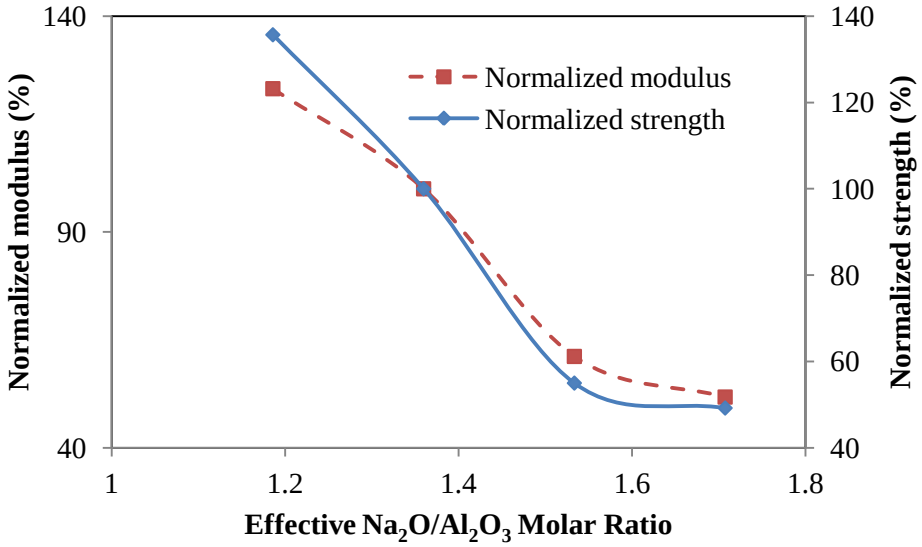

Fig. 16. Effect of Effective Na_2O/Al_2O_3 Ratio Based on Dissoluble Content

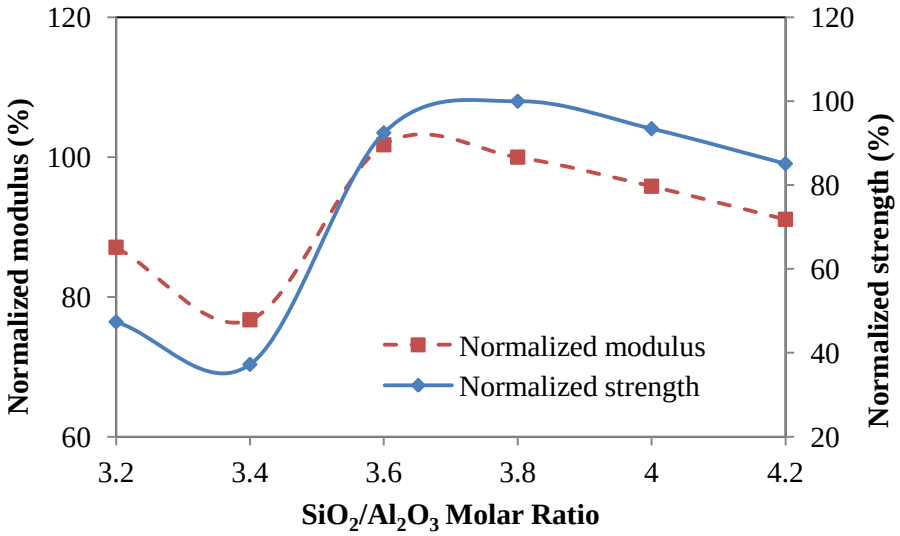

Fig. 17. Effect of SiO_2/Al_2O_3 Ratio Molar Ratio of Activator on the Compressive Strength of the Produced Geopolymer

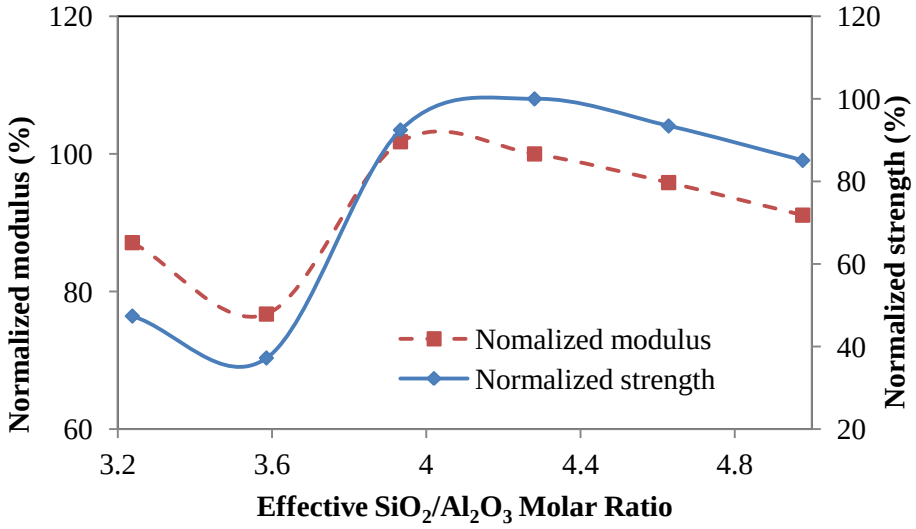

Fig. 18. Effect of Effective Molar Ratio of SiO_2/Al_2O_3 on the Compressive Strength of the Produced Geopolymer

3.6. Effect of Curing Time and Age

Compressive strength of geopolymer specimens made using fly ash from Gaston (mix design is given in Table 2) varying with the curing time are shown in Fig. 19. It can be seen that the compressive strength of the geopolymer does not change very much after 4 hours curing in the oven at 75°C, indicating a very high geopolymerization speed. Most of the geopolymerization can be finished within the first 4 hours. It also suggests that 48 hours curing used in this study is sufficient. This is in agreement with the observation of Hardjito et al. (Hardjito et al., 2004). They found that longer curing time could improve the geopolymerization and improve the strength, but longer than 48 hours did not help significantly. Longer curing time at high temperature could break the granular of geopolymer, due to dehydration and excessive shrinkage (Khale and Chaudhary, 2007).

Compressive strength varying with the age is shown in Fig. 20. Although Fig. 19 suggests curing at 75°C can accelerates the geopolymerization and that 4h curing is enough to finish most geopolymerization, the geopolymerization will not stop after curing for quite

a long time, as evidenced by Fig. 20. In this figure, we can find that the compressive strengths of the geopolymer specimens for either SiO_2/Al_2O_3=3.8 or 3.6 increase with age in the testing period (84 days). This is similar to the hydration of the Portland cement, which can take over many years. In fly ash geopolymer specimens, geopolymerization can occur as long as aluminosilicate sources and alkaline activator are present. With new reaction products covering the fly ash particles, it becomes more difficult for the amorphous materials in the fly ash to diffuse through the reaction products and participate in the geopolymerization process.

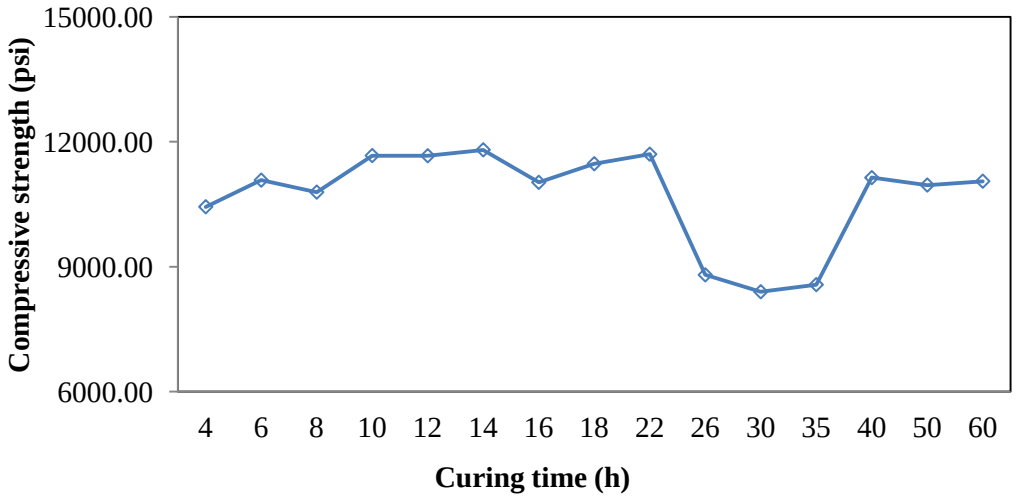

Fig. 19. Effect of Curing Time on the Strength of the Geopolymer Using Fly Ash from Gaston

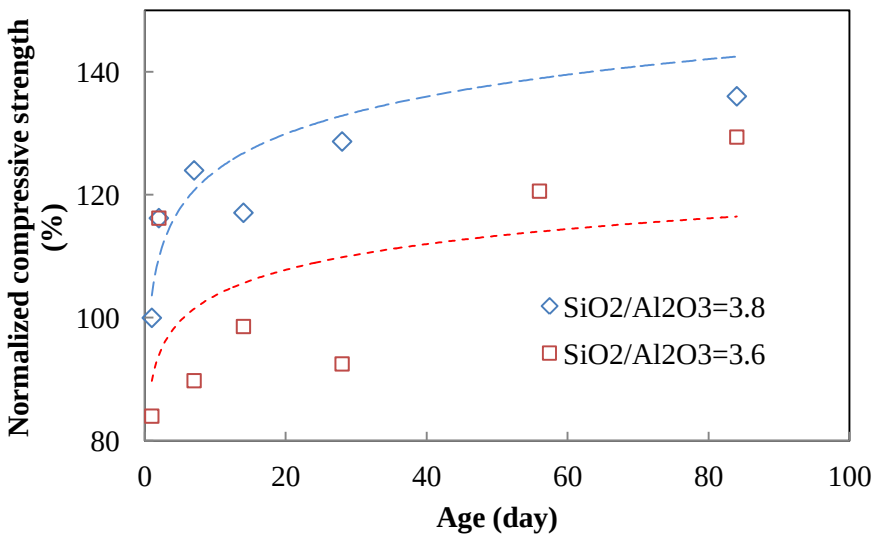

Fig. 20. Strength of Geopolymers Varying with Age

3.7. Effect of Fly Ash Sources

Compressive strengths of geopolymers specimens made using four fly ashes are presented in Fig. 21. It can be seen that geopolymer using fly ash from Gaston has the highest compressive strength. While geopolymer based on fly ash from Orlando is lower, even though the chemical composition and dissolution degree of this fly ash are very close to that of the fly ash from Gaston. The major reason causes this difference in strength is that the content of amorphous phases in Gaston fly ash is higher than that in Orlando fly ash, as indicated by the XRD spectra of these two fly ashes (Figs. 5 and 6). In this case, the dissolution degree as an indicator of the content of the amorphous phases in the fly ash is misleading. XRD spectrum may provide the most reliable information of the content of the amorphous phases in the fly ash. As anticipated, the strength of the geopolymer specimens based on fly ash from Martin Lake is much lower than those based fly ashes from Gaston and Orlando because its dissolution degree is much lower. Therefore, less amorphous materials participated in the geopolymerization, leading to lower compressive strength.

Among three low-calcium fly ashes, the fly ash from Gaston has the lowest calcium content and the one from Martin Lake has the highest. According to Van Jaarsveld et al. (van Jaarsveld et al., 2003), higher calcium content fly ash produces greater compressive strength. This suggests that the geopolymer based on fly ash from Martin Lake should have highest strength. Testing results in Fig. 21 show a trend exactly opposite to Van Jaarsveld et al.'s observation. This suggests that calcium content is not the only factor affecting the strength of the geopolymers. Geopolymer based on fly ash with higher calcium content could have lower strength if their dissolution degree is lower. Geopolymer specimens based on high calcium fly ash from Miller exhibit a higher compressive strength than that produced by Martin Lake although it has a low dissolution degree. This may be because some C-S-H was also formed in the geopolymer which can reinforce the geopolymer gel. As a result, its strength is higher.

Figure 22 shows the EDX spectrum of a small area in the geopolymer specimens based on the fly ash from Gaston. It can be seen that the major elements in this probing area are O (56.87 wt.%), Na (9.52 wt.%), Al (6.97 wt.%), and Si (15.36 wt.%), suggesting it is geopolymer gel.

Figure 23 (a) shows the microstructure of the geopolymer made of the fly ash from Gaston. A few unreacted fly ash residues can be clearly identified from this figure. They are all covered by some minerals. Element mapping shows that no or little Na element can be found on the surface of these fly ash residues, suggesting that the minerals covering the surface of the unreacted fly ash particles are non-reactive mineral in the fly ash, not geopolymer gel. Except the fly ash residues, other area shown in Fig. 23(a) is rich in Si, Al, and Na, as shown in Figs. 23(b), (c), and (f), indicating that geopolymer gel has been

produced. No or little Ca can be identified from this sample as shown in Fig. 23(d). This is not surprising since the fly ash from Gaston has very low Ca content. A shrinkage crack is also present which is very common for most geopolymer cured at elevated temperature.

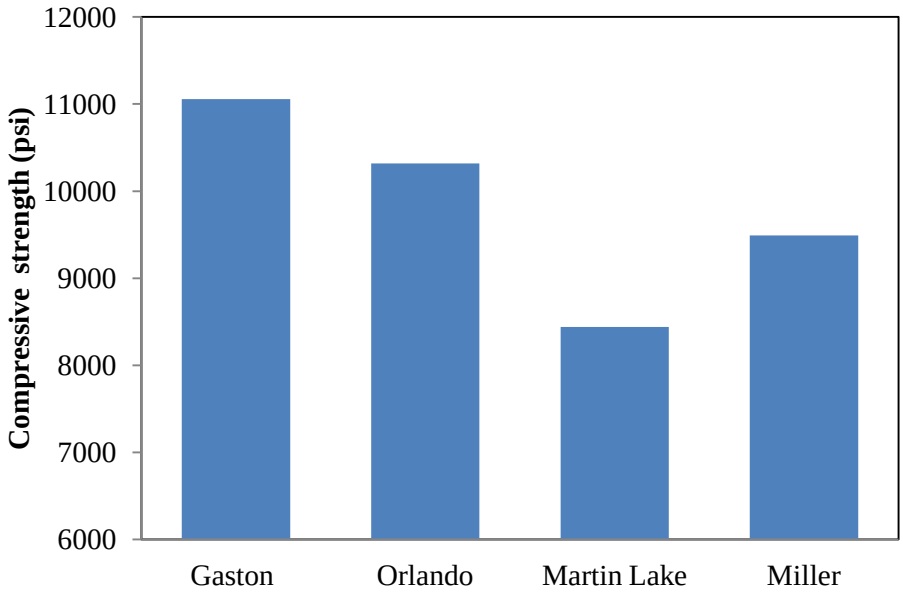

Fig. 21. Compressive Strengths of Geopolymers Made from Fly Ashes from Four Different Sources

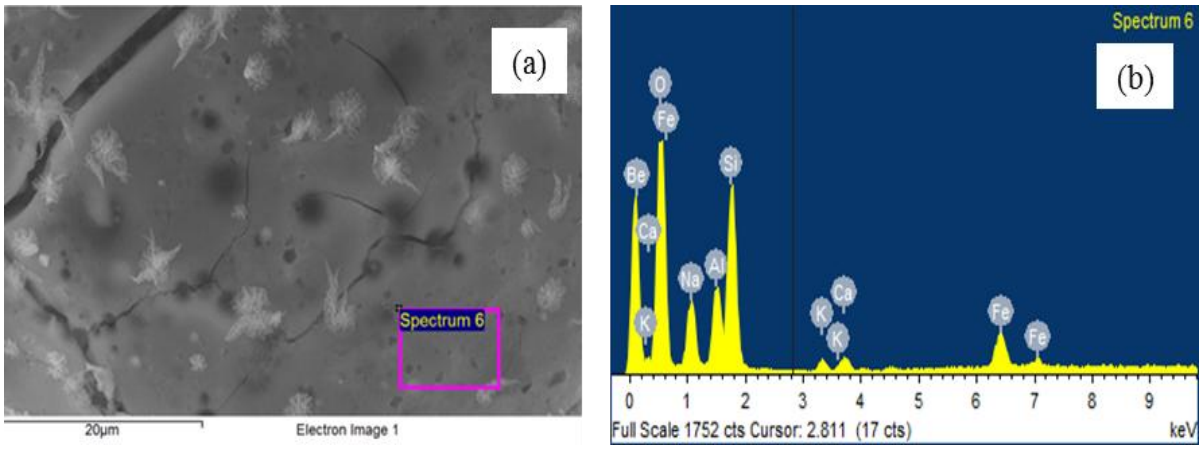

Fig. 22. Geopolymer Gel Produced Using Fly Ash from Gaston: (a) SEM Image; (b) EDX Spectrum

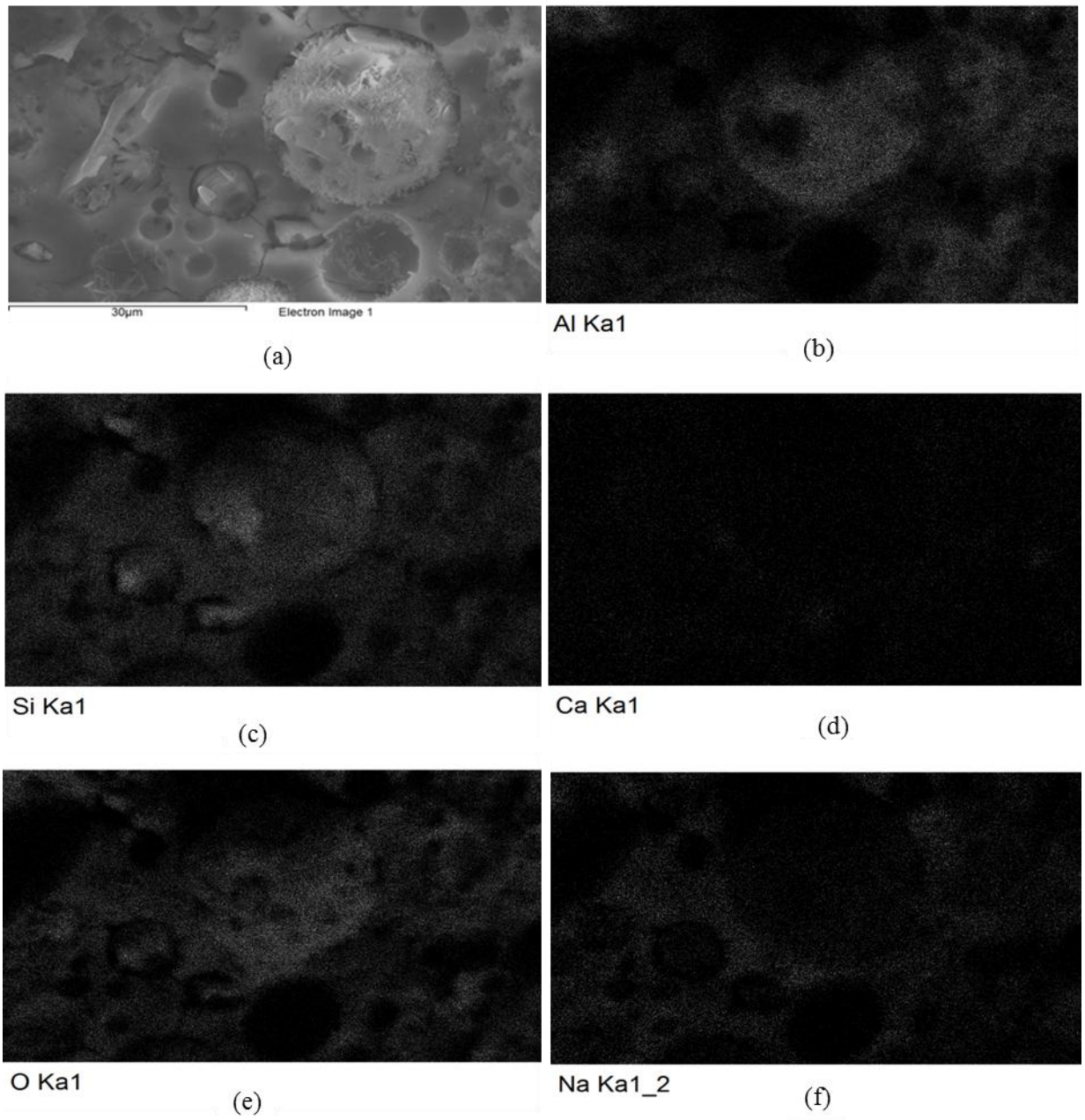

Fig. 23. SEM and Element Mapping of Geopolymer Using Fly Ash from Gaston: (a) SEM Image; (b) Al Mapping; (c) Si Mapping; (d) Calcium Mapping; (e) O Mapping; (f) Na Mapping.

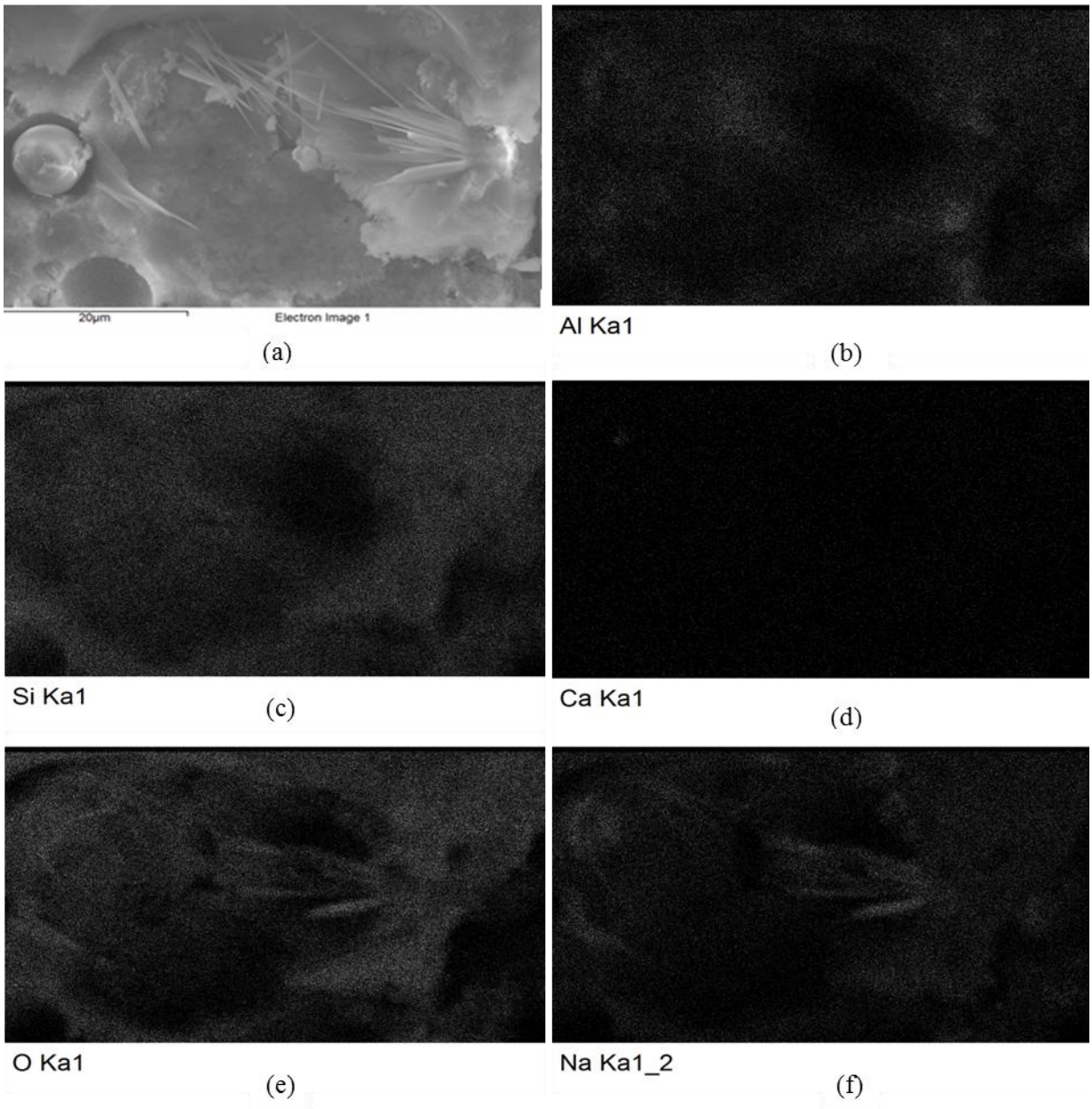

Fig. 24. SEM and Element Mapping of Geopolymer Using Fly Ash from Orlando: (a) SEM Image; (b) Al Mapping; (c) Si Mapping; (d) Calcium Mapping; (e) O Mapping; (f) Na Mapping.

Figure 24 shows the microstructure and element mapping of the geopolymer based on the fly ash from Orlando. Similar to the previous case, some unreacted fly ash can be found. Element mapping shows that geopolymer gel is the major product in the observed area.

Some needle-like crystals can be seen in this image. Element mapping shows that these crystals are rich in Na and O and contain no or little Ca, Si, and Al. Therefore, most likely, these crystals are unreacted alkaline NaOH.

Figure 25 shows the microstructure and element mapping of the geopolymer samples based on the fly ash from Martin Lake. Some unreacted fly ash particles can be found in this geopolymer sample. Unlike in the previous two cases in which part of the fly ash particles have been dissolved, the fly ash particles present in this sample have smooth surfaces, indicating they did not participate in any chemical reaction. This can be confirmed by the element mapping. As shown in Figs. 25(d), and (f), these particles are rich in Ca but contain no or little Na. This observation agrees very well with the dissolution testing result. It also explains why the geopolymer based on fly ash from Martin Lake is weaker. Figure 25(d) shows that most calcium was not leached out of the fly ash and still locked within the fly ash particles. Therefore, no binder other than geopolymer can be found in this sample even though the fly ash contains 8.03% of CaO.

Figure 26 shows the microstructure and element mapping of the geopolymer sample based on high calcium fly ash from Miller. More shrinkage cracks can be found in this sample which could be caused by the high calcium content of the fly ash. This may explains why the compressive strength of this geopolymer is weaker than that of the geopolymers based on fly ashes from Gaston and Orlando. A calcium-rich area has been identified in Fig. 26(a) and (d). In this area, no or little Na or Al was found while Si is abundant. Therefore, very likely, C-S-H is produced in this area due to the high calcium content in the fly ash, which can reinforce the geopolymer gel, and make it stronger than the geopolymer based on fly ash from Martin Lake.

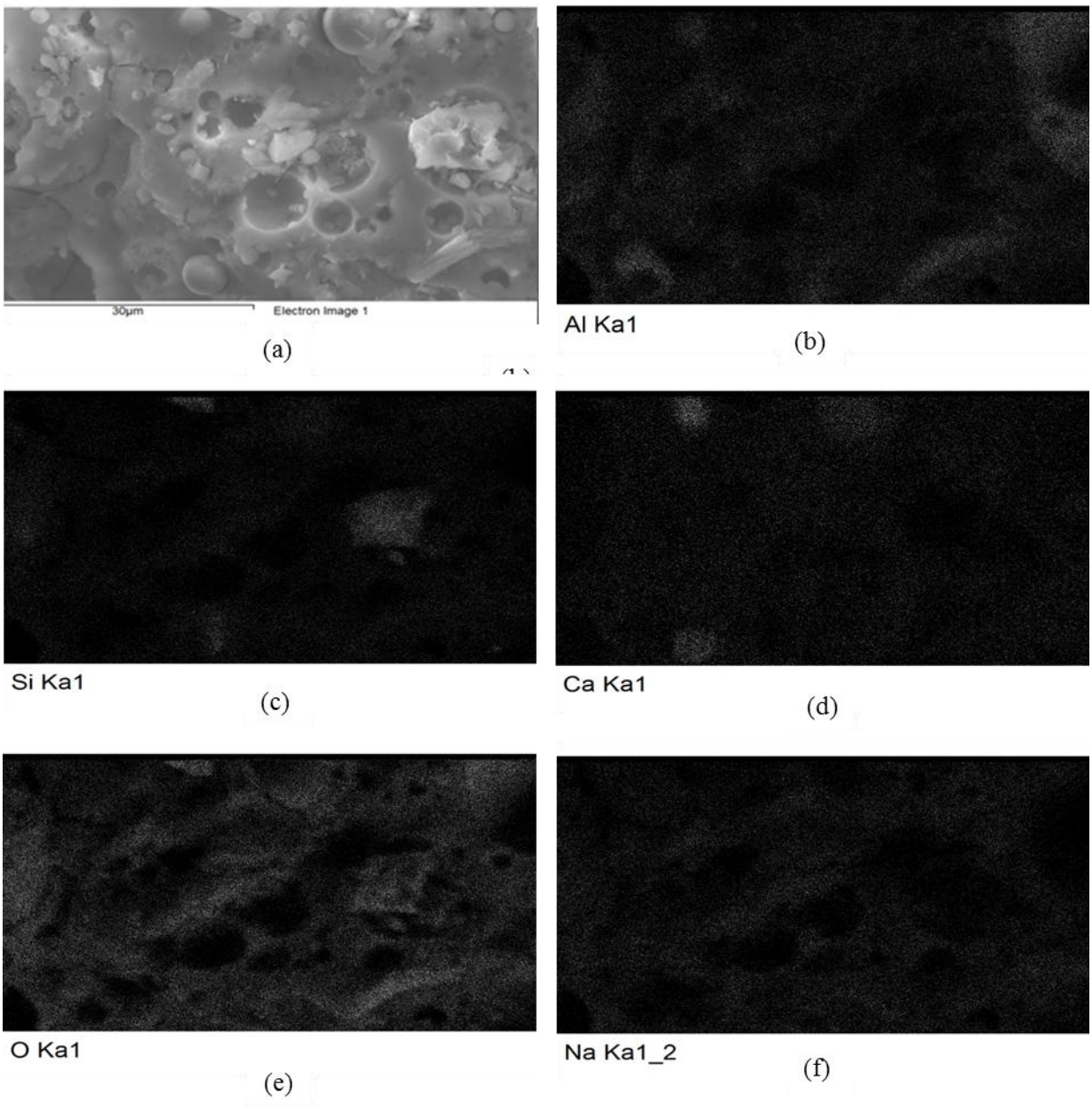

Fig. 25. SEM and Element Mapping of Geopolymer Using Fly Ash from Martin Lake: (a) SEM Image; (b) Al Mapping; (c) Si Mapping; (d) Ca Mapping; (e) O Mapping; (f) Na Mapping.

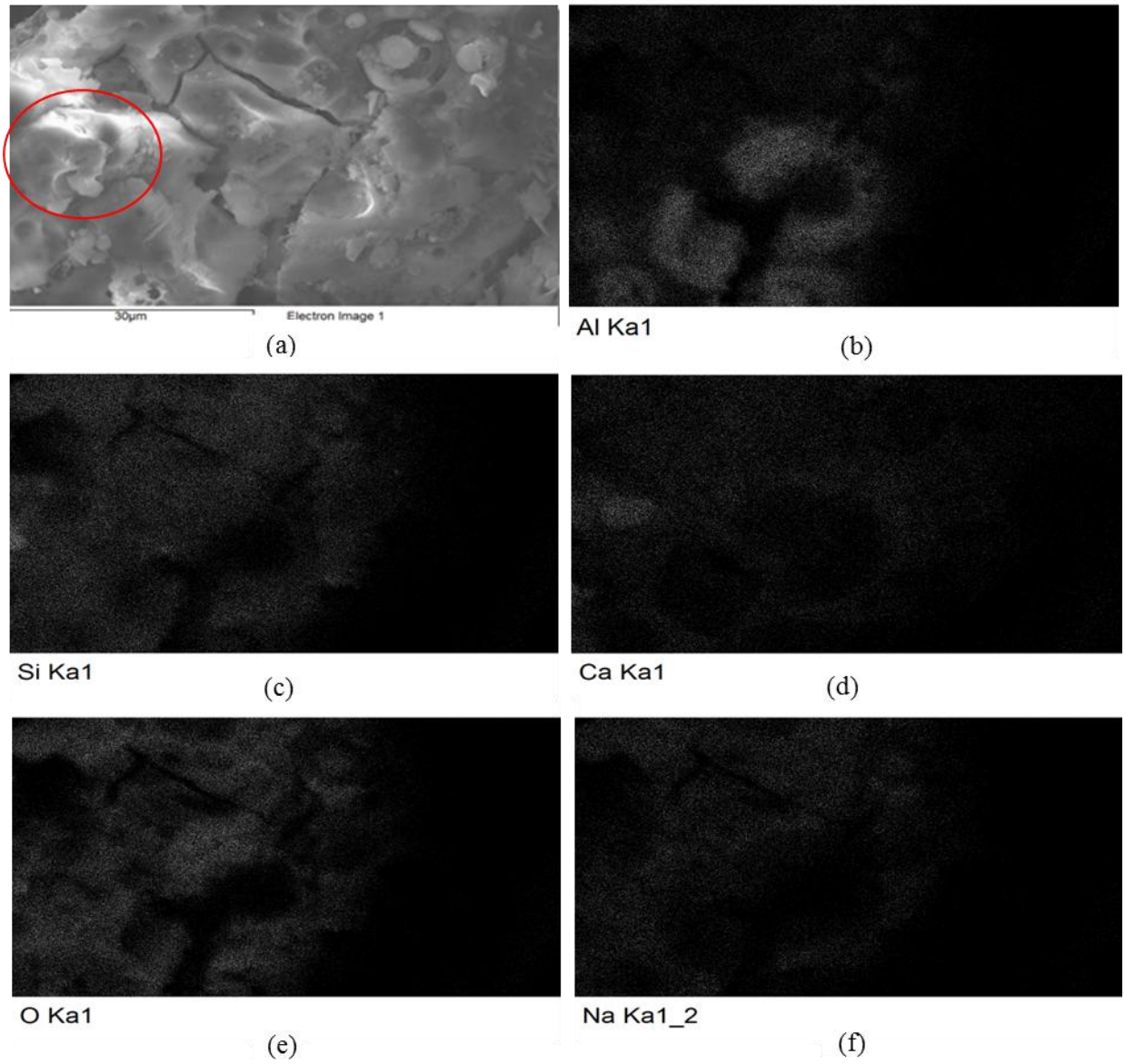

Fig. 26. SEM and Element Mapping of Geopolymer Using Fly Ash from Miller: (a) SEM Image; (b) Al Mapping; (c) Si Mapping; (d) Ca Mapping; (e) O Mapping; (f) Na Mapping.

4. CONCLUSIONS

In this study, fly ashes from four different sources were used to synthesize Geopolymer mortars. Comprehensive experimental programs have been carried out to characterize the fly ashes, to examine the critical factors affecting on the mechanical properties of geopolymers,

and to evaluate the potentials of four locally available fly ashes as source materials for geopolymers. The following conclusions can be drawn based on the experimental studies:

Fly ashes from four different sources exhibit quite different dissolution degrees, which will affect the properties of the geopolymer using these fly ashes as source materials. Fly ash from Gaston has highest reactive content and is the best source material to make geopolymer.

Dissolution degree might not be a reliable indicator of the content of the reactive materials in the fly ash. New crystalline or fast precipitants can be produced during the dissolution testing, which can make the measured dissolution degree deviate from its real value.

The alkalinity plays an important role in its compressive strength development. Compressive strength of the geopolymer increases with the alkalinity of the activator. However, higher alkalinity may increase the cost and carbon footprint of the produced geopolymer.

The compressive strength of geopolymers decreases with the molar ratio of Na_2O/Al_2O_3 when the molar ratio of Na_2O/Al_2O_3 is less than 0.9. Above that, its effect is very little.

The compressive strength of geopolymers decreases first and then increases with the gross molar ratio of SiO_2/Al_2O_3 and reaches its maximum at 3.6~3.8, and then decreases again. The optimal molar ratio obtained in this study is in good agreement with other findings in the literature.

Geopolymer samples cured at 75°C gain most of its strength after four hours curing.

The compressive strengths of geopolymer specimens increase with age during the whole testing period, suggesting geopolymerization takes a very long time.

The compressive strength of the geopolymer decreases with the calcium content of the source fly ash, which is opposite to the observation reported in the literature. The major reason causes this contradictory is that the dissolution degrees are different in each fly ashes. Therefore, calcium content cannot be used solely to predict the strength of the geopolymer.

Geopolymer made from low-calcium fly ash with higher content of reactive materials has better strength. Among all fly studied in this research, fly ash from Gaston is the most suitable to synthesize geopolymer. The geopolymer made from this fly ash has the highest strength because of its highest content of reactive materials.

High-calcium fly ash from Miller can be used to synthesize geopolymer too. Its reaction products include some C-S-H.

REFERENCES

ASCE. 2013. "2013 Report Card for America's Infrastructure." http://www.infrastructurereportcard.org/a/documents/2013-Report-Card.pdf.

ASTM C39-05. 2005. "Test Method for Compressive Strength of Cylindrical Concrete Specimens". ASTM International.

ASTM C618-05. 2005. "Specification for Coal Fly Ash and Raw or Calcined Natural Pozzolan for Use in Concrete". ASTM International.

Chindaprasirt, P., T. Chareerat, and V. Sirivivatnanon. 2007. "Workability and Strength of Coarse High Calcium Fly Ash Geopolymer." *Cement and Concrete Composites* 29 (3): 224–29.

Duxson, Peter, John L. Provis, Grant C. Lukey, Seth W. Mallicoat, Waltraud M. Kriven, and Jannie S.J. van Deventer. 2005. "Understanding the Relationship between Geopolymer Composition, Microstructure and Mechanical Properties." *Colloids and Surfaces A: Physicochemical and Engineering Aspects* 269 (1-3): 47–58.

Hardjito, D., S. E Wallah, D. Sumajouw, and B. V. Rangan. 2004. “Factors Influencing the Compressive Strength of Fly Ash-Based Geopolymer Concrete.” *Civil Engineering Dimension* 6 (2). http://puslit2.petra.ac.id/ejournal/index.php/civ/article/viewArticle/16116.

Khale, Divya, and Rubina Chaudhary. 2007. “Mechanism of Geopolymerization and Factors Influencing Its Development: A Review.” *Journal of Materials Science* 42 (3): 729–46.

Kuhlmann, K., and H. Paschmann. 1997. “The Ecological Position of Cement and Concrete.” *ZKG International* 50 (1): 1–8.

Phair, John W. 2006. “Green Chemistry for Sustainable Cement Production and Use.” *Green Chemistry* 8 (9): 763.

Provis, J.L., P. Duxson, J.S.J. Van Deventer, and G.C. Lukey. 2005. “The Role of Mathematical Modelling and Gel Chemistry in Advancing Geopolymer Technology.” *Chemical Engineering Research and Design* 83 (7): 853–60.

Provis, J.L., and J.S.J. van Deventer. 2007. “Geopolymerisation Kinetics. 2. Reaction Kinetic Modelling.” *Chemical Engineering Science* 62 (9): 2318–29.

Silva, P. De, K. Sagoe-Crenstil, and V. Sirivivatnanon. 2007. “Kinetics of Geopolymerization: Role of Al_2O_3 and SiO_2.” *Cement and Concrete Research* 37 (4): 512–18.

Van Jaarsveld, J. G. S., J. S. J. van Deventer, and G. C. Lukey. 2002. “The Effect of Composition and Temperature on the Properties of Fly Ash- and Kaolinite-Based Geopolymers.” *Chemical Engineering Journal* 89 (1-3): 63–73.

Van Jaarsveld, J. G. S., J. S. J. van Deventer, and G. C. Lukey. 2003. “The Characterisation of Source Materials in Fly Ash-Based Geopolymers.” *Materials Letters* 57 (7): 1272–80.

Van Oss, Hendrik G., and Amy C. Padovani. 2003. “Cement Manufacture and the Environment Part II: Environmental Challenges and Opportunities.” *Journal of Industrial Ecology* 7 (1): 93–126.

NONLINEAR FRACTURE BEHAVIOR OF FLY ASH BASED GEOPOLYMER USING SPLITTING WEDGE TESTING AND DIGITAL IMAGINE CORRELATION TECHNIQUE

ABSTRACT

Geopolymer synthesized with industrial wastes such as fly ash has the potential to replace Ordinary Portland cement as a green binder for concrete. Although extensive studies have been carried out on geopolymer, its fracture behavior has received very little attention. This study examines the nonlinear fracture behavior of a fly ash based geopolymer mortar using splitting wedge testing method. A full-field displacement measurement technology, digital imagine correlation (DIC) system is used to measure the full-field displacement of the fracture specimen and to determine the crack opening displacements. The measured full-field displacement clearly shows that a fracture process zone (FPZ) exists ahead of the major crack, suggesting that the fracture of the geopolymer mortar follows a nonlinear behavior similar to the OPC based concrete. By assuming a bi-linear constitutive law for this FPZ, a closed-form solution of the fracture specimen is obtained using a crack hinge model. The bi-linear law can then be determined by least-square fitting the analytical solution and the testing data. Testing result shows that the geopolymer mortar has lower fracture energy compared with OPC-based concrete with similar strength. By using crack opening displacement at different locations of the specimen, the present method can study the size effect of the fracture of quasi-brittle materials by using only one specimen, which can save enormous time and energy needed in existing methods. Measured fracture energy

of the geopolymer mortar exhibits strong size dependence, suggesting that larger specimen is needed to determine the intrinsic fracture toughness of the geopolymer.

1. INTRODUCTION

Geopolymers are amorphous three-dimensional alumino-silicate binder materials. They can be synthesized by mixing source material (alumino-silicate reactive materials such as metakaolin, fly-ashes) and an alkaline activator (strong alkaline solutions such as NaOH or KOH) and then curing at room or elevated temperature. Compared with OPC, geopolymers possess the following advantages: a) less energy consumption and CO_2 emission (20% of the carbon dioxide emissions produced in the manufacture of OPC) during manufacture, b) higher strength and much less shrinkage, c) lower permeability (comparable to natural granite), and d) substantially higher resistance to fire and acid attacks. Geopolymers are considered as "green materials" and strong candidates to replace OPC in selected applications leading to more sustainable infrastructure system.

Extensive studies have been carried out on geopolymer mortars/concretes in last two decades, most of these works focus on the strength properties of the geopolymers. The fracture behavior of geopolymers, however, has received very little attention. Fracture properties are critical to many applications of the geopolymer concretes and should be studied for their adoption for real applications.

Two methods have been used to measure the fracture toughness of geopolymer concrete: strength intensity factor method (Sarker et al. 2013) in which the critical strength intensity factor is measured as the fracture toughness, and RILEM method in which the work-of-fracture (RILEM TC-50 FMC 1985) is measured as the fracture toughness (Pan et al. 2011). However, geopolymer mortar or concrete is a heterogeneous material. Substantial energy

dissipation occurs during the fracture of the geopolymer mortar/concrete, resulting in non-linear behavior during loading. Stress intensity factor method which is built on linear fracture mechanics ignores the nonlinear behavior and therefore is not effective for geopolymer mortar or concrete. RILEM work-of-fracture method can account for the nonlinear behavior of the fracture; however, the values determined by this method are dependent on the size and shape of the test specimen. This size effect is caused by the nonlinear FPZ. If the behavior of the FPZ can be directly measured, then shortcomings of both existing methods can be overcome. To this end, a new approach to determine the non-linear fracture behavior of geopolymer mortar using splitting wedge specimen together with digital image correlation technique is proposed.

2. MATERIALS AND METHODS

2.1 Geopolymer Mortar

Fly ash from Gaston, a coal-burning power plant in Alabama was used to synthesize geopolymer. The chemical composition of the fly ash is shown in Table 1. In mix design of the geopolymer is shown in Table 2. The produced specimens were cured in oven for 48 hours at 75 °C. The measured compressive strength of the specimen is 77 MPa (11 ksi).

Table 1. Chemical Composition of Fly Ashes

Source	SiO_2	Al_2O_3	Fe_2O_3	SO_3	CaO	Moisture	LOI	Na_2O
Gaston	50.38%	27.20%	9.14%	0.30%	2.49%	0.14%	2.95%	0.69%

Table 2. Mix Design of Geopolymer Using Fly Ashes from Gaston (in Mass)

Ingredients	fly ash	Sodium silicate	NaOH solution	super plasticizer	Sand
Content (wt%)	24.48%	8.68%	6.84%	2.00% of fly ash	60%

2.2. Wedge Splitting Test

Commonly used methods to test the fracture behavior for concrete include three point bending test (TPBT) and compact tension (CT) test. In this study, a Wedge Splitting Test (WST) is adopted. This test was first proposed by Linsbauer and Tschegg (Linsbauer and Tschegg, 1986) and further developed by Brühwiler and Wittmann (Brühwiler and Wittmann, 1990) for stable fracture test on concrete. It has been used by various researchers (Denarié et al., 2001; Skoček and Stang, 2008; Skoček and Stang, 2010). That WST is chosen in this study is because of its advantages over other popular fracture testing methods (TPBT and CT). Firstly, the testing set up for WST is very simple. Second, the specimen is easy to fabricate and therefore, even can be done on-site or drilled from the structure. Lastly and most importantly, the crack propagation in the specimen is stable, which eliminates the difficult task to control the crack growth in the other existing method such as TPBT.

The geopolymer mortar specimen (Fig. 1(a)) has a size of 24.5 mm (1") in thickness, 147 mm (6") in length and 70 mm (2 and 3/4") in height, as shown in Fig.1. A pre-crack with length of 15.9 mm (5/8") is created on the specimen before the testing. This specimen is placed on a roller support, which is fixed on the lower plate of the MTS machine (Fig. 1(b)). A stiff steel profile with two identical wedges fixed at the upper plate of the testing machine is used to load the specimen. During the test, the applied load P_v (vertical component) and the crack opening displacement (COD) are measured. The splitting force P_{sp} which is the horizontal component of the force acting on the specimen P_v can be generated to drive two rollers apart (Fig. 1(c)), leading to a mode I fracture in the geopolymer mortar specimen. The testing could be displacement controlled, or crack opening displacement controlled (an additional clip gauge for CMOD measurement is needed). Brühwiler and Wittamann

(Brühwiler and Wittamann, 1990) showed that when the following condition was met, WST was stable under displacement control:

$$l_{ch} > K \cdot L \cdot \left(k_p/k_M + 1\right), \quad (1)$$

where l_{ch} is the characteristic length of the material, k_p and k_M are the stiffness of the specimen and the loading machine; K is the constant depending on the specimen geometry; and L is the cantilever length of the wedge splitting specimen. They (Brühwiler and Wittmann, 1990) also showed that stable fracture could be performed on all materials, except the "completely brittle one".

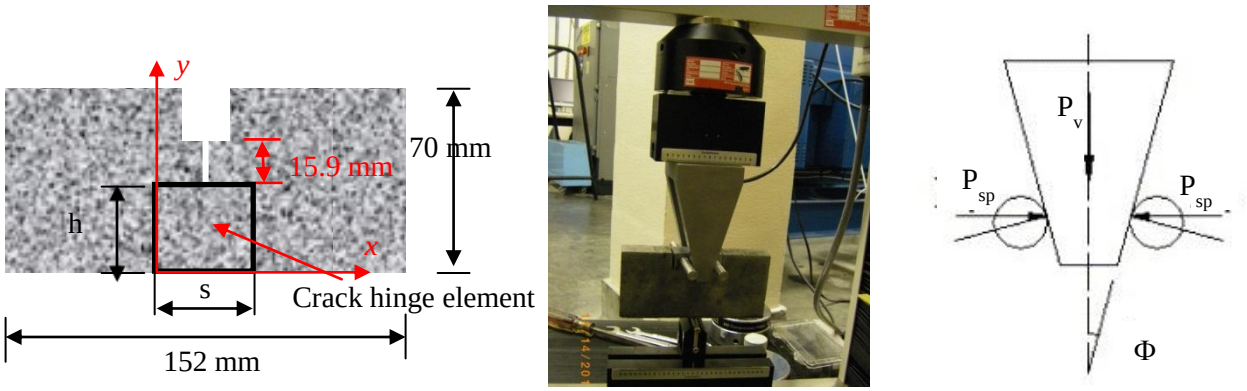

(a) (b) (c)

Fig. 1. Wedge Splitting Test: (a) Specimen; (b) Loading Setup; (c) Loading

2.3. Crack Opening Displacement (COD) Measurement Using DIC

As a heterogeneous material, geopolymer mortar has complicated fracture behavior, especially the microscopic behavior at the FPZ, in which the microstructural features interact with the failure process. Therefore, a robust full-field measurement method, Digital Imagine Correlation (DIC) method is used to directly observe the fracture process and measure the crack opening of the specimen. Although there are some other high-resolution full-field measurement methods such as Moire interferometry, electronic speckle patter

interferometry, and laser holographic interferferometry, they are difficult to apply on geopolymer concrete. In addition, these methods require a vibration-free environment, which is difficult to achieve around mechanical testing machines.

2.3.1 Working Principle of the DIC system

DIC system was first studied by researchers in University of South Carolina in the early 1980s (Peters and Ranson, 1982; Sutton et al., 1983; Chu et al., 1985). It is a full-field deformation measurement technique that extracts the full-field displacement data by comparing a pair of digital images of a specimen surface before and after deformation. In this method, image of the body could be represented by a discrete function: value between 0 and 255 of its grey levels. In order to correlate the intensity distribution of the deformed image to the undeformed image, the images are divided into small subsets called pattern (see the initial pattern ABCE in Fig. 2). The displacement field is assumed homogeneous inside each pattern. A discrete function *f(x, y)* is used to represent the initial image of the body before deformation, which is transformed in another discrete function *f*(x*, y*)* after deformation, as shown in Fig. 2. Then the cross correlation coefficient can be calculated as:

$$C = 1 - \frac{\Sigma[f(x,y)\cdot f^*(x^*,y^*)]}{[\Sigma[f^2(x,y)\cdot f^{*2}(x^*,y^*)]]^{1/2}}. \quad (2)$$

By minimizing the correlation function over a subset image region, in-plane displacements, *u* and *v*, and the displacement gradients, *du/dx*, *du/dy*, *dv/dx*, and *dv/dy* are determined, which are in turn used for further analysis.

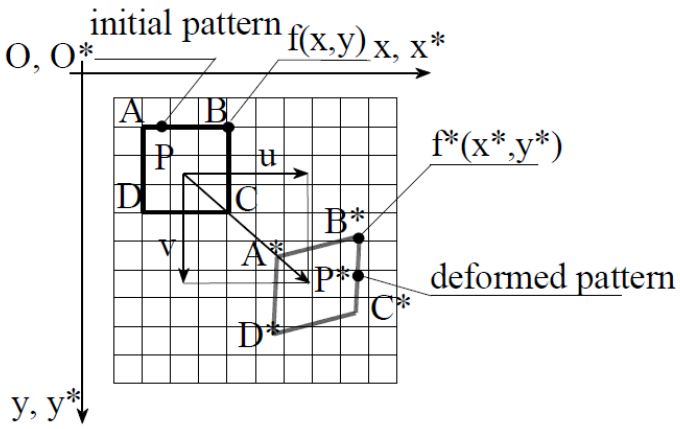

Fig. 2. Pattern, Displacements, and Discrete Functions Used in DIC

2.3.2. Full-field Displacement Measurement of the Geopolymer Fracture Specimen Using DIC

To use DIC to measure the full-field displacement of the geopolymer fracture specimens, one or two cameras are used to capture images of the surface of the specimen. By painting the surface with speckles, points in different images can be correlated by pattern matching, which provides us a way to track the movement of the points. If a reference image is taken when the specimen is unloaded, then the strain can be calculated from the displacement field. Compared with the strain gauge, DIC has an obvious advantage: it can obtain the displacement for every point in the area of interest. Also, it does not have an upper bound of the strain it can measure. The precision of the DIC system depends on the optical lens and the CCD. It could be as high as 10^{-5} times the size of a pixel. With DIC, the whole displacement field of the specimen can be obtained, from which the difference in horizontal displacement of any arbitrary point can be calculated. If two points are chosen on the crack surface, then the difference in their horizontal displacements gives the crack opening displacement (COD) at these two points.

However, a couple of challenges must be overcome to use the DIC with the loading machine. The first challenge is to find the corresponding COD for a specific load. This is because that the COD and the mechanical load are measured by the DIC and the material testing machine, respectively, which do not communicate with each other directly. This challenge was overcome by using time synchronization. To do this, the clocks of two computers that were used to control MTS and DIC were synchronized before the start of the test. A program was written to read the corresponding load from MTS records for each COD read from DIC. This worked very well by using the low loading rate of the MTS and the high time resolution (in seconds) of the DIC system.

The second challenge is to set up the coordinate system used by the DIC system in alignment with the computation coordinate system. The origin of the DIC coordinate system is at the center of two cameras with the line through centers of two cameras as *x*-axis. This system is different from the one used in the computation, in which the back boundary (bottom line of the uncracked side of the specimen) is chosen as the *x* axis and the crack path is chosen as the *y*-axis. This challenge was overcome by coordinate system transform function provided by the software of the DIC system. To do this, a small speckle was chosen as the reference point, which needed to be identified on both the DIC images and the specimen. Its coordinates measured with a caliper were used as inputs to perform coordinates transformation using the DIC system.

Figure 3 shows the full field measurement results of a geopolymer mortar specimen. Figure 3(a) shows the displacement field before any FPZ can be identified. In Fig. 3(b), the applied load is high enough to generate a clear FPZ ahead of the pre-crack. Similarly to the OPC based mortars/concrete, the FPZ in geopolymer is much localized. The crack opening

within the FPZ is presented in Fig. 3(c). The splitting force vs. COD can then be obtained as shown in Fig. 4. It can be seen that the whole softening branch of this curve was captured, suggesting that stable fracture propagation was obtained by using WST method during the test.

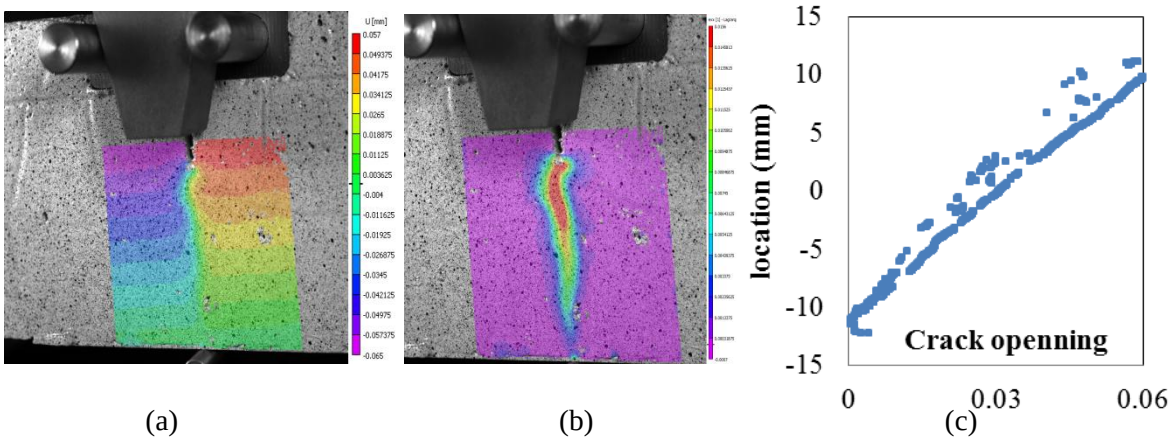

(a) (b) (c)

Fig. 3. Full-Field Displacement Measurement Using DIC: (a) Displacement Field before FPZ Is Formed; (b) FPZ Identified by DIC; (c) Crack Opening within the FPZ.

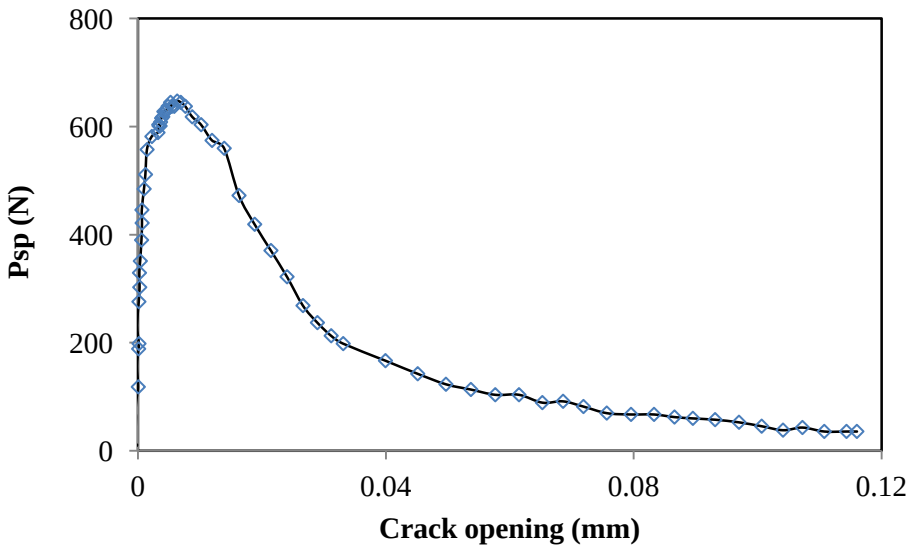

Fig. 4. Splitting Force Varying with Crack Opening Displacement Determined by DIC

2.4. Inverse Analysis for the Traction-Separation Law of the FPZ

2.4.1. Traction-Separation Law

As aforementioned and demonstrated by the full-field displacement measurement shown in Fig. 3, the size of the FPZ of the geopolymer mortar specimen is not small compared with the size of the specimen. As a result, classical linear elastic fracture mechanics (LEFM) is inapplicable here due to the large nonlinear process zone (Bažant 2000). Hillerborg et al. (Hillerborg et al., 1976) extended the Cohesive Zone Model (CZM) (Barenblatt 1959) to the nonlinear fracture of concrete. In CZM, the locally damaged materials forming a narrow band of localized deformation may be modeled by nonlinear springs which represent the major physical variables. Compared with LEFM, which ignores the microscopic details and discloses little what happens within the damage zone, the CZM takes the behavior of FPZ into consideration and provides a way to examine the "inner problem" of understanding, characterizing and modeling the failure processes that actually lead to energy dissipation.

Traction-separation law is used to model the constitutive relationship in FPZ. A number of traction-separation laws, including linear (Hillerborg 1976), bilinear (Roelfstra and Wittmann, 1986; Wittmann, 1986), trilinear (Cho et al., 1984), and exponential (Gopalaratnam and Surendra, 1985) softening curve, have been used to model concrete materials. Among them, the bilinear softening relationship (Fig. 5) has been used extensively and is the model of choice in this work.

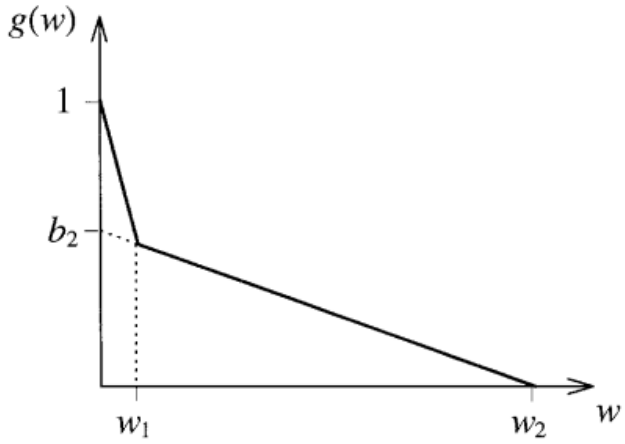

Fig. 5. Bi-linear Track-Separation Law of Geopolymer Mortar

To retrieve the bilinear traction-separation law of the geopolymer mortar from the SWT, an inverse analysis procedure is established. The constitutive law of the geopolymer mortar can be written as

$$\sigma = \begin{cases} E\,\epsilon,\ pre-cracking \\ \sigma(w) = g(w) f_t,\ cracking \end{cases} \tag{3}$$

where σ and ε are the stress and strain, respectively; w is the COD; E and f_t are the Young's modulus and the uni-axial tensile strength of the geopolymer, respectively. In the bi-linear model (as shown in Fig.5), the softening function *g(w)* can be written as

$$g(w) = a_i w + b_i \ (i = 1, 2). \tag{4}$$

The relationship of the parameters shown in Fig. 5 can be easily obtained as

$$b_1 = 1, w_1 = \frac{1-b_2}{a_1-a_2}, w_2 = \frac{b_2}{a_2}\,. \tag{5}$$

2.4.2. Crack Hinge Model

Crack Hinge Model was developed by Ulfkjær *et al*. (Ulfkjær et al., 1995). This model gives a closed-form solution of the fracture of concrete specimen and enjoys many advantages such as simplicity and computational efficiency. In this model, the portion of the

specimen near the crack (the rectangular area indicated in the specimen shown in Fig. 1(a)) is modeled as a hinge element, which consists of two rigid plates connected by a series of independent springs as shown in Fig.6. As shown in Fig. 6(a), the hinge element has a length of *s* and a depth of *h*. This element can also be viewed as a beam segment to which a bending moment *M* and an external axial force *N* are applied. The deformation of the hinge element is given by half of the angular deformation φ and the depth of the neutral incremental strip y_0, as shown in Fig. 6(b). Take a strip from the hinge element at a distance of *y* from the top of the element, as shown in Fig. 6(b). After deformation, the length of this strip becomes $s + u(y)$, where $u(y)$ is the displacement of the strip (Fig. 6(b)).

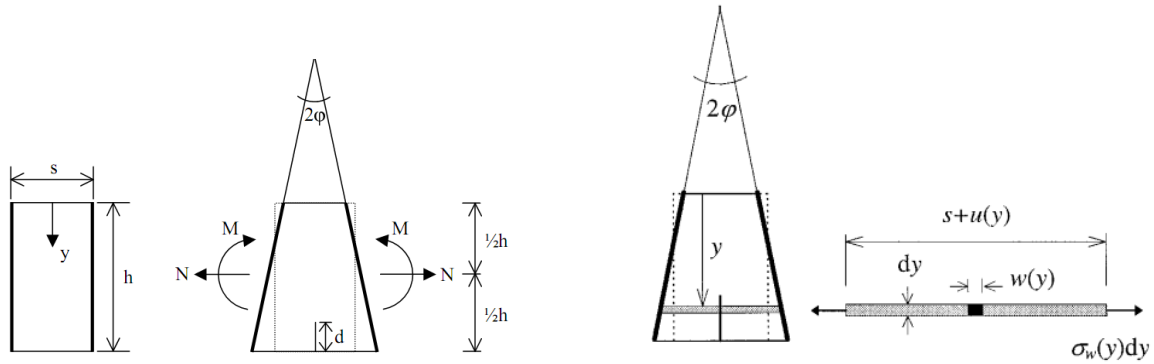

(a) (b)

Fig. 6. Crack Hinge Model of Concrete Fracture: (a) Concrete Beam before Cracking; (b) Concrete Beam after Cracking (Olesen 2001)

According to Crack High Model, the crack development process can be divided into four phases as shown in Fig. 7 (Olesen 2001):

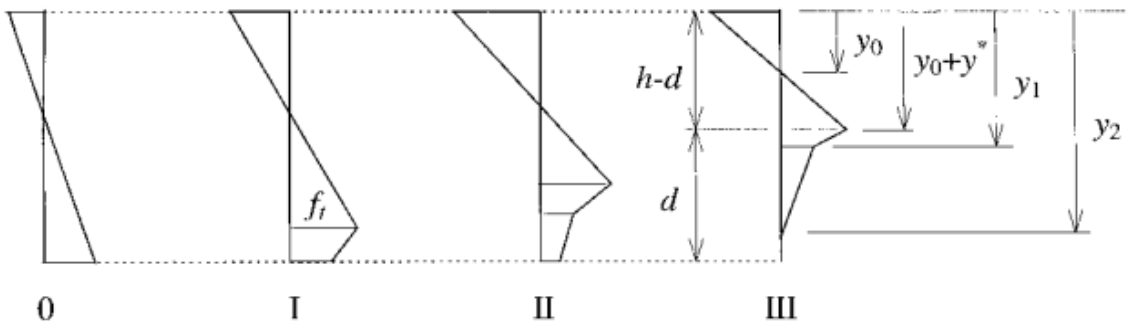

Fig. 7. Crack Development Phases according to Crack High Model (Olesen 2001)

Phase 0 is the elastic process in which the stress in outer fiber is below its tension strength.

Phase I is the fictitious crack development process, in which the stress in outer fiber passes its tensile strength and falls back below it, and the deformation is smaller than w_1.

Phase II is the fictitious crack development process, in which the deformation in outer fiber passes w_1 but not w_2.

Phase III is the real crack development, stress in outer fiber is zero.

2.4.3. Analytical Solution to the Crack Hinge Model

To establish the closed-form solution of Crack Hinge Model, four dimensionless variables are introduced first

$$\mu = \frac{6M}{f_t h^2 t}, \rho = \frac{N}{f_t h t}, \theta = \frac{hE}{s f_t}\varphi, \alpha = \frac{d}{h}, \tag{5}$$

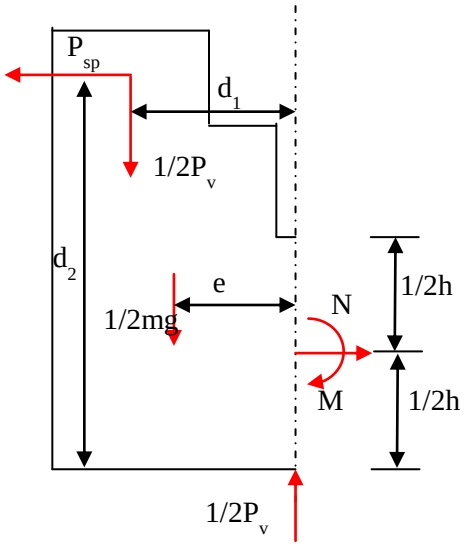

Fig. 8. Free Body Diagram of the Half Hinge Element

where *M* and *N* are shown in Fig. 8; f_t is the tensile strength of the geopolymer; *t* is the width of the hinge; *d* is the depth of the fictitious crack (Figs. 6 and 7); *h* is the total depth of the hinge element.

The wedge used for this test is shown in Fig. 1(c). Assuming the friction constant between the roller and the wedge is η, the equilibrium condition of the wedge gives

$$\eta N \cos\Theta + N \sin\Phi = \frac{P_v}{2}. \tag{6}$$

The equilibrium condition of the roller gives

$$P_{sp} = N\cos\Phi - \eta N\cos\Phi. \tag{7}$$

Thus

$$P_{sp} = \frac{1-\eta\tan\Phi}{2(\eta+\tan\Phi)} P_v. \tag{8}$$

Taking the segment of the specimen as a Euler-Bernoulli beam, thus $\varphi = \frac{Ms}{2EI}$, where $I = \frac{th^3}{12}$, s is the length of the hinge (Fig. 6(b)). Then bending moment M can be expressed as

$$M = \frac{Eth^3\varphi}{6s} = \frac{th^2\theta f_t}{6}. \tag{9}$$

The stress of the outer fiber can be written as

$$\sigma_m = \frac{6M}{h^2t} + \frac{N}{ht} = \theta f_t + \rho f_t. \tag{10}$$

If $\sigma_m \leq f_t$, there is no crack; and $\alpha = 0$ and $\theta \leq 1 - \rho$.

The displacement of the horizontal strip $u(y)$ shown in Fig. 6(b) can be obtained as the sum of the elastic deformation of the strip and the crack opening as

$$u(y) = s\frac{\sigma(w(y))}{E} + w(y) = 2(y - y_0)\varphi\ , \tag{11}$$

where $w(y)$ is the crack opening. Rearranging Eq. (11) yields

$$\sigma\big(w(y)\big) = \frac{E}{s}[2(y - y_0)\varphi - w(y)]\ . \tag{12}$$

Considering the constitution law of the Crack Hinge Model given by Eqs. (3) and (4), we have

$$\sigma\big(w(y)\big) = f_t(b_i - a_i w(y)). \tag{13}$$

Substituting Eq. (13) into Eq. (12) and solving for $w(y)$ give

$$w(y) = \frac{f_t b_i - \frac{2(y-y_0)\varphi E}{s}}{f_t a_i - \frac{E}{s}} = \frac{\frac{2(y-y_0)sf_t\theta}{hE} - \zeta_i}{1-\beta_i} \tag{14}$$

where $\beta_i = \frac{f_t a_i s}{E}$, $\zeta_i = \frac{f_t b_i s}{E}$. Substituting Eq. (14) into the constitution equation Eq. (3) yields

$$\sigma\big(w(y)\big) = f_t\left[b_i - a_i\frac{2(y-y_0)\varphi-\zeta_i}{1-\beta_i}\right] = f_t\left[b_i - a_i\frac{\frac{2(y-y_0)sf_t\theta}{hE}-\zeta_i}{1-\beta_i}\right]. \tag{15}$$

At the end of phase I, we have

$$\theta + \rho = 1. \tag{16}$$

Namely,

$$\theta + \frac{N}{thf_t} = 1\ . \tag{17}$$

Considering $M = \frac{th^2\theta f_t}{6}$, Eq. (17) can be written as

$$\frac{6M}{th^2 f_t} + \frac{N}{thf_t} = 1\ . \tag{18}$$

From the free body diagram of the specimen shown in Fig. 8, we have

$$N = P_{sp},\ \ M = P_{sp}\left(d_2 - \frac{h}{2}\right) + \frac{P_v d_1}{2} + \frac{mge}{2}, \tag{19}$$

where *mg* is the self-weight of the specimen; d_1, d_2, and *e* are shown in Fig. 8. Substituting Eq. (19) into Eq. (18) yields

$$\frac{6}{th^2 f_t}\left[P_{sp}\left(d_2 - \frac{h}{2}\right) + \frac{P_v d_1}{2} + \frac{mge}{2}\right] + \frac{P_{sp}}{thf_t} = 1. \tag{20}$$

Rearranging Eq. (8), we have

$$P_v = kP_{sp}, \tag{21}$$

where $k = \frac{2(\eta+\tan\Phi)}{1-\eta\tan\Phi}$. Substituting Eq. (21) into Eq. (19) and solving for P_{sp}, we have

$$P_{sp} = \frac{f_t h^2 t - 3mge}{6d_2 + 3kd_1 - 2h} \tag{22}$$

The beam forces can also be calculated by

$$M = \int_0^h \sigma(y)(y-y_0)dy = Et\int_0^{h-d}\frac{2(y-y_0)\varphi}{s}(y-y_0)dy$$

$$+t\int_{h-d}^{h} f_t\left[b_i - a_i\frac{2(y-y_0)\varphi-\zeta_i}{1-\beta_i}\right](y-y_0)dy$$

$$=\frac{h^2 f_t(-3+3(2-4\alpha+\alpha^2)\theta+4(-1+\alpha)^3\theta^2+(3+6(-1+2\alpha)\theta+4(1-3\alpha+3\alpha^2)\theta^2)\beta_1)}{6\theta(-1+\beta_1)}, \tag{23}$$

$$N=\int_0^h \sigma(y)dy = Et\int_0^{h-d}\frac{2(y-y_0)\varphi}{s}dy + t\int_{h-d}^{h} f_t\left[b_i - a_i\frac{2(y-y_0)\varphi-\zeta_i}{1-\beta_i}\right]dy =$$

$$\frac{thf_t(-1+(-1+\alpha)^2\theta+(1+(-1+2\alpha)\theta)\beta_1)}{-1+\beta_1}. \tag{24}$$

Solving for α gives

$$\alpha = 1-\beta_1-\sqrt{(1-\beta_1)\left(\frac{1-\rho}{\theta}-\beta_1\right)}. \tag{25}$$

The other root of α has no physical significance since α has to satisfy $0 \le \alpha < 1$. Then

$$\mu = 4\left(1-3\alpha+3\alpha^2-\frac{\alpha^3}{1-\beta_1}\right)\theta+(6\alpha-3)(1-\rho). \tag{26}$$

The crack mouth opening displacement (CMOD) and the COD are obtained as

$$CMOD = w(h) = \frac{sf_t}{E}\frac{2\alpha\theta}{1-\beta_1}, \tag{27}$$

$$COD = w(y) = \frac{sf_t}{E}\frac{2\left(\alpha-1+\frac{y}{h}\right)\theta+(1-b_i)}{1-\beta_i}, \tag{28}$$

where $(b_i,\beta_i) = f(x) = \begin{cases}(1,\beta_1), \text{phase} I\\ (b_2,\beta_2), \text{phase } II\\ (0,0), \text{ phase } III\end{cases}$.

The solutions for other phases could also be obtained in a similar way and are given by Olesen (Olesen, 2001) as following.

Phase II:

$$\alpha_{II} = 1-\beta_2-\frac{1-b_2}{2\theta}-\sqrt{(1-\beta_2)\left(\frac{(1-b_2)^2}{4\theta^2(\beta_1-\beta_2)}-\beta_2+\frac{b_2-\rho}{\theta}\right)}, \tag{29}$$

$$\mu_{II} = 4\left(1-3\alpha+3\alpha^2-\frac{\alpha^3}{1-\beta_2}\right)\theta+(6\alpha-3)(1-\rho)-\frac{(1-b_2)\left(3\alpha^2-\left(\frac{c}{2\theta}\right)^2\right)}{1-\beta_2}, \tag{30}$$

Phase III:

$$\alpha_{III} = 1 - \frac{1}{2\theta}\left(1 + \sqrt{\frac{(1-b_2)^2}{\beta_1 - \beta_2} + b_2^2 - 4\rho\theta}\right), \tag{31}$$

$$\mu_{III} = 4\theta * (1 - 3\alpha + 3\alpha^2 - \alpha^3) + (6\alpha - 3)(1 - \rho) - 3\alpha^2 + \frac{\left(1-\frac{b_2}{\beta_2}\right)(1-b_2+c)}{4\theta^2\beta_2}\left(1 + \frac{\beta_1 c}{1-\beta_1}\right) + \frac{c}{2\theta}^2, \tag{32}$$

where $c = (1-b_2)(1-\beta_1)/(\beta_2-\beta_1)$.

2.4.4. Inverse Analysis

Equations obtained in the above section suggest that the COD can be easily obtained if ρ is known. However, there is no explicit expression to obtain ρ from the COD. Therefore, an inverse analysis is employed to obtain the traction-separation law of the FPZ from the global response of the specimen (the load-COD curve) using the algorithm proposed by Østergaard (Østergaard, 2004). Since a DIC system was used to measure the full-field displacement of the specimen, multiple CODs can be obtained. To take these CODs into inverse analysis, the Østergaard (Østergaard, 2004)'s algorithm was extended, which may provide more reliable results of the traction separation law.

By using one COD, the algorithm to retrieve the traction-separation law of the geopolymer specimens can be carried out as following:

Find Young's modules *E*: The Young's modulus is obtained by least-square fitting the P-COD curve in the phase I (elastic stage) as shown in Appendix C. The elastic solution is obtained from Finite Element Analysis (FEA) (The batch file used for this analysis is in Appendix B).

Iteratively find f_t, a_1, b_1, a_2, b_2 by least-square fitting *P*-curve in phase II and III:

$$\min \frac{1}{N}\sum_1^N \left(P_{sp}^{cal} - P_{sp}^{obs}\right)^2 \tag{33}$$

where P_{sp}^{cal} is the calculated horizontal force given by Eq. (20).

If multiple CODs are needed, Eq. (33) can be extended as

$$\min \frac{1}{J}\sum_1^J \frac{1}{N}\sum_1^N \left(P_{sp}^{cal} - P_{sp}^{obs}\right)^2 \tag{34}$$

where *J* is the number of the CODs obtained at different locations.

3. TESTING RESULTS AND DISCUSSIONS

An MTS machine was used to load the specimen under displacement control at the rate of 0.0003 in/min. 10 cycles of "loading to 20 lbs and then unloading" process were applied to the specimen before the testing to create a sharp crack tip. The DIC system took a picture every 20 seconds. To reduce the air vibration caused by temperature fluctuation, two florescent lamps were used to provide strong light for the DIC system, instead of the stock incandescent lamps that heated up the air and the specimen. Unlike in the traditional testing method where only COD can be measured, the full-field measurement using the DIC system allows for measuring COD at any location along the crack path. As shown in Fig.9. Three CODs measured at different depths (y = 20, 25, and 30mm as shown in Fig. 9) were used in the inverse analysis. The calculated results are shown in Table 3 and Fig.10. It can be seen that a slightly different traction-separation law is obtained by using different CODs.

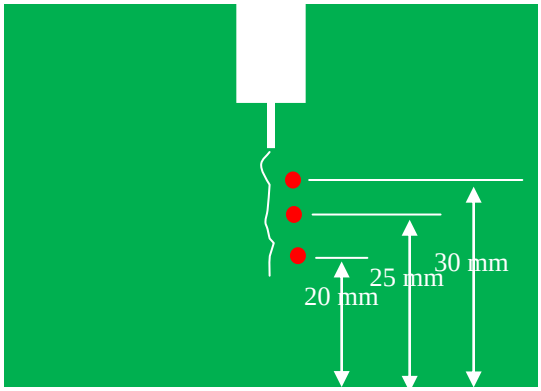

Fig. 9. Location of Measured CODs Used in Inverse Analysis

Table 3. Traction-Separation Parameters Retrieved Using One Load COD Curve

Location of COD measured (mm)	**20**	**25**	**30**
f_t **(Pa)**	4.09E+06	3.90E+06	3.91E+06
a_1	74043	59772	48322
a_2	827.83	328.17	316.09
b_2 **(mm)**	0.065701	0.0392	0.041614
w_1 **(m)**	1.28E-05	1.62E-05	2E-05
w_2 **(m)**	7.94E-05	0.000119	0.000132

With the known traction separation law, the load verse COD curve can be calculated (Matlab function is in wst_forward.m in Appendix C). Figure 11 and 12 compare the simulated load-COD curves with the experimental ones. It can be seen that simulated curves reach excellent agreement with the measured one, suggesting that the bi-linear traction-separation law can give good prediction of the fracture behavior of the geopolymer mortar.

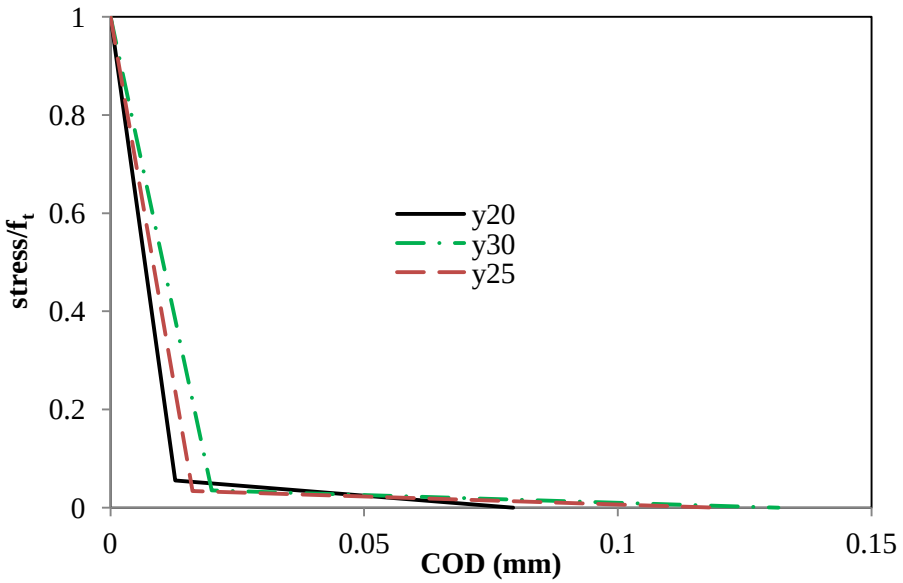

Fig. 10. Traction Separation Law Obtained Using One Load COD Curve

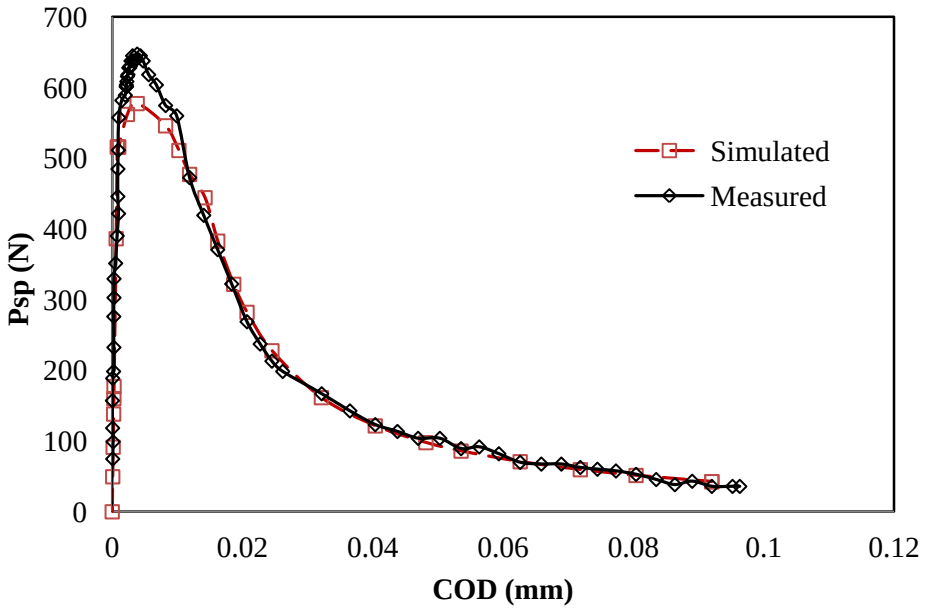

Fig. 11. Comparison of Simulated and Measured Load-COD Curve Using COD at y = 25 mm.

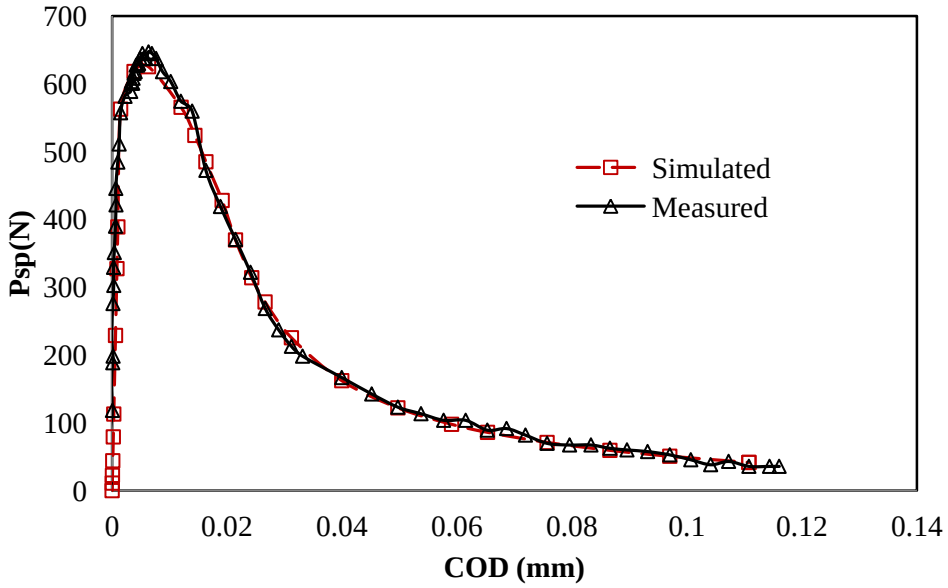

Fig. 12. Comparison of Simulated and Measured Load-COD Curve Using COD at y = 30 mm.

The fracture energies which are the areas below the traction-separation laws were calculated based on these different CODs and are shown in Fig. 13. It can be seen that the fracture energy of this geopolymer mortar is in the same order of magnitude as that of the OPC based concrete, but has lower value compared with OPC concrete with similar compressive strength. This may suggest that the geopolymer mortar is more brittle than the OPC-based mortar.

Figure 13 clearly shows that the fracture energy depends on the location of the measured COD. It reduces with the distance of the location of COD to the back boundary of the specimen. This interesting feature is caused by the size effect of the crack propagation in quasi-brittle material such as geopolymer mortar. As shown in Fig. 9, the location of the COD actually gives the ligament between the crack tip to the back boundary of the specimen.

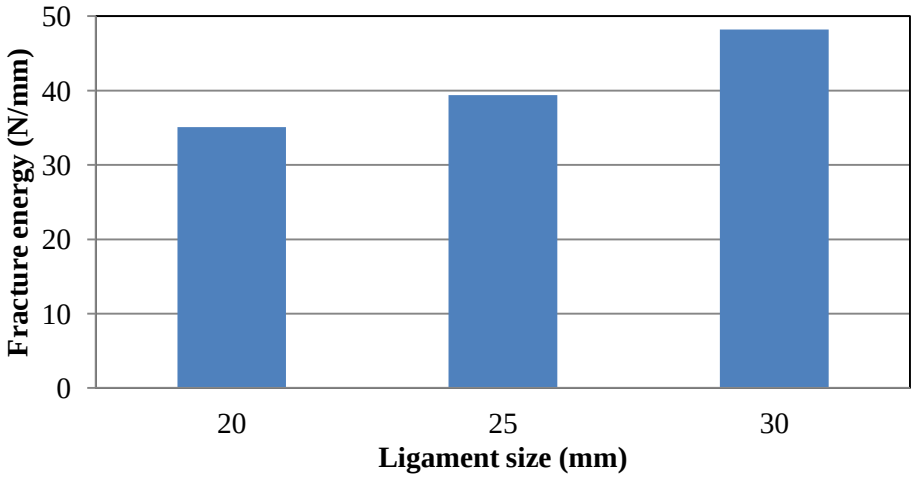

Fig. 13. Fracture Energy Reduces with the Ligament Size

Size effect is a common feature in quasi-brittle materials. Size effect of the fracture energy of concrete has been linked to the influence of ligament length on the FPZ. Small FPZ associated with smaller ligament length leads to lower specific fracture energy. This was explained by Hu and Duan (Hu and Duan, 2004) by considering the development of the FPZ. For a sufficient large ligament between the crack tip and the back boundary of the specimen, there exist an inner zone and a boundary zone, as shown in Fig. 14. The crack-tip FPZ during crack growth can be fully developed in the inner zone as it is away from the specimen's back boundary. In this zone, the FPZ's height h_{FPZ} remains constant at its maximum (Fig. 14(b)) and fracture energy is constant. In the boundary region, FPZ, and then its height h_{FPZ} is inevitably reduced because of the physical limitation of the remaining ligament and the ever-changing stress gradient. The variation in h_{FPZ} leads to the reduction in the local specific fracture energy g_f. As shown in Fig. 9, the ligament between the location where COD is measured and the boundary may be not big enough such that all three fracture energies were measured within the boundary zone, leading to their dependence on the location of the COD. If this is true, it suggests that size effect of a quasi-

brittle material can be studied by just using one-size specimen, which can save enormous time and energy compared with the commonly used method, in which specimens with different sizes must be manufactured and tested.

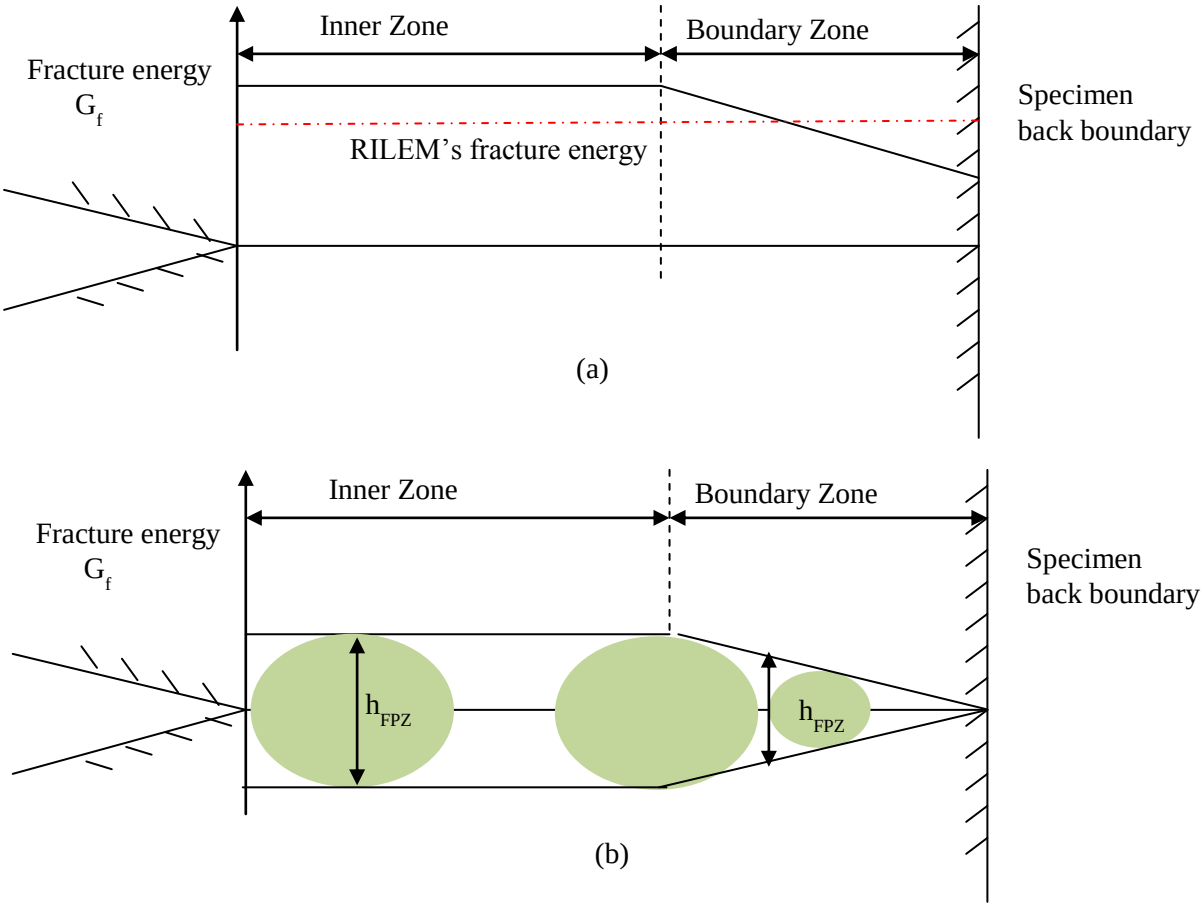

Fig. 14. Effect of Ligament Size on Fracture Energy: (a) Fracture Energy Varies in Different Zones; (b) Corresponding Variations of FPZ and Its Height in Different Zones (Hu and Duan 2004)

We can also use all three CODs to back calculate an averaged traction-separation law using Eq. (34). The resulted average bi-linear traction-separation law is shown in Fig. 3.15 and parameters are given as: $f_t = 4.02$ MPa, $a_1 = 63265$, $a_2 = 828.62$, $b_2 = 0.065787$, $w_1 = 1.49626 \times 10^{-5}$, $w_2 = 7.93934 \times 10^{-5}$, and fracture energy is 38.6 N/m. Figures 16 and 17 compare the simulated load-COD curves with the experimental

ones. Once again, excellent agreement with the measured data has been achieved by the simulation, suggesting that the average traction-separation law retrieved using multiple CODs also works very well for the examined geopolymer mortar.

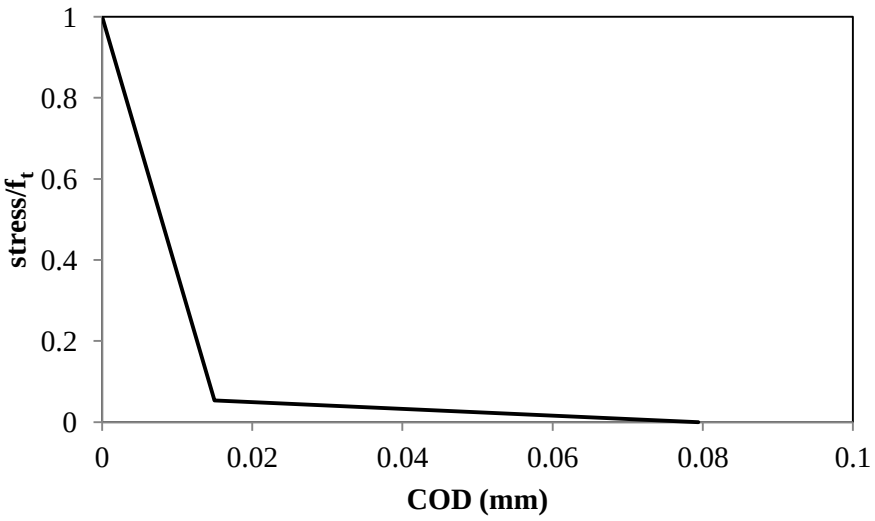

Fig. 15. Average Traction-Separation Law Calculated Based on Three CODs.

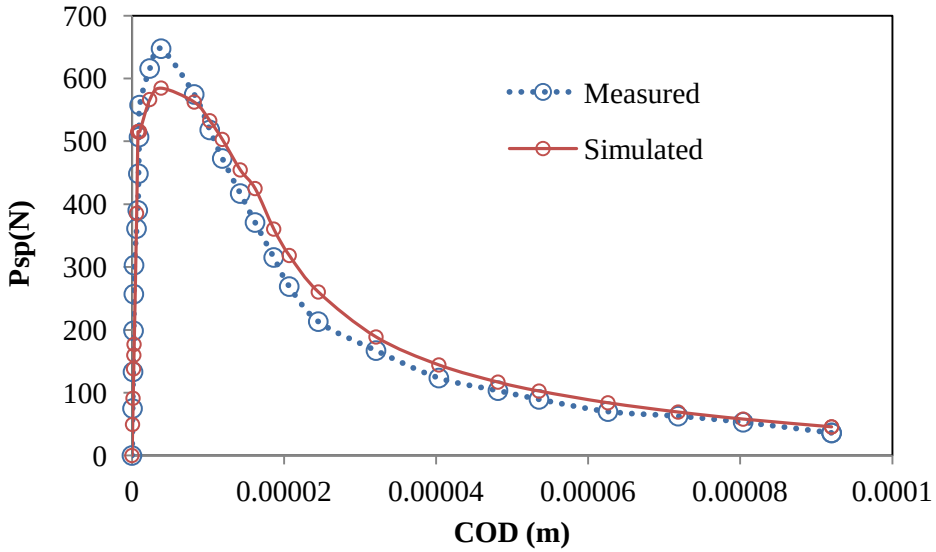

Fig. 16. Comparison of Simulated and Measured Load verse COD (y = 25 mm) Curve Using the Averaged Traction-Separation Law.

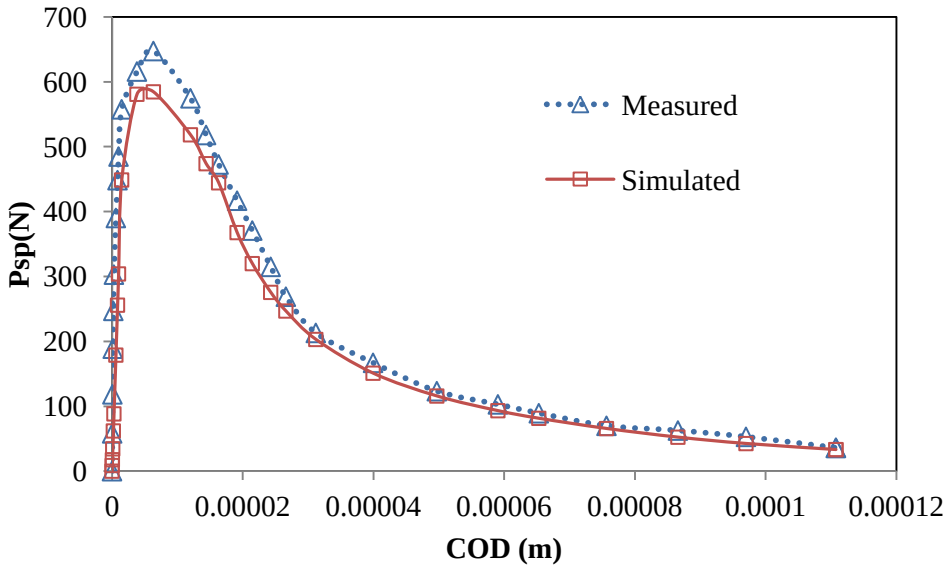

Fig. 17. Comparison of Simulated and Measured Load verse COD (y = 30 mm) Curve Using the Averaged Traction-Separation Law.

4. CONCLUSIONS

This study examines the nonlinear fracture behavior of a fly ash based geopolymer mortar using splitting wedge testing method. A full-field displacement measurement technology, DIC system is used to measure the full-field displacement of the fracture specimen and to determine the CODs. Following conclusions can be drawn from this study:

1. The full-field displacement measurement clearly shows that a FPZ exists ahead of the major crack, suggesting that the fracture of the geopolymer mortar follows a nonlinear behavior similar to the OPC based concrete.
2. The bi-linear law of the FPZ of the geopolymer can be retrieved by least-square fitting the analytical solution and the testing data.
3. The geopolymer mortar has lower fracture energy compared with OPC-based concrete with similar strength.

4. By using the DIC system to measure CODs at different locations, testing one fracture specimen is equivalent to testing multiple specimens with different crack sizes. Therefore, only one specimen is needed in this study to study the size effect of the fracture of quasi-brittle materials, which can save enormous efforts compared with traditional methods used in size-effect study.
5. The fracture energy of the geopolymer mortar exhibits clear size-dependent feature, which in turn confirms that the fracture of geopolymer mortar is nonlinear.

REFERENCES

Barenblatt, G. I. 1959. "The formation of equilibrium cracks during brittle fracture. General ideas and hypotheses. Axially-symmetric cracks." *Journal of Applied Mathematics and Mechanics* 23 (3): 622–636.

Bažant, Zdeněk P. 2000. "Size effect." *International Journal of Solids and Structures* 37 (1–2) (January): 69–80.

Brühwiler, E., and F.H. Wittmann. 1990. "The wedge splitting test, a new method of performing stable fracture mechanics tests." *Engineering Fracture Mechanics* 35 (1-3): 117–125.

Cho, K., et al. 1984. "Fracture Process Zone of Concrete Cracks." *Journal of Engineering Mechanics* 110 (8): 1174–1184.

Chu, T. C., et al. 1985. "Applications of digital-image-correlation techniques to experimental mechanics." *Experimental Mechanics* 25 (3) (September 1): 232–244.

Denarié, E., et al. 2001. "Concrete Fracture Process Zone Characterization with Fiber Optics." *Journal of Engineering Mechanics* 127 (5) (May 1): 494.

Gopalaratnam, V. S., and Surendra P. Shah. 1985. "Softening response of plain concrete in direct tension." In *ACI Journal Proceedings*. Vol. 82. ACI.

Hillerborg, A., et al. 1976. "Analysis of crack formation and crack growth in concrete by means of fracture mechanics and finite elements." *Cement and Concrete Research* 6 (6) (November): 773–781.

Hu, X., and K. Duan. 2004. “Influence of fracture process zone height on fracture energy of concrete.” *Cement and Concrete Research* 34 (8) (August): 1321–1330.

Linsbauer, HN, and EK Tschegg. 1986. “Fracture energy determination of concrete with cube shaped specimens.” *Zement und Beton* 31: 38–40.

Olesen, J. 2001. “Fictitious Crack Propagation in Fiber-Reinforced Concrete Beams.” *Journal of Engineering Mechanics* 127 (3): 272–280.

Østergaard, L. 2004. “Early-age fracture mechanics and cracking of concrete. Experiments and modelling.” Danmarks Tekniske University.

Pan, Zhu, Jay G. Sanjayan, and B. Vijay Rangan. 2011. “Fracture Properties of Geopolymer Paste and Concrete.” *Magazine of Concrete Research* 63 (10): 763–71.

Peters, W. H., and W. F. Ranson. 1982. “Digital Imaging Techniques In Experimental Stress Analysis.” *Optical Engineering* 21 (3): 213427.

RILEM TC-50 FMC, ‘Determination of the fracture energy of mortar and concrete by means of three-point bend tests on notched beans’, *Mater. Struct.*, **18** (1985) 287–290

Roelfstra, P. E., and F. H. Wittmann. 1986. “Numerical method to link strain softening with failure of concrete.” *Fracture toughness and fracture energy of concrete*: 163–175.

Sarker, P. K. et al. 2013. “Fracture behaviour of heat cured fly ash based geopolymer concrete.” *Materials & Design* 44 (February): 580–586.

Skoček, J., and H. Stang. 2008. “Inverse analysis of the wedge-splitting test.” *Engineering Fracture Mechanics* 75 (10) (July): 3173–3188.

Skoček, J., and H. Stang. 2010. “Application of optical deformation analysis system on wedge splitting test and its inverse analysis.” *Materials and Structures* 43 (April 13): 63–72.

Sutton, MA, WJ Wolters, WH Peters, WF Ranson, and SR McNeill. 1983. “Determination of displacements using an improved digital correlation method.” *Image and Vision Computing* 1 (3) (August): 133–139.

Ulfkjær, J., et al. 1995. “Analytical Model for Fictitious Crack Propagation in Concrete Beams.” *Journal of Engineering Mechanics* 121 (1): 7–15.

Wittmann, Folker H. 1986. “Fracture Toughness and Fracture Energy of Concrete.” In *Proceedings of the International Conference on Fracture Mechanics of Concrete*. Lausanne, Oct. 1985

Appendix A

The python 2.7 script that extracts Crack width and Load:

```
#extract COD-Force curve from DIC images and MTS load
  file

import argparse
import os
import re
import stat
import time
from datetime import datetime

def parse_mts(fp):
        "parse the MTS data file, returns a list of [time,
  load, disp]"
        ret = []
        with open(fp, 'r') as f:
                sline = re.compile('^"EXTENSION')
                blank = re.compile('^\s*$')
                begin = False
                for i in f.readlines():
                        #print i
                        if sline.match(i):
                                begin = True
                                #print "begin"
                                continue
                        if not begin:
                                continue
                        if blank.search(i):
                                continue
                        #data lines
                        ret.append(map(float,
  i.split(','))) #extension (in), time (min), load(lbs)
        return ret

def image_time(fp, st):
        #the timestamp of the @fp relative to @st
```

```
        delta =
  datetime.fromtimestamp(os.stat(fp)[stat.ST_MTIME]) - st
        return delta.total_seconds()

def COD(fp, x, y):
        #the COD of @image, measured at y = @y, x = @x
        #@fp is the DIC exported data file
        COL_X = 0
        COL_Y = 1
        COL_U = 6
        dist1 = dist2 = 10000000
        point1 = point2 = None
        blank = re.compile('^\s*$')
        with open(fp, 'r') as f:
                for i in f.readlines()[1:]:
                        if blank.search(i):
                                continue
                        c = map(float, i.split(","))
                        c1 = (c[COL_X] - x) ** 2 +
  (c[COL_Y] - y) ** 2
                        c2 = (c[COL_X] + x) ** 2 +
  (c[COL_Y] - y) ** 2
                        if c1 < dist1:
                                dist1 = c1
                                point1 = (c[COL_X],
  c[COL_Y], c[COL_U])
                        if c2 < dist2:
                                dist2 = c2
                                point2 = (c[COL_X],
  c[COL_Y], c[COL_U])
        #print point1, point2
        if point1 == None or point2 == None:
                return None
        return point1[2] - point2[2]

def force(mts, t):
        #@mts: returned from parse_mts
        #t: time in seconds
        f0 = 0
```

```
        d = 10000
        for ext, ti, f in mts:
                tm = ti * 60 #convert to seconds
                if tm > t:
                        d1 = tm - t
                        if d1 < d:
                                print "force = ", f
                                return f
                        break
                d = t - tm
                f0 = f
        print "force = ", f0
        return f0

def main():
        parser =
  argparse.ArgumentParser(description='Handle the command
  options')
        parser.add_argument('--DIC-dir', metavar='PATH',
  action='store', default=os.path.dirname(__file__),
  dest='dic_dir', help="DIC image directory")
        parser.add_argument('--DIC-prefix',
  metavar='prefix', action='store', default='test',
  dest='dic_prefix', help="DIC image file prefix (default:
  test)")
        parser.add_argument('--MTS-data', action='store',
  dest='mts_data', help="Data file exported from MTS")
        parser.add_argument('--start-time',
  action='store', dest='start_time', help="What time did
  the test start? (in MM/DD/YYYY HH:MM:SS format)")
        parser.add_argument('--start-seq',  action='store',
  dest='start_seq', type=int, default=0, help="what seq
  number the images start?")
        parser.add_argument('--stop-seq', action='store',
  dest='stop_seq', type=int, help="What seq number the
  images end?")
        parser.add_argument('--y', action='store',
  dest='y', type=float, help="The y coordinate at which
  the COD is measured")
```

```
	parser.add_argument('--x', action='store',
dest='x', type=float, help="The x coordinate at which
the COD is measured")
	parser.add_argument('--dest', action='store',
dest='dest', help="The file to store the result")

	args = parser.parse_args()
	#print args
	#print args.dic_prefix
	#print args.mts_data

	mts = parse_mts(args.mts_data)
	st = datetime.strptime(args.start_time,
"%m/%d/%Y %H:%M:%S")
	with open(args.dest, 'w') as dest:
		curve = []
		for i in xrange(int(args.start_seq),
int(args.stop_seq) + 1):
			t =
image_time(os.path.join(args.dic_dir, args.dic_prefix +
'-%04d_0.tif' % i), st)
			print "Processing data point", i,
"t = ", t / 60
			cod =
COD(os.path.join(args.dic_dir, args.dic_prefix + '-
%04d_0.csv' %i), args.x, args.y)
			if cod != None:
				curve.append((cod,

force(mts, t) * 4.44822162 #convert to newtons
                                                        ))
		#curve.sort(cmp = lambda x, y: int(x[0])
- int(y[0]))
		dest.write("File No,COD(mm),Force(N)\n")
		for i, (ext, f) in enumerate(curve):
			dest.write("%d,%g,%g\n" % (i, ext,
f))
```

```
if __name__ == '__main__':
        main()
```

Appendix B

Ansys batch file for elastic analysis:

```
!/clear
  !/UNITS, MPA
  !LEN -- millimeters
  !MASS -- Tonne
  !FORCE -- Newton
  !
  !/UNITS, uMKS
  !LEN -- micro-meter
  !MASS -- Kg
  !FORCE -- micro-Newton
  !Pressure -- MPa
  !
  !/UNITS, MKS
  /PREP7

  !english system
  x1 = 1.0/16
  x2 = 1
  x3 = 3
  y1 = 1.5
  y2 = y1 + 5.0/8
  y3 = y2 + 5.0/8

  !convert to metric system
  x1 = x1*0.0254
  x2 = x2*0.0254
  x3 = x3*0.0254
  y1 = y1*0.0254
  y2 = y2*0.0254
  y3 = y3*0.0254

  EP=1E9 !Young's modulus of high strength concrete,
  set by command line
  NUP=.3

  /PNUM,KP,0
```

```
/PNUM,LINE,0
/PNUM,AREA,0
/PNUM,VOLU,1
/PNUM,NODE,0
/PNUM,TABN,0
/PNUM,SVAL,0
/NUMBER,1
/PNUM,MAT,1

ET,1, PLANE182
KEYOPT, 1, 1, 2 !reduced integration as per ANSYS
sugguests

MPTEMP,1,0
MPDATA, EX, 1, , EP
MPDATA, PRXY, 1, ,NUP

K, 1, 0, 0, 0
K, 2, x1, 0, 0
K, 3, x2, 0, 0
K, 4, x3, 0, 0
K, 11, 0, y1, 0
K, 12, x1, y1, 0
K, 13, x2, y1, 0
K, 14, x3, y1, 0
K, 22, x1, y2, 0
K, 23, x2, y2, 0
K, 24, x3, y2, 0
K, 33, x2, y3, 0
K, 34, x3, y3, 0

A, 1, 2, 12, 11
A, 2, 3, 13, 12
A, 3, 4, 14, 13
A, 12, 13, 23, 22
A, 13, 14, 24, 23
A, 23, 24, 34, 33

KSEL,ALL
```

```
NUMMRG, KP

ASEL, ALL
AATT, 1,,,  !AATT, MAT, REAL, TYPE, ESYS, SECN

LSEL,ALL
LESIZE, ALL, 0.0254/32

FINE=0.01
MSHKEY, 1
MSHAPE, 0, 2D
ESIZE, FINE, 20
AMESH,ALL

NUMMRG, ALL
FINISH

/SOLU
PV=50 !in newtons
fmu=0.02 !friction coefficient
theta=15*3.1415926/180 !wedge angle
PH=PV*(1-fmu*tan(theta))/(2*(fmu+tan(theta)))

ANTYPE, STATIC

SELTOL, 2E-12
NSEL, S, LOC, x, 0
DSYM, SYMM, X

!bottom
NSEL, R, LOC, Y, 0
D, ALL, UY, 0

NSEL, S, LOC, X, X2,
NSEL, R, LOC, Y, Y2, Y3
*GET, COUNT, NODE, 0, COUNT
F, ALL, FX, PH/COUNT

NSEL, S, LOC, X, X2-0.75*0.0254, X2
```

```
NSEL, R, LOC, Y, Y2
*GET, COUNT, NODE, 0, COUNT
F, ALL, FY, -0.5*PV/COUNT

ALLSEL
SOLVE
FINISH

/POST1
XCOOR = 0.010
YCOOR = 0.030
SELTOL, 5E-4
NSEL, S, LOC, X, XCOOR
NSEL, R, LOC, Y, YCOOR
*GET, P1, NODE, 0, NUM, MIN
*GET, XCOOR, NODE, P1, LOC, X
*GET, YCOOR, NODE, P1, LOC, Y
DIS=2*UX(P1)
eC=PV/EP/DIS
FINISH
```

Appendix C.

Matlab files for inverse analysis (Based on Østergaard's code (Østergaard, 2004):

wst.m:

```
function
  out=wst(estimates,output,geometry,step,min_load,actout,
  actplot)
if nargin <=6
    actplot = 1;
    if nargin <= 5;
        actout = 0;
        if nargin <= 4
            min_load = 1;
            if nargin <= 3
                step = 0.1;
                if nargin <= 2
                    geometry = 'wstgeometry.dat';
                    if nargin == 1
                        output = 'wst.out';
                    end,end,end,end,end,end
est=textread(estimates, 'commentstyle', '%');
geo=textread(geometry, 'commentstyle', '%');
m = geo(1); a0 = geo(2); am = geo(3); b = geo(4); bm =
  geo(5); d1 = geo(6);
d2 = geo(7); h = geo(8); L1 = geo(9); t = geo(10); mu =
  geo(11); L2=geo(12);
alpha_w = geo(12);
s=stimate(est,geo,'wst');
g = 9.82;
ft=est(1); a1=est(2); a2=est(3); b2=est(4); E=est(5);
m = m/2;
alpha_w = alpha_w/180*pi;
beta1 = ft*a1*s/E; beta2 = ft*a2*s/E;
A_1 = bm*(L1-h-a0); A_2 = (L2/2-am/2)*a0; A_3 = L2/2*h;
A = A_1 + A_2 + A_3;
e = (L2/2-bm/2)*A_1/A + (L2/4+am/2)*A_2/A + L2/4*A_3/A;
if size(geo,1)==12
```

```
    y = (b-h)/b;
    v2 = y/(1-y)^2*(38.2-55.4*y+33.0*y^2);
else
    v2 = geo(13);
end
kmu = (2*tan(alpha_w)+2*mu)/(1-mu*tan(alpha_w));
c = (1-b2)*(1-beta1)/(beta2-beta1);
p_0 = (ft*h^2*t-6*m*g*e)/(6*d2+3*d1*kmu-2*h);
theta_0_1 = 1 - 1/(ft*h*t)*p_0;
cmod_0 = p_0/E/t*v2;
row = 3;
res = [0 0 0 0 0;... %cmod P alpha theta phase
    cmod_0 p_0 0 1 0];
options =
  optimset('Display','off','MaxFunEvals',5000,'MaxIter',5
  000,...
    'TolFun',1e-13);
while res(row-1,2) >= min_load
    res(row,4) = res(row-1,4)+step*res(row-1,4);
    res(row,2) = fsolve(@fun,res(row-
  1,2),options,ft,h,t,c,beta1,beta2,...
        b2,d2,kmu,d1,m,g,e,s,E,b,res(row,4));
    [res(row,1), res(row,3), res(row,5)] =
  params(res(row,2),ft,h,t,c,...

  beta1,beta2,b2,d2,kmu,d1,m,g,e,s,E,b,theta_0_1,v2,res(r
  ow,4));
    row = row + 1;
end
if actout == 1
    out = res;
end
if actplot == 1
    hold off
    plot(res(:,1),res(:,2),'-o','MarkerSize',6);
    hold on
    title(['P-CMOD curve based on "' estimates
  '"'],'FontSize',12,...
        'interpreter','none')
```

```
    xlabel('CMOD','FontSize',14)
    ylabel('P ','Rotation',0,'FontSize',14)
    axis([0 1.1*max(res(:,1)) 0 1.1*max(res(:,2))])
end
dlmwrite(output,res,'\t')
function F =
  fun(x,ft,h,t,c,beta1,beta2,b2,d2,kmu,d1,m,g,e,s,E,b,the
  ta)
rho = 1/(ft*h*t)*x;
theta_1_2 = 1/2*(1-rho-c+sqrt((1-rho-c)^2+c^2/(beta1-1)));
theta_2_3 = 1/2*(rho*(beta2-
  1)+b2/beta2+sqrt(rho^2*(beta2-1)^2+2*rho...
    *(beta2-1)*b2/beta2+(1-b2)^2/(beta1-
  beta2)+b2^2/beta2));
switch 1
    case theta <= theta_1_2
        alpha = 1-beta1-sqrt((1-beta1)*((1-rho)/theta-
  beta1));
        mu = 4*(1-3*alpha+3*alpha^2-alpha^3/(1-
  beta1))*theta+(6*alpha-3)*(1-rho);
    case theta <= theta_2_3
        alpha = 1-beta2-(1-b2)/2/theta-sqrt((1-
  beta2)*((1-b2)^2/4/theta^2/...
            (beta1-beta2)-beta2+(b2-rho)/theta));
        mu = 4*(1-3*alpha+3*alpha^2-alpha^3/(1-
  beta2))*theta+(6*alpha-3)...
            *(1-rho)-(1-b2)*(3*alpha^2-(c/2/theta)^2)/(1-
  beta2);
    case theta > theta_2_3
        alpha = 1-1/2/theta*(1+sqrt((1-b2)^2/(beta1-
  beta2)+b2^2/beta2-...
            4*rho*theta));
        mu = 4*theta*(1-3*alpha+3*alpha^2-
  alpha^3)+(6*alpha-3)*(1-rho)-...
            3*alpha^2+1/4/theta^2*(1-b2/beta2)*(1-
  b2/beta2+c)*(1+beta1...
            *c/(1-beta1))+(c/2/theta)^2;
end
F = mu-6/(ft*h^2*t)*(x*(d2-h/2)+1/2*kmu*x*d1+m*g*e);
```

```
function [cmod, alpha, phase] =
  params(x,ft,h,t,c,beta1,beta2,b2,...
    d2,kmu,d1,m,g,e,s,E,b,theta_0_1,v2,theta)
rho = 1/(ft*h*t)*x;
theta_1_2 = 1/2*(1-rho-c+sqrt((1-rho-c)^2+c^2/(beta1-1)));
theta_2_3 = 1/2*(rho*(beta2-
  1)+b2/beta2+sqrt(rho^2*(beta2-1)^2+2*...
    rho*(beta2-1)*b2/beta2+(1-b2)^2/(beta1-
  beta2)+b2^2/beta2));
switch 1
    case theta <= theta_1_2
        alpha = 1-beta1-sqrt((1-beta1)*((1-rho)/theta-
  beta1));
        bi = 1; betai=beta1;
        phase = 1;
    case theta <= theta_2_3
        alpha = 1-beta2-(1-b2)/2/theta-sqrt((1-
  beta2)*((1-b2)^2/4/...
            theta^2/(beta1-beta2)-beta2+(b2-rho)/theta));
        bi = b2; betai=beta2;
        phase = 2;
    case theta > theta_2_3
        alpha = 1-1/2/theta*(1+sqrt((1-b2)^2/(beta1-
  beta2)+b2^2/...
            beta2-4*rho*theta));
        bi = 0; betai=0;
        phase = 3;
end
cmod = s*ft/E*(1-bi+2*alpha*theta)/(1-betai)+2*(b-
  h)*((s*ft/...
    E*(1-bi+2*alpha*theta)/(1-betai))/2/alpha/h-
  s*ft/h/E*theta_0_1/...
    (1-beta1))+x/E/t*v2;
```

datared.m:

```
function [X,Y] = datared(X_full,Y_full,cs_s)
j=1;
row=2;
X = 0;
Y = 0;
peak=find(Y_full==max(Y_full));
m=peak(1);
max_Y=max(Y_full(:,1));
max_X=max(X_full(:,1));
X_full_int=X_full(:)./max_X;
Y_full_int=Y_full(:)./max_Y;
for i=2:m
    if (Y_full_int(i)>Y_full_int(j)) &&
   ((X_full_int(i)>X_full_int(j)))
        X(row,1)=X_full(i);
        Y(row,1)=Y_full(i);
        row=row+1;
        j=i;
    end
end
for i=m+1:size(Y_full,1)
    if (Y_full_int(i)<Y_full_int(j)) &&
   ((X_full_int(i)>X_full_int(j)))
        X(row,1)=X_full(i);
        Y(row,1)=Y_full(i);
        row=row+1;
        j=i;
    end
end
j=1;
row=2;
X_full = X;
Y_full = Y;
X = 0;
Y = 0;
peak=find(Y_full==max(Y_full));
m=peak(1);
max_Y=max(Y_full(:,1));
```

```
max_X=max(X_full(:,1));
X_full_int=X_full(:)./max_X;
Y_full_int=Y_full(:)./max_Y;
for i=2:m
    if X_full_int(i)>X_full_int(j)
        cs=((Y_full_int(i)-
  Y_full_int(j))^2+(X_full_int(i)...
            -X_full_int(j))^2)^0.5;
        if cs >= cs_s
            if cs <= 1.5*cs_s
                X(row,1)=X_full(i);
                Y(row,1)=Y_full(i);
                row=row+1;
                j=i;
            else
                a=(Y_full_int(i)-
  Y_full_int(j))/(X_full_int(i)-X_full_int(j));
                dx=sign(X_full_int(i)-
  X_full_int(j))*1/(1+a^2)^0.5*cs_s;
                dy=a*dx;
                k=1;
                while cs > 1.5*cs_s
                    X(row,1)=X_full(j)+k*dx*max_X;
                    Y(row,1)=Y_full(j)+k*dy*max_Y;
                    cs=((Y_full_int(i)-
  Y(row,1)/max_Y)^2+...
                            (X_full_int(i)-
  X(row,1)/max_X)^2)^0.5;
                    row=row+1;
                    k=k+1;
                end
                X(row,1)=X_full(i);
                Y(row,1)=Y_full(i);
                row=row+1;
                j=i;
            end
        end
    end
end
```

```
X(row,1)=X_full(m);
Y(row,1)=Y_full(m);
row=row+1;
i=m;
while i<=size(X_full,1)
    if X_full_int(i)>X_full_int(j)
        cs=((Y_full_int(i)-
  Y_full_int(j))^2+(X_full_int(i)...
            -X_full_int(j))^2)^0.5;
        if cs >= cs_s
            if cs < 1.5*cs_s
                X(row,1)=X_full(i);
                Y(row,1)=Y_full(i);
                row=row+1;
                j=i;
            else
                a=(Y_full_int(i)-
  Y_full_int(j))/(X_full_int(i)-X_full_int(j));
                dx=sign(X_full_int(i)-
  X_full_int(j))*1/(1+a^2)^0.5*cs_s;
                dy=a*dx;
                k=1;
                while cs > 1.5*cs_s
                    X(row,1)=X_full(j)+k*dx*max_X;
                    Y(row,1)=Y_full(j)+k*dy*max_Y;
                    cs=((Y_full_int(i)-
  Y(row,1)/max_Y)^2+...
                            (X_full_int(i)-
  X(row,1)/max_X)^2)^0.5;
                    row=row+1;
                    k=k+1;
                end
                X(row,1)=X_full(i);
                Y(row,1)=Y_full(i);
                row=row+1;
                j=i;
            end
        end
        i=i+1;
```

```
    else
        avg_index=find(Y_full(i:size(Y_full(:,1),1))...
            ==max(Y_full(i:size(Y_full(:,1),1))));
        if (i+avg_index <= size(X_full,1)) &
  (Y_full(i)<Y_full(j))
            X(row,1)=X_full(i+avg_index);
            Y(row,1)=Y_full(i+avg_index);
            row=row+1;
            i=i+avg_index;
            j=j+avg_index;
        else
            i=i+1;
        end
    end
end
X(row,1)=X_full(size(X_full,1));
Y(row,1)=Y_full(size(X_full,1));
```

initialize.m:

```
function ini = initialize(geo,work,inputs,eCs,ycoors)
options = optimset('Display','off','MaxFunEvals',5000,...
    'MaxIter',5000,'TolFun',1e-13);

m = geo.m; a0 = geo.a0; am = geo.am; bm = geo.bm;
d1 = geo.d1; d2 = geo.d2; h = geo.h; L1 = geo.L1; t =
  geo.t;
mu = geo.mu; L2=geo.L2; alpha_w = geo.alpha_w/180*pi;
A_1 = bm*(L1-h-a0); A_2 = (L2/2-am/2)*a0; A_3 = L2/2*h;
A = A_1 + A_2 + A_3;
e = (L2/2-bm/2)*A_1/A + (L2/4+am/2)*A_2/A + L2/4*A_3/A;
kmu = (2*tan(alpha_w)+2*mu)/(1-mu*tan(alpha_w));
[fid, msg] = fopen(inputs{1}, 'r');
if fid > 0
        c = textscan(fid, '%f %f %f', fid, 'Delimiter',
  ',', 'HeaderLines', 1);
        fclose(fid);
        X = c{1} * 0.001;
        Y = c{2};
else
        fprintf(1, 'failed to open input file due
  to: %s\n', msg);
end
ini = struct('ft', 0.5*(max(Y)*(6*d2+3*d1*kmu-
  2*h)+6*(m/2)*9.82*e)/h^2/t, ...
             'b2', 0.5, ...
             'E', 2E10, ...
             'a1', 0, ...
             'a2', 0);
a1 = [5000; 10000; 30000; 40000; 50000];
a2 = [500; 800; 1000; 2000; 5000];
a1s = size(a1);
a2s = size(a2);
b=zeros(a1s(1),a2s(1));
work = work/h/t;
E = zeros(size(b));
output = '';
```

```
for i=1:size(a1(:,1))
    for j=1:size(a2(:,1))
        ini.a1 = a1(i);
        ini.a2 = a2(j);
        fprintf(1, 'Trying a1 = %f, a2 = %f', ini.a1,
  ini.a2);
        if ini.a1 <= ini.a2
            E(i,j) = Inf;
            b(i,j) = Inf;
            fprintf(1, ', b2 = Inf\n');
            continue;
        end
                %[b(i,j),fval, exitflag, output] =
  fzero(@fun,0.5,options,ini,work(1,1));
        try
            [b(i,j),fval, exitflag, output] =
  fzero(@fun,0.5,options,ini,work(1,1));
        catch
            E(i,j) = Inf;
            b(i,j) = Inf;
            fprintf(1, ', b2 = Inf\n');
            continue;
        end
        fprintf(1, ', b2 = %f\n', b(i,j));
        ini.b2 = b(i, j);
        if exitflag == 1 && (b(i,j) > 0) && (b(i,j) <
  1) ...
                &&
  (swcheck(ini,stimate(ini,geo,'wst'),0)==1)
                        outs =
  wstmain(geo,inputs,eCs,ycoors,ini,1);
                        for k=1:size(inputs, 1)
                                tmp = outs{k};
                                Y = tmp(:, 2);
                                out = tmp(:, 3);
                                E(i,j) = E(i,j) +
  sum((real(Y(1:size(out,1))-
  out(:,1))).^2)/size(out,1)/size(inputs,1);
                        end
```

```
        else
            E(i,j)=Inf;
        end
    end
end
if (sum(sum(E(:,:)<Inf)) > 0)
    [i,j]=find(E==min(min(E)));
    ini.a1 = a1(i,1);
    ini.a2 = a2(j,1);
    ini.b2 = b(i,j);
    if swcheck(ini,stimate(ini,geo,'wst'),0)==0
        errormsg(output)
    end
else
    errormsg(output)
end

function fun = fun(b2,ini,work)
if(b2 > 1 || b2 < 0)
    fun = 1E12;
else
    fun=1/2*ini.ft*(b2/ini.a2+(1-b2)/(ini.a1-
  ini.a2)*(ini.a2-ini.a1*b2)/ini.a2)...
        -work;
end
function errormsg(output)
fprintf(1, 'iniialization algorithm has failed due to the
  below mentioned reason.\n')
fprintf(1, 'Please conduct a manual iniialization. The
  best estimate on the constitutive\n')
fprintf(1, 'parameters obtained by the algorithm is
  stored in. Only ft and E\n')
fprintf(1, 'will be meaningful in this file.\n')
```

wstmain.m:

```
function pres= wstmain(geo,inputs,eCs,ycoors,est,p)
%returns the residue of all curves
%obs contains the CMOD
m = geo.m; a0 = geo.a0; am = geo.am; bm = geo.bm;
d1 = geo.d1; d2 = geo.d2; h = geo.h; L1 = geo.L1; t =
  geo.t;
mu = geo.mu; L2=geo.L2; alpha_w = geo.alpha_w/180*pi;
s=stimate(est,geo,'wst'); g = 9.82;
ft=est.ft; a1=est.a1; a2=est.a2; b2=est.b2; E=est.E;
m = m/2;
alpha_w = alpha_w/180*pi;
beta1 = ft*a1*s/E; beta2 = ft*a2*s/E;
A_1 = bm*(L1-h-a0); A_2 = (L2/2-am/2)*a0; A_3 = L2/2*h;
A = A_1 + A_2 + A_3;
e = (L2/2-bm/2)*A_1/A + (L2/4+am/2)*A_2/A + L2/4*A_3/A;
kmu = (2*tan(alpha_w)+2*mu)/(1-mu*tan(alpha_w));
c = (1-b2)*(1-beta1)/(beta2-beta1);
p_0 = (ft*h^2*t-6*m*g*e)/(6*d2+3*d1*kmu-2*h);
theta_0_1 = 1 - 1/(ft*h*t)*p_0;

options =
  optimset('Display','off','MaxFunEvals',50000,'MaxIter',
  50000,...
    'TolFun',1e-13);
red = 0.09;
pres = cell(size(inputs,1),1);
parfor k=1:size(inputs,1)
        [fid, msg] = fopen(inputs{k}, 'r');
        if fid > 0
                cnt = textscan(fid, '%f %f', ...
                       'Delimiter', ',', ...
                       'HeaderLines', 1, ...
                       'ReturnOnError', 0);
                fclose(fid);
                X = cnt{1} * 0.001;
                Y = cnt{2};
                [COD,Y] = datared(X,Y,red);
```

```
                cmod_0 = p_0/E/t/eCs(k);
                fprintf(1, 'P0 = %f N, CMOD_0 = %f mm\n',
  p_0, cmod_0 *1000);
                row = 1;
        if p == 0
                        pts = 0;
                        while COD(row) <= cmod_0
                                pts = pts + 1;
                        end
                        pre = zeros(pts);
                else
                        pre = zeros(size(COD));
        end
        row = 1;
        while COD(row) <= cmod_0
                        pre(row,1)=COD(row)*E*t*eCs(k);
                        row=row+1;
        end
        x = [1.01*theta_0_1 ; 1.01*p_0];
                if p > 0
                        for i=row:size(COD,1)
                                x =
  fsolve(@fun,x,options,ft,h,t,ycoors(k),c,beta1,beta2,b2
  ,d2,kmu,d1,m,g,e,...
                                                s,E,COD(i));
                                pre(i,1)=x(2);
                        end
                end
                pres{k} = [COD Y pre];
        else
                fprintf(1, 'file %s is failed to open due
  to: %s\n', input, msg);
        end
end

function F =
  fun(x,ft,h,t,ycoor,c,beta1,beta2,b2,d2,kmu,d1,m,g,e,s,E
  ,cmod)
rho = 1/(ft*h*t)*x(2);
```

```
theta_1_2  =  1/2*(1-rho-c+sqrt((1-rho-c)^2+c^2/(beta1-1)));
theta_2_3 = 1/2*(rho*(beta2-
  1)+b2/beta2+sqrt(rho^2*(beta2-1)^2+2*rho*(beta2...
    -1)*b2/beta2+(1-b2)^2/(beta1-beta2)+b2^2/beta2));
switch 1
    case x(1) <= theta_1_2
        alpha = 1-beta1-sqrt((1-beta1)*((1-rho)/x(1)-
  beta1));
        mu = 4*(1-3*alpha+3*alpha^2-alpha^3/(1-
  beta1))*x(1)+(6*alpha-3)*(1-rho);
        bi = 1; betai=beta1;
    case x(1) <= theta_2_3
        alpha = 1-beta2-(1-b2)/2/x(1)-sqrt((1-beta2)*((1-
  b2)^2/4/x(1)^2/(beta1...
            -beta2)-beta2+(b2-rho)/x(1)));
        mu = 4*(1-3*alpha+3*alpha^2-alpha^3/(1-
  beta2))*x(1)+(6*alpha-3)*(1-rho)...
            -(1-b2)*(3*alpha^2-(c/2/x(1))^2)/(1-beta2);
        bi = b2; betai=beta2;
    case x(1) > theta_2_3
        alpha = 1-1/2/x(1)*(1+sqrt((1-b2)^2/(beta1-
  beta2)+b2^2/beta2-4*rho*x(1)));
        mu = 4*x(1)*(1-3*alpha+3*alpha^2-
  alpha^3)+(6*alpha-3)*(1-rho)-3*alpha^2+...
            1/4/x(1)^2*(1-b2/beta2)*(1-
  b2/beta2+c)*(1+beta1*c/(1-beta1))...
            +(c/2/x(1))^2;
        bi = 0; betai=0;
end
F(1) = mu-6/(ft*h^2*t)*(x(2)*(d2-
  h/2)+1/2*kmu*x(2)*d1+m*g*e);
%F(2) = s*ft/E*(1-bi+2*alpha*(x(1)-1+ycoor/h))/(1-betai)
  - cmod;
phi=s*ft*x(1)/h/E;
y0=(1-alpha)*h/2;
F(2)=2*(ycoor-y0)*phi-cmod;
```

E1.m:

```
function E1 =
  E1(est,inputs,eCs,ycoors,geo,fix,lb,ub,type,warnings,i,
  rep,obstype)
inp = struct('ft', fix.ft, ...
             'a1', fix.a1, ...
             'a2', fix.a2, ...
             'b2', fix.b2, ...
             'E', est(1));
if (inp.E < lb.E)||(inp.E >
  lb.E)||(swcheck(inp,stimate(inp,geo,type),0)==0)
    E1=1e12;
    %warn(warnings,1,stimate(inp,geo,type),inp,lb,ub,i,re
  p,1);
else
        outs = wstmain(geo,inputs,eCs,ycoors,inp,0);
        E1 = 0;
        for k=1:size(outs,1);
                ret = outs{k};
                Y = ret(:, 2);
                out = ret(:, 3);
                E1 = E1 + sum((real(Y(1:size(out,1))-
  out(:,1))).^2)/size(out,1)/size(outs,1);
        end
    fprintf(1, '%g\n', E1);
end
```

E2.m:

```
function E2 =
  E2(est,inputs,eCs,ycoors,geo,fix,lb,ub,type,warnings,
  i,rep,obstype)
inp = struct('ft', est(1), ...
             'a1', est(2), ...
             'a2', fix.a2, ...
             'b2', fix.b2, ...
             'E', fix.E);
fprintf(1, 'Trying ft = %g, a1 = %g, ret = ', inp.ft,
  inp.a1);
if (inp.ft<lb.ft) ||(inp.a1<lb.a1) ||(inp.ft>ub.ft)
  ||(inp.a1>ub.a1) ...
    ||(swcheck(inp,stimate(inp,geo,type),0)==0)
    E2=1e12;
    fprintf(1, '%g\n', E2);

  %warn(warnings,1,stimate(inp,geo,type),inp,lb,ub,i,re
  p,2);
else
        outs = wstmain(geo,inputs,eCs,ycoors,inp,1);
        E2 = 0;
        for k=1:size(outs,1);
                ret = outs{k};
                Y = ret(:, 2);
                out = ret(:, 3);
                E2 = E2 + sum((real(Y(1:size(out,1))-
  out(:,1))).^2)/size(out,1)/size(outs,1);
        end
    fprintf(1, '%g\n', E2);
end
```

E3.m:

```
function E3 =
  E3(est,inputs,eCs,ycoors,geo,fix,lb,ub,type,warnings,i,
  rep,obstype)
inp=struct('ft', fix.ft, ...
           'a1', fix.a1, ...
           'a2', est(1), ...
           'b2', est(2), ...
           'E', fix.E);
fprintf(1, 'Trying a2 = %g, b2 = %g, ret = ', inp.a2,
  inp.b2);
if
  (inp.a2<lb.a2)||(inp.b2<lb.b2)||(inp.a2>ub.a2)||(inp.b2
  >ub.b2)||...
        (swcheck(inp,stimate(inp,geo,type),0)==0)
    E3=1e12;
    fprintf(1, '%g\n', E3);
    %warn(warnings,1,stimate(inp,geo,type),inp,lb,ub,i,re
  p,3);
else
        outs = wstmain(geo,inputs,eCs,ycoors,inp,1);
        E3 = 0;
        for k=1:size(outs,1);
                ret = outs{k};
                Y = ret(:, 2);
                out = ret(:, 3);
                E3 = E3 + sum((real(Y(1:size(out,1))-
  out(:,1))).^2)/size(out,1)/size(outs,1);
        end
    fprintf(1, '%g\n', E3);
end
```

stimate.m:

```
function s = stimate(inp,geo,type)
switch 1
    case strcmp(type,'wst')
        % s=0.20*geo(7); %This value fits experimental
  results [8]
        s=0.84*geo.h; %This value fits FEM calculations
  [6]
    case strcmp(type,'tpbt')
        % s=0.70*geo(2);%This value fits experimental
  results [8]
        s=0.50*geo(2); %This value fits FEM calculations
  [8], [2]
end
```

swcheck.m:

```
function swcheck = swcheck(inp,s,output)
beta1 = inp.ft*inp.a1*s/inp.E;
beta2 = inp.ft*inp.a2*s/inp.E;
w1=(1-inp.b2)/(inp.a1-inp.a2);
s1=inp.b2-inp.a2*w1;
switch 1
    case output == 0
        if (beta1 >= 1)||(beta1 == 0)||(isinf(beta1) ==
  1)||(beta2 <= 0)...
                ||(beta2 >= 1)||(beta2 == beta1)||(w1 <=
  0)||(s1 <= 0)||...

  (isnan(inp.ft)==1)||(isnan(inp.a1)==1)||(isnan(inp.a2)=
  =1)...
                ||(isnan(inp.b2)==1)||(isnan(inp.E)==1)
            swcheck=0;
        else
            swcheck=1;
        end
    case output == 1
        switch 1
            case (beta1 >= 1), fprintf(1, 'Invalid s-w
  curve. beta1>=1');
                swcheck=0;
            case (beta1 == 0), fprintf(1, 'Invalid s-w
  curve. beta1=0');
                swcheck=0;
            case (isinf(beta1) == 1), fprintf(1, 'Invalid
  s-w curve. beta1=inf');
                swcheck=0;
            case (beta2 <= 0), fprintf(1, 'Invalid s-w
  curve. beta2<=0');
                swcheck=0;
            case (beta2 >= 1), fprintf(1, 'Invalid s-w
  curve. beta2>=1');
                swcheck=0;
```

```
            case (beta2 == beta1), fprintf(1, 'Invalid s-
    w curve. beta1=beta2');
                swcheck=0;
            case (w1 <= 0), fprintf(1, 'Invalid s-w curve.
    w1<=0');
                swcheck=0;
            case (s1 <= 0), fprintf(1, 'Invalid s-w curve.
    s1<=0');
                swcheck=0;
            case (isnan(inp.ft)==1),fprintf(1, 'Invalid
    tensile strength. ft = NaN');
                swcheck=0;
            case (isnan(inp.a1)==1),fprintf(1, 'Invalid
    first slope. a1 = NaN');
                swcheck=0;
            case (isnan(inp.a2)==1),fprintf(1, 'Invalid
    second slope. a2 = NaN');
                swcheck=0;
            case (isnan(inp.b2)==1),fprintf(1, 'Invalid
    cut-off. b2 = NaN');
                swcheck=0;
            case (isnan(inp.E)==1),fprintf(1, 'Invalid
    Youngs modulus. E = NaN');
                swcheck=0;
            otherwise
                swcheck=1;
        end
end
```

wst_forward.m:

```
function wst_forward(input,mts,output,geometry,est)
tic

if nargin <= 4
    red = 0.009;
end
if nargin == 3
    geometry = 'wstgeometry.dat';
end
%geo=textread(geometry);
%data=textread(input);
[fid, msg] = fopen(mts, 'r');
if fid > 0
    cnt = textscan(fid, '%f %f %f', 'headerlines', 1,
  'Delimiter', ',');
    ext = cnt{1};
    force = cnt{3};
else
    fprintf(1, 'Failed to open %s due to: %s\n', mts,
  msg);
    ext = [];
    force = [];
end
work = trapz(ext, force); % work in lb * inch
work = work * 4.448 * 0.0254; % in N * m
fprintf(1, 'work = %f N*m\n', work);
[fid, msg] = fopen(geometry, 'r');
if fid > 0
    cnt = textscan(fid,
  '%f %f %f %f %f %f %f %f %f %f %f %f', 'HeaderLines', 1,
  'Delimiter', ',');
    geo = struct('m', cnt{1}, ...
        'a0', cnt{2}, ...
        'am', cnt{3}, ...
        'bm', cnt{4}, ...
        'd1', cnt{5}, ...
        'd2', cnt{6}, ...
```

```
        'h', cnt{7}, ...
        'L1', cnt{8}, ...
        't', cnt{9}, ...
        'mu', cnt{10}, ...
        'L2', cnt{11}, ...
        'alpha_w', cnt{12});
else
    fprintf(1, 'Failed to open %s due to: %s\n', mts,
  msg);
end
fprintf(1, 'Input parameters (inches): m = %f kg, a0 = %f,
  am = %f, bm = %f, d1 = %f, d2 = %f\n', ...
    geo.m, geo.a0/0.0254, geo.am/0.0254, geo.bm/0.0254,
  geo.d1/0.0254, geo.d2/0.0254);
fprintf(1, 'h = %f, L1 = %f, L2 = %f, mu = %f, alpha_w
  = %f degree\n', ...
    geo.h/0.0254, geo.L1/0.0254, geo.L2/0.0254, geo.mu,
  geo.alpha_w);
[fid, msg] = fopen(input, 'r');
if fid > 0
    c = textscan(fid, '%q %f %f', 'HeaderLines', 1,
  'Delimiter', ',');
    inputs = c{1};
    eCs = c{2};
    ycoors = c{3};
else
    fprintf(1, 'Failed to open input file due to: %s\n',
  msg);
    inputs = [];
    eCs = [];
    ycoors = [];
end

if swcheck(est,stimate(est,geo,'wst'),1) == 1
    out=wstmain(geo,inputs, eCs, ycoors, est,1);
    %resplot(X,Y,out,input,'cmod')
    rows=max(arrayfun(@(x) size(x{1,1},1), out));
    ret = zeros(rows, size(out, 1) * 3);
    arrayfun(@(x) size(x{1,1},1), out));
```

```
    for i=1:size(out)
        o = out{i};
        ret(1:size(o,1), 3*i-2:3*i) = o;
    end
    dlmwrite(output, ret,',')
    res = arrayfun(@(x) mean((x{1,1}(:,2)-
  x{1,1}(:,3)).^2), out);
    res = mean(res);
    fprintf(1, 'residue = %f\n', res);
    res = 0;
    for k=1:size(out,1)
                ret = out{k};
                Y = ret(:, 2);
                o = ret(:, 3);
                res = res + mean((Y-o).^2)/size(out,1);
    end
    fprintf(1, 'residue = %f\n', res);
    fprintf(1, 'Time = %f sec\n', toc);
    %disp(['Time =' blanks(1) num2str(toc,3) blanks(1)
  'sec'])
end
```

ELECTRICAL PROPERTIES OF GEOPOLYMERS SYNTHESIZED USING FOUR DIFFERENT FLY ASHES

ABSTRACT

Electric properties measurement is an effective method to study cementitious materials at both the micro- and macroscale. This study examines and compares the electrical properties of geopolymers synthesized using four locally available fly ashes. Both the fixed frequency and spectral measurements were carried out during the curing and after the curing of geopolymers to gain insight into the geopolymerization process of the geopolymers over more than one year. During the curing of geopolymers at 75 °C, both the magnitude of the electrical impedance and the electrical resistance measured at frequency of 10 KHz increase with the curing time, suggesting that both the magnitude of the electric impedance or the electric resistance can be used as an indicator of the degree of geopolymerization. It has been found that the calcium content plays an important role in the electrical resistance evolution of the geopolymer during curing. The electrical resistance of the geopolymer with high calcium content increases faster than that with lower calcium content during the curing. The evolution of the electrical impedances of four geopolymers was monitored over one year. Testing results show that the bulk resistance or the diameters of the high frequency arcs of all geopolymers increase with age during the whole testing period, suggesting that the polymerization is a very long process. The bulk electric resistance of the geopolymer at late age can be a few orders of magnitude higher than that at early age.

1. INTRODUCTION

Geopolymers are amorphous three-dimensional alumino-silicate binder materials. They can be synthesized by mixing source material (alumino-silicate reactive materials such as metakaolin, fly-ashes) and an alkaline activator (strong alkaline solutions such as NaOH or KOH) and then curing at room or elevated temperature. Compared with OPC, geopolymers possess the following advantages: a) less energy consumption and CO_2 emission (20% of the carbon dioxide emissions produced in the manufacture of OPC) during manufacture, b) higher strength and much less shrinkage, c) lower permeability (comparable to natural granite), and d) substantially higher resistance to fire and acid attacks. Geopolymers are considered as "green materials" and strong candidates to replace OPC in selected applications leading to more sustainable infrastructure system.

Extensive studies have been carried out on geopolymer mortars/concretes in last two decades. Most of these works focus on the mechanical properties of the geopolymers. The electrical properties of geopolymers, however, have received very little attention. Electrical properties of OPC binder have been studied over a long period (McCarter and Brousseau, 1990). This is because the electrical conductivity or resistivity of cement paste is mainly caused by the ion transport through the pore solution in cement-based cement, which mainly depends on both pore solution conductivity and porosity. Both the pore solution conductivity and porosity evolve with the hydration of cement, which is a dissolution-precipitation process. At the initial stage of the hydration, the conductivity would increase with the release of the ions from the cement. As the hydration develops, the solid structure would hamper the movement of the charge carriers and the free water in pores used to be

connected would be separated, which would decrease the conductivity, as observed in experimental studies (Tamás et al., 1987; Morsy, 1999).

In early study of the electrical properties of concretes, the resistance or its reciprocal, conductance, was measured and related its change to the degree of hydration of the concrete (Tamás, 1982; Morsy, 1999). To this end, the resistance of conductance of the specimen is measured at a fixed frequency of electrical field or a narrow frequency range. Measured resistance is assumed due to the ionic transport in the specimen. Usually, an alternating current is used to minimize the influence of the electrochemical processes taking place at the electrode/cement interface. This is because the contribution of the electrode/cement interface to the measured resistance is very significant at low frequency and reduces rapidly at high frequency. The major drawback of the resistance/conductance measurement method is that the results are only applicable at certain frequencies of the electrical field. To overcome this drawback, electrical impedance spectroscopy (EIS) method has been developed, in which the electrical impedance spectrum of the specimen is measured for a large range of frequency (Carter and Brousseau, 1990). The measured complex impedance spectrum is usually expressed as a Nyquist plot as shown in Fig. 1, in which the *x*-axis is the real part of the impedance and the *y*-axis is the negative of the imaginary part of the impedance. Usually, two arcs exist on a typical complex impedance response of a concrete specimen, as shown Fig. 1. The right arc is the low frequency branch which is related to the effect of the electrode/cement interface. The left arc is the high-frequency branch which reflects the resistance/conductivity of the bulk material, the specimen between the electrodes. Two arcs meet at a point where the imaginary part reaches its minimum. The

corresponding real impedance is the bulk resistance of the sample, which is independent of frequency (Schwarz et al., 2007).

Existing studies suggest that electric properties measurement is an effective method to study cementitious materials at both the micro- and macroscale. Both the fixed frequency and spectral measurements can be used to study the electrical properties of concrete, as summarized by McCarter et al. (McCarter et al., 2003). It is reasonable to assume that these methods are also applicable to geopolymers. The electric properties of geopolymers largely depend on free alkali metal ions. However, very few detailed studies have been reported on the electrical properties on geopolymer. Cui et al. (Cui et al., 2008) investigated the conductivity of geopolymers made with different mix ratios. The measured AC conductivity of the harden geopolymer was 1.5×10^{-4} S m^{-1} at room temperature. Hanjitsuwan et al. (Hanjitsuwan et al., 2011) measured the electrical conductivity and dielectric constant of fly ash geopolymer pastes and found that they were dependent on the frequency range and liquid alkali to ash ratio.

In this study, electric properties of geopolymers made from four different fly ashes were examined using both the fixed frequency and spectral measurements to gain fundamental understanding of the strength development of fly ash based geopolymers.

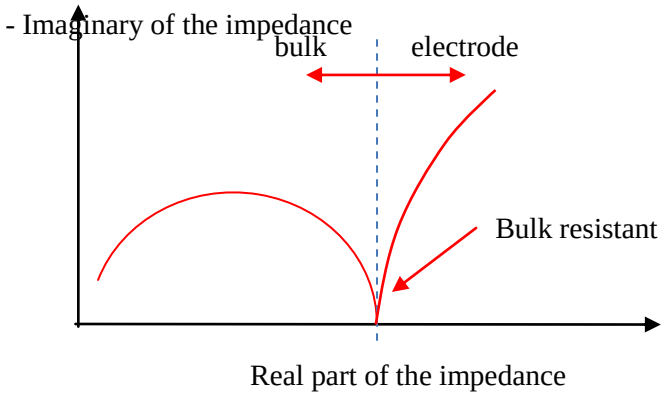

Fig. 1. Typical Complex Impedance Response of Concrete

2. MATERIALS AND METHODS

2.1. Geopolymer Mortars

Fly ash based geopolymer mortar specimens were manufactured using four fly ashes. These fly ashes were chosen for two reasons: 1) both the high calcium and low calcium fly ashes are included; and 2) two fly ashes with very similar chemical compositions are included. In this way, we are able to examine the difference of the electrical properties of geopolymers caused by high and low calcium fly ash, and to compare the electrical properties of geopolymers made from fly ashes with similar chemical composition. The chemical compositions of these fly ashes are shown in Table 1. It can be seen that the fly ash from Miller is class C fly ash, and the rest fly ashes are class F (low calcium) fly ashes. Fly ashes from Gaston and Orlando have very similar chemical compositions.

To determine the content of the amorphous material in fly ash samples which could actually participate in the geopolymerization, dissolution testing was carried out to measure the dissolution degrees of fly ashes in aqueous 14M NaOH solution. Five samples were

tested for each fly ash and the dissolution degree was determined as the loss of the mass of the fly ash after soaking in NaOH solution over 24 hours at 75°C.

A mix of Sodium Hydroxide (NaOH) solution and Sodium Silicate solution was chosen as the activator of the geopolymer. Sodium Silicate solution is lab level from Fisher Scientific containing 29.4 wt% of SiO_2, 9.1 wt% of Na_2O, and 61.5 wt% of water. Only fine aggregates were used to synthesize geopolymer mortars. Superplasticizer was also used to enhance the workability. All geopolymer mortar made in this study contain 60 wt% of sand. The molar ratio of SiO_2/Al_2O_3 was chosen as 3.8 and the molar ratio of Na_2O/Al_2O_3 was chosen as 0.8. The concentration of NaOH aqueous solution was 14M. In such a case, the mix design of the geopolymer using fly ash from Gaston can be obtained and shown in Table 2. The produced specimens were cured in oven for 48 hours at 75 °C.

Table 1. Chemical Composition of Fly Ashes

Source	SiO_2	Al_2O_3	Fe_2O_3	SO_3	CaO	Moisture	LOI	Na_2O
Orlando	54.48%	27.72%	8.14%	0.11%	1.29%	0.15%	4.11%	0.67%
Miller	36.23%	19.41%	6.45%	1.84%	23.11%	0.11%	0.61%	1.50%
Martin Lake	54.88%	19.31%	8.46%	0.45%	8.03%	0.10%	0.04%	0.62%
Gaston	50.38%	27.20%	9.14%	0.30%	2.49%	0.14%	2.95%	0.69%

Table 2. Mix Design of Geopolymer Using Fly Ashes from Gaston (in Mass)

Ingredients	fly ash	Sodium silicate	NaOH solution	super plasticizer	Sand
Content (wt%)	24.48%	8.68%	6.84%	2.00% of fly ash	60%

2.2. Electrical Properties Measurements

The electrical properties of the produced geopolymer specimens were studied using both the fixed frequency and spectral measurements. In the fixed frequency measurement, an AC with frequency of 10 kHz and voltage of 2V was applied to the two electrodes embedded in

the geopolymer specimen. The current intensity that went through the sample was recorded. The resistance of the specimen was calculated by $R=U/I$, where U is the applied voltage, and I is current intensity. In the spectral measurement, a HP 4191A impedance analyzer was used to measure the impedance of the geopolymers.

3. RESULTS AND DISCUSSIONS

3.1. Properties of Geopolymers

Dissolution testing shows that the dissolvable composition in different fly ashes varies significantly, as shown in Table 3. Orlando fly ash has a dissolution degree as high as 62.25%; while the Miller fly ash has a very low dissolution degree of 33.14%.

Table 3. Dissolution Degree of Fly Ashes

Fly ash	Gaston	Orlando	Miller	Martin Lake
Dissolution (%)	57.2	62.25	33.14	48.6

Cylindrical samples of geopolymer with size of 2×4 in. were manufactured to measure the compressive strength in compliance of ASTM C39-05. The loading rate was chosen as 0.03 in/min so that the stress rate was within 35×10^7 psi/s as specified in ASTM C39-05. Before testing, specimens were capped with sulfate cement so that both surfaces were flat and parallel. The compressive strength of four geopolymer mortars were obtained and shown in Fig. 2. It can be seen that geopolymer using fly ash from Gaston has the highest compressive strength. While geopolymer based on fly ash from Orlando is lower, even though the chemical composition and dissolution degree of this fly ash are very close to that of the fly ash from Gaston. The strength of the geopolymer specimens based on fly ash from Martin Lake is much lower than those based on fly ashes from Gaston and Orlando because its dissolution degree is much lower. Geopolymer specimens based on high calcium fly ash

from Miller exhibits a higher compressive strength than that produced by fly ash from Martin Lake although it has a low dissolution degree. This may be because some calcium silicate hydrate was also formed in this geopolymer which can reinforce the geopolymer gel, leading to higher strength.

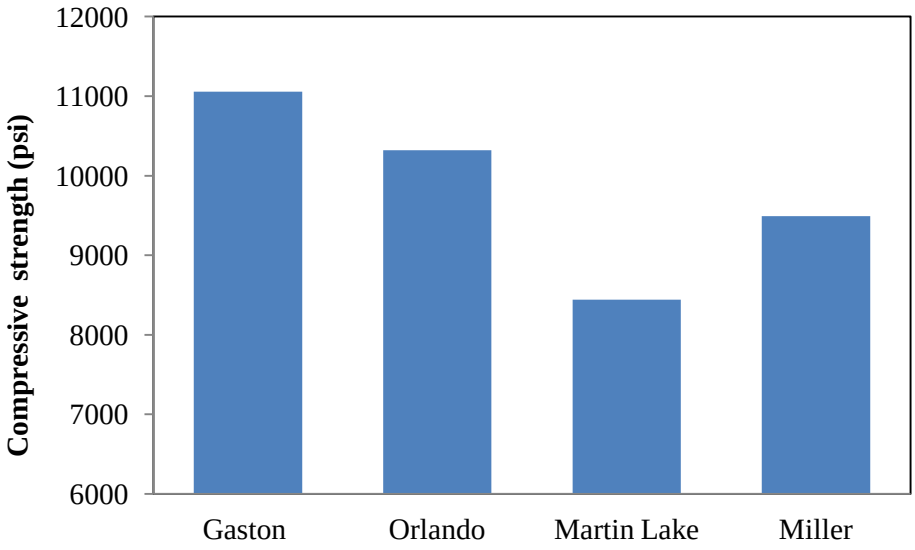

Fig. 2. Compressive Strengths of Geopolymers Mortars Made from Fly Ashes from Four Different Sources

3.2 Electrical Properties Evolution during the Curing of Geopolymers

Electrical impedance of the geopolymer specimen made of fly ash from Gaston was monitored during its curing at 75 °C in an oven. The Nyquist plots of the measured spectra at different curing time are shown Fig. 3. It can be seen that a full loop is formed for each measured spectrum. This is quite surprising because no such Nyquist plot has been reported. Further study is needed here to understand why a full loop can be formed here.

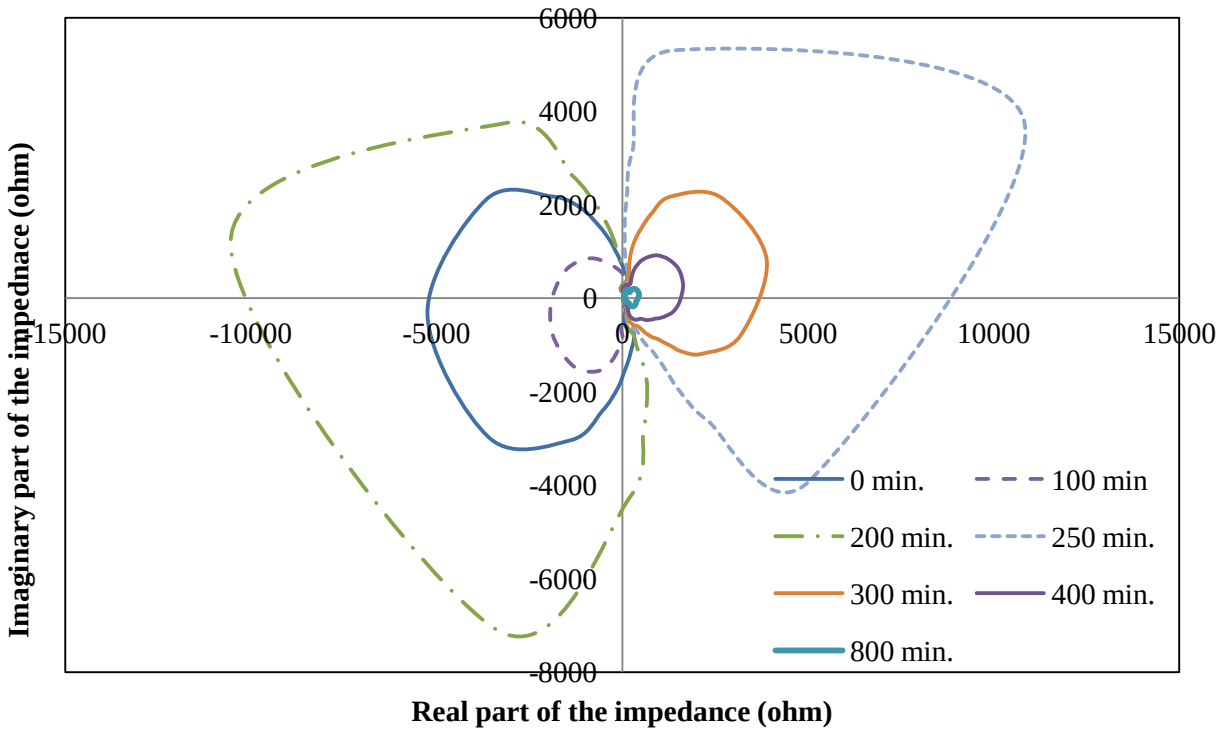

Fig. 3. Evolution of Nyquist Spectra of the Geopolymer Specimen Made from Gaston Fly Ash with Time during Curing.

The size of the loop of the Nyquist plot increases at the beginning with the curing time. After about 4 hours curing, this loop suddenly flips to the right side of the coordinate system, as shown by the loop of 250 minutes curing in Fig. 3. It is unclear what causes such a flip. After that, the size of the loop reduces with curing time. Although a clear physical meaning of the observed phenomenon is not available yet, Fig.3 suggests that the electrical impedance varies with the degree of the geopolymerization of the specimen, and therefore, can be used as an indicator for the degree of the geopolymerization. Fig. 4 shows the magnitude of the electrical impedance of the geopolymer varying with curing time for a wide range of frequency between 100 Hz – 10 MHz. It can be clearly seen that the magnitude of the impedance increases monotonously with curing time within the range of

100 Hz – 1 MHz. Therefore, magnitude of the electrical impedance of the geopolymer provides another indicator of the degree of polymerization.

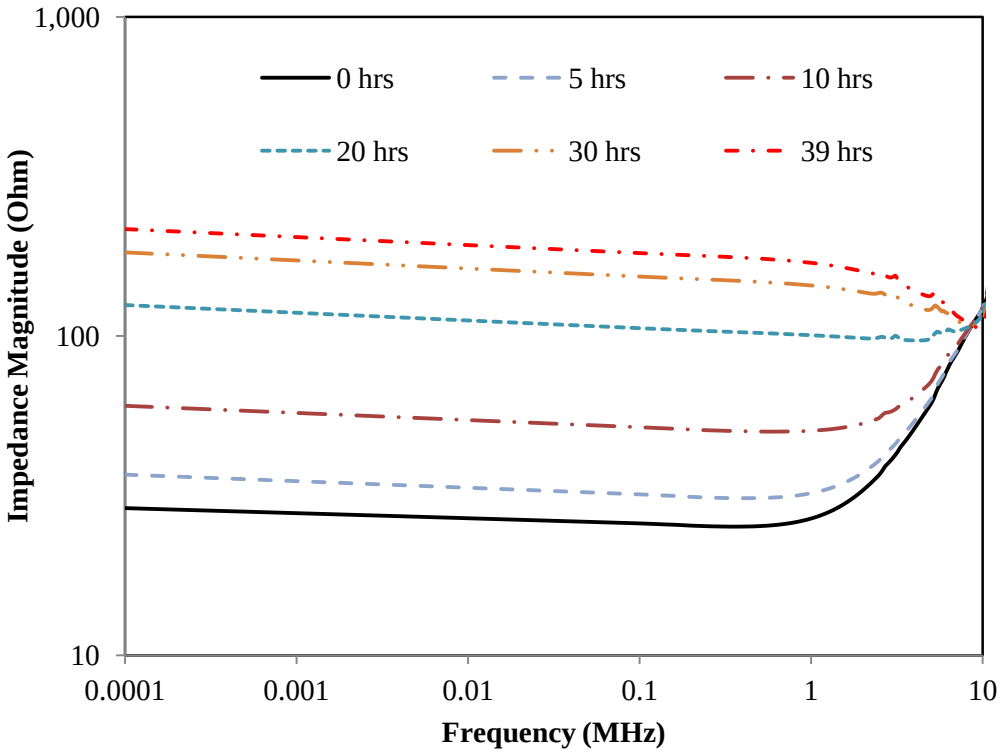

Fig. 4. Evolution of the Impedance Magnitude with Curing Time

No bulk resistance of the specimen can be obtained from Fig. 3. However, Fig. 4 shows that magnitudes of the electrical impedance with the frequency less than 1 MHz all increase monotonously with curing time. This suggests that electric resistance measured with this frequency range shall bear the same trend. Therefore, electric resistance measured at fixed frequency (10 KHz) was used here to examine the geopolymerization processes of four geopolymers. The measurement results are shown in Fig. 5. Three duplicated specimens were tested for each geopolymer shown in the figure. During the manufacture of the specimens, a delay time (2h) was introduced after the geopolymer mortar specimens were cast into the mold and before they were put into the oven for curing, because this delay time

could be beneficial to the strength development (Chindaprasirt et al., 2007) of the geopolymers. Figure 5(b) shows that electrical resistances of these fresh geopolymers remain almost unchanged in this first two hours of delay time, suggesting that no or little reaction between the fly ash and alkaline activator occurred in this period. This stage is clearly the induction period of the geopolymerization. Figure 5(b) also shows that the higher the content of CaO in the fly ash, the lower the resistance the fresh geopolymer is. This may be caused by the temperature rise induced by the reaction between CaO and water. High content of CaO in the fly ash can cause higher temperature rise in the fresh geopolymer, which accelerate the movement of ions in the fresh geopolymer, leading to lower electrical resistance.

After the samples were cured in the oven, their temperatures rose quickly from the ambient temperature to 75 °C. As a result, the resistance drops sharply to a low level, as shown in Fig. 5. After the temperatures of the specimens were stable, the resistances of the geopolymer specimens would be mainly controlled by three factors: 1) continuous release of the ions from fly ashes which causes resistance to decrease, 2) consolidation of the geopolymerization products which causes the resistance to increase, 3) loss of water in the specimens which causes the resistance to increase. The driving force for the actual change of the resistance is the combination of these three factors. For all the geopolymer specimens examined in this study, their electrical resistances increase again with the curing time after 40 min. in the oven. Three stages can be seen on the evolution of electrical resistance with curing time of fly ash from Miller: a fast increase stage, a flat/slight increase stage and a final increase stage. The first fast increase stage should be dominated by the consolidation of the geopolymerization products, as pointed out by various researchers (van Jaarsveld et al

1997; Hardjito et al. 2004). The final increase stage should be dominated by the loss of moisture, while the flat/slight increase stage in the middle should be a combination of all these three factors. Similar features can be found on other three geopolymers.

Figure 5 (a) shows that fast increase stage of the all geopolymers last about 24 hours, suggesting that most geopolymerization was finished within one day. Due to the high reaction rate of CaO, the resistance increasing rate of the geopolymer made of fly ash with higher CaO content is higher too, as shown in Fig. 5(a). The final resistance of the geopolymers in the testing period seems dependent on the content of CaO too. Geopolymer made of high calcium fly ash from Miller has much higher electric resistance; while three low-calcium fly ash based geopolymers have similar electrical resistance at the end of the testing time.

The above observation indicates that the electrical resistance can be used to monitor the geopolymerization process during the curing. To verify this observation, compressive strengths of geopolymer specimens cured with different time were measured and shown in Fig. 6. It can be seen that the compressive strengths of the geopolymer specimens increase with curing time and reach their maximum at 22 hours curing, suggesting that most geopolymerization has been finished within this time. This is in good agreement with the electrical resistance measurement shown in Fig. 5(a). Figure 6 also shows that excessive curing can even reduce the compressive strength of the geopolymers.

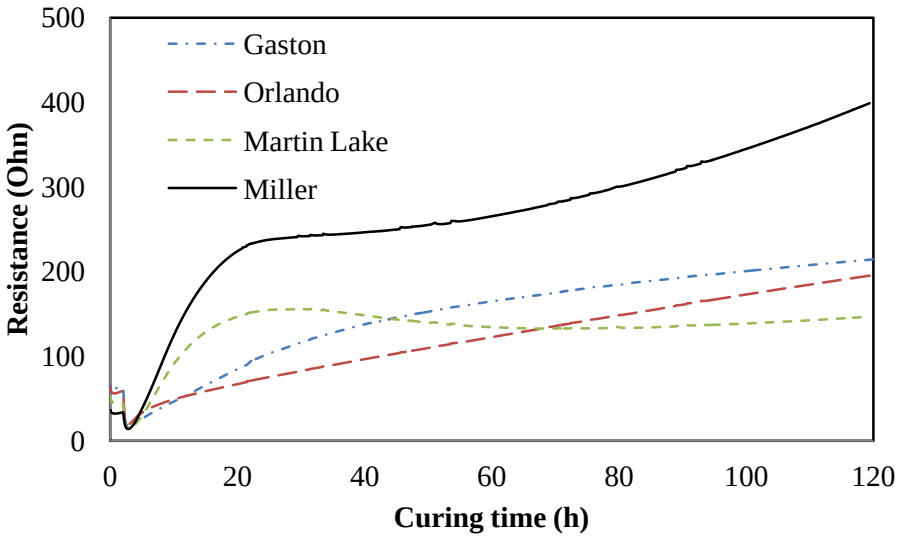

(a)

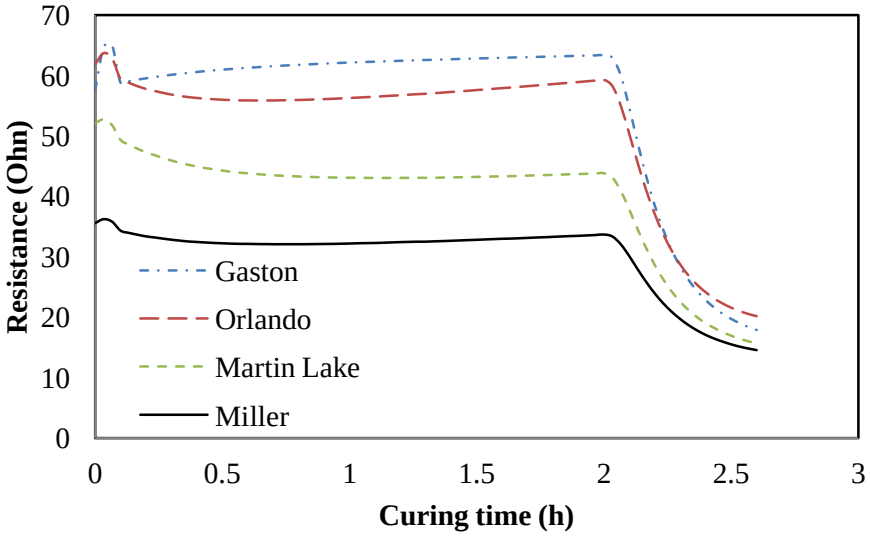

(b)

Fig. 5. Evolution of the Electrical Resistance with Curing Time: (a) Resistance Varying with Curing Time during the Whole Testing Time; (b) Resistance of the Fresh Geopolymer Samples before Curing

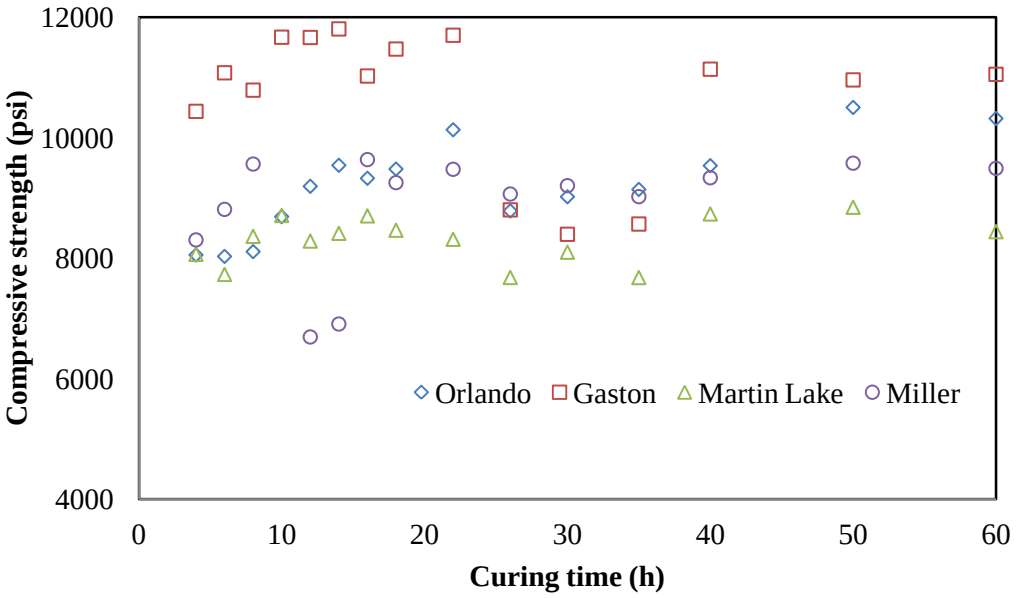

Fig. 6. Compressive Strength of Geopolymer Specimens Varying with Curing Time

3.3 Electrical Impedance Evolution with the Age of Geopolymers

Electrical impedances were measured for four geopolymers over one year to examine the long-term evolution of the electrical properties of geopolymer. In this test, geopolymer specimens were cast and cured in oven at 75 °C for 24 hours, and then stored in the laboratory environment. Figure 7 shows the Nyquist plots of the geopolymer specimens made of fly ash from Martin Lake. Figure 7(a) shows the Nyquist plots of this geopolymer at 5, 8, and 17 days. Two arcs can be clearly seen in these plots on which the bulk resistance can be determined. The diameter of the high-frequency loop increases with the age, implying that the bulk electrical resistance of this material increases with age. In Fig. 7(b), the Nyquist plots at age of 51, 108, and 384 days are presented. Because the frequency used in this test is too high, only the high-frequency arcs are captured in this figure. The diameter of the high-frequency arc continues growing with time over one year. At the end of the testing, the sizes of the high-frequency arc increases by two orders of magnitudes. Although

no bulk resistance can be read from this figure, it is in proportion of the diameter of the high-frequency arc of this geopolymer. A larger diameter of the high-frequency arc implies a higher bulk resistance. Figure 7(b) suggests that the bulk electric resistance of this geopolymer increased with age over the whole testing time. At the end of the testing, its bulk resistance is in the order of 10^5 ohm, which is in the same range as given by Davidovits (Davidovits, 2008).

Figure 8 compares the Nyquist plots of the electrical impedance spectra of four geopolymers at different ages. At an age of 8 days, the geopolymer made of fly ash from Miller has the highest bulk resistance, which is in agreement with the electrical resistant measurement shown in Fig. 5(a). At age of 108 days, the diameters of the high-frequency arcs of the geopolymer made of fly ash from Gaston and Orlando are much larger than that of the other two, as shown in Fig. 8(b). The diameters of the high-frequency arcs of all geopolymer specimens continue increasing after 108 days. At age of 384 days, the diameters of all the arcs are almost doubled for geopolymer made of fly ashes from Gaston and Orlando, as shown in Fig. 8(c). The diameters of the high-frequency arcs of the geoplymers made of fly ashes from Martin Lake and Miller increase almost four times during this period. It is interesting to see that the diameters of the high-frequency arcs are affected by the content of CaO in the fly ash. The higher the content of CaO in the fly ash, the smaller the diameter of the high-frequency arc of the Nyquist plot of the electrical impedance is. This may be caused by the fact that Ca^{2+} ions were not integrated into the geopolymer chains. Geopolymer made of fly ash with higher calcium content may contain more free Ca^{2+} ions and therefore have higher conductivity, leading to smaller diameter of the high-frequency arc. Another possible reason is that the dissolution degrees of fly ashes from

Gaston and Orlando are higher than that of the fly ashes from Martin Lake and Miller. As a result, reaction is more complete in the geopolymers based on the former two fly ashes, which consumes more free Na^+ ions and other ions released from the fly ash, and reduces the porosity of the geopolymers. Consequently, these two geopolymers have higher bulk electrical resistance.

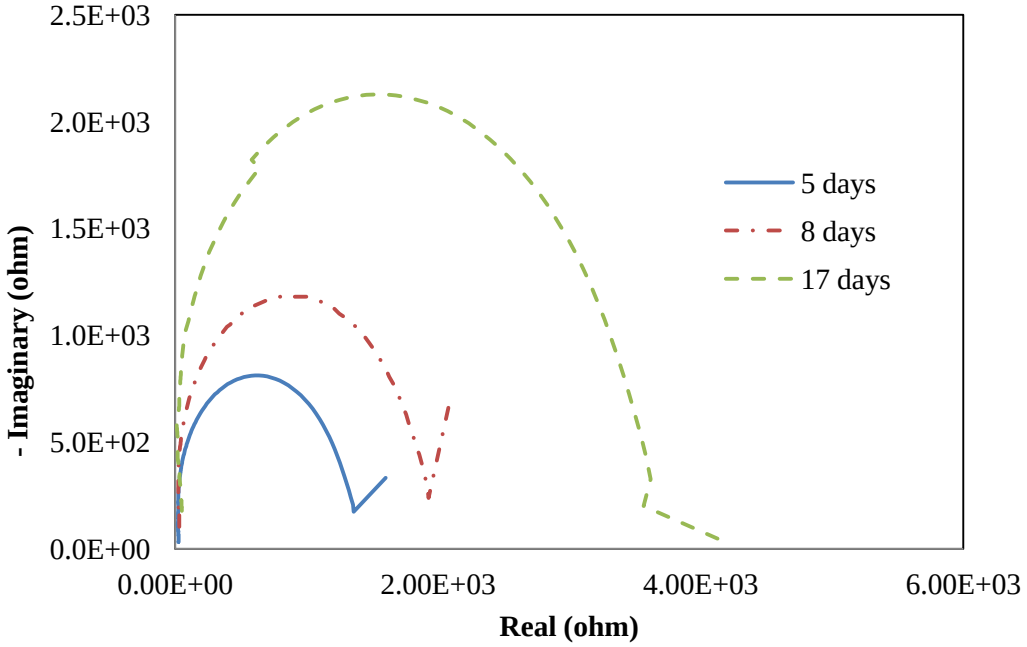

.

(a)

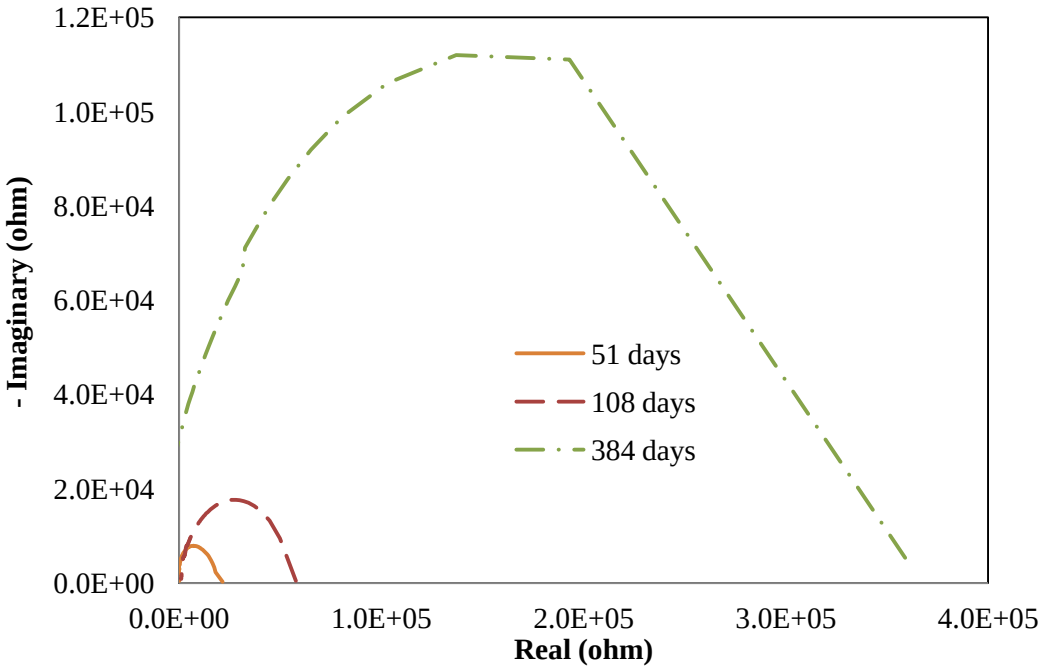

(b)

Fig. 7. Evolution of Nyquist Spectra of the Geopolymer Specimen Using Fly Ash from Martin Lake with Age

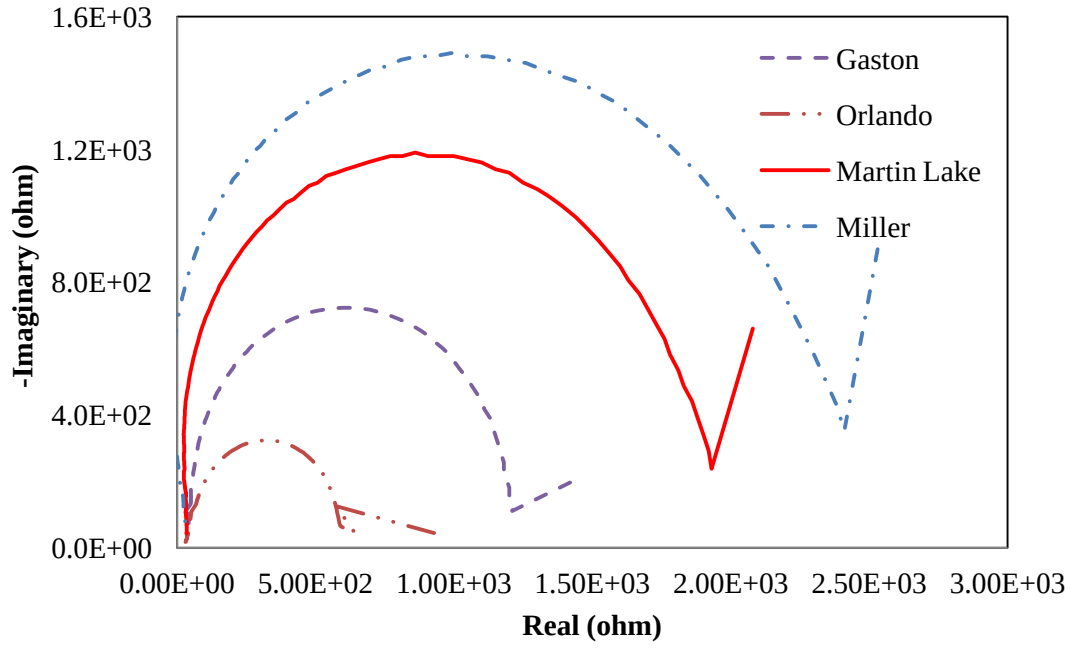

(a)

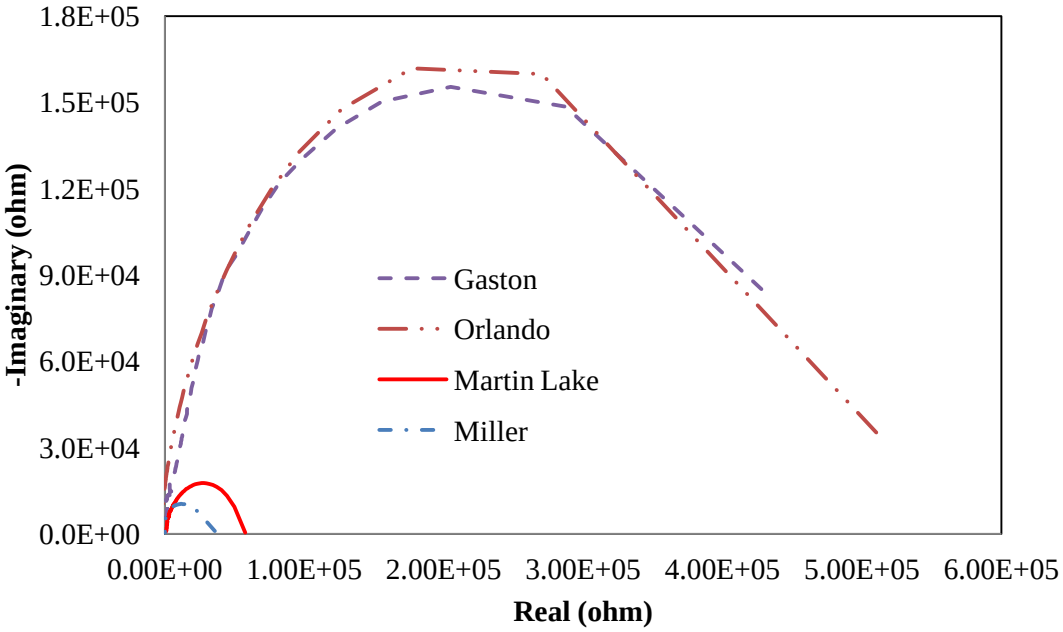

(b)

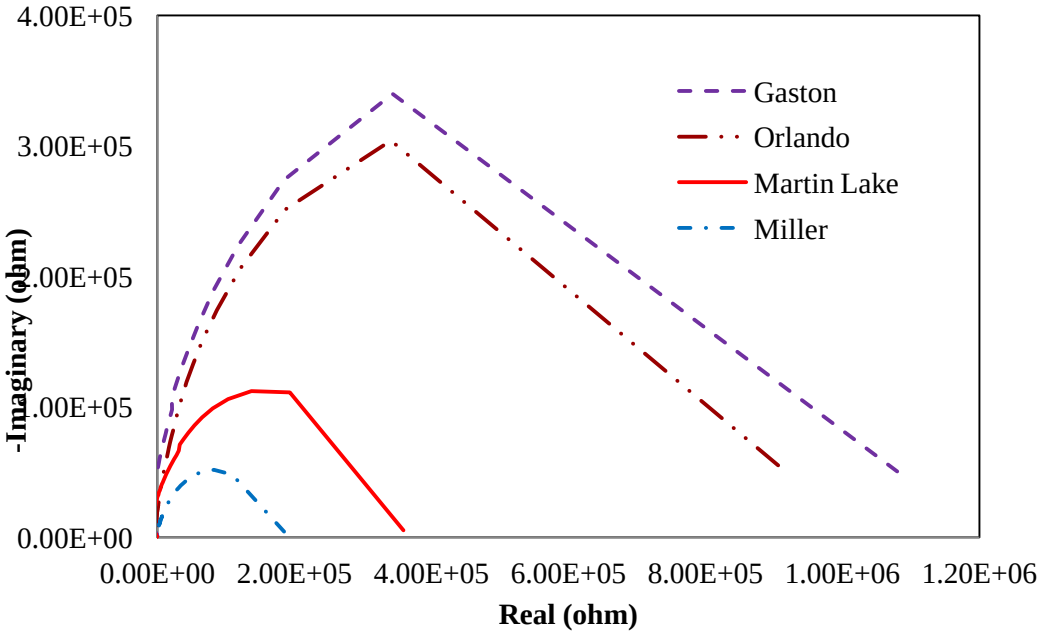

(c)

Fig. 8. Comparisons of Nyquist Spectra of Geopolymer Made from Four Different Fly Ashes: (a) 8 days; (b) 108 days; (c) 384 days.

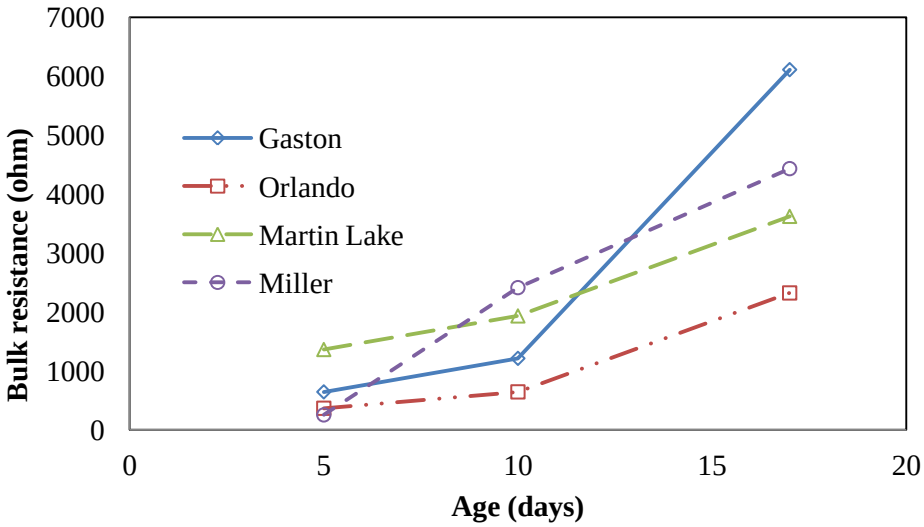

Fig. 9. Bulk Resistance of the Geopolymer Specimens Varying with Age

Figure 9 shows the bulk resistances of all geopolymers increase with age. However, their increasing rates are different. The bulk resistance of the geopolymer specimen made of fly ash from Gaston increases fastest with age in the period examined in Fig. 9. Although fly ash from Orland has very similar chemical composition and dissolution degree as fly ash from Gaston, the bulk resistance of geopolymer made of this material increases much slower. However, at age of 108 days, the electric resistances of these two geopolymers are almost identical, as shown in Fig. 8(b).

Figures 7–9 all suggest that the electrical properties of geopolymers vary with age in the testing period which is over one year. Two possible reasons are responsible for this evolution of the electrical properties: 1) unfinished geopolymerization in the specimens, and 2) loss of water in the testing specimens. Similar to the hydration in Portland cement, the geopolymerization of fly ash based geopolymer can take a very long period because the slow diffusion of reactive ions from the fly ash after fast reaction period at the early age shown in Fig. 5. The slow geopolymerization can consume free ions and reduce porosity in

the geopolymer specimens, leading to higher bulk resistance of the specimen. Water in the geopolymer will provide transport tool for free ions. Loss of water can therefore increase the bulk resistance of the specimen too. Since the specimens were stored in the laboratory environment, it is very likely that they lost some of their water to reach balance with the environment. Two tests were carried out to determine which reason is responsible for the change of electrical properties of the specimens observed in this study. In test I, the masses of geopolymer specimens were measured over the whole testing period to monitor the loss of moisture in the specimen. In test II, the strength of the geopolymer specimen at different age was measured to determine whether geopolymerization is undergoing or finished over the testing period.

The result of test I is shown in Fig. 10. It can be seen that the masses of all specimens reduce with age, suggesting that they all lost water during the testing period. During the first 17 days, water evaporation from these specimens was very fast. After that, water loss was much slower. The mass loss of the geopolymer made of the fly ash from Orlando is almost negligible after the age of 51 days. The mass of the geopolymer made of the fly ash from Gaston even increases a little bit after 51 days, suggesting it may absorb some water from the environment. If water content is the major reason responsible for the electrical properties evolution of the geopolymers, the diameters of the high-frequency arcs of these two geopolymers should be the same or even smaller at the age of 384 days in comparison with that of the age of 108 days. However, experimental result (Figs. 8(b) and 8(c)) is on the opposite side. Therefore, unfinished geopolymerization should be the major reason for the increase of the diameters of the high-frequency arcs of these two geopolymers after age of 108 days. The geopolymer specimens made of the fly ashes from Miller and Martin Lake

continue losing moisture slowly from the age of 51 days to 383 days, which contributed to the increase of the diameters of the high-frequency arcs of these two geopolymers.

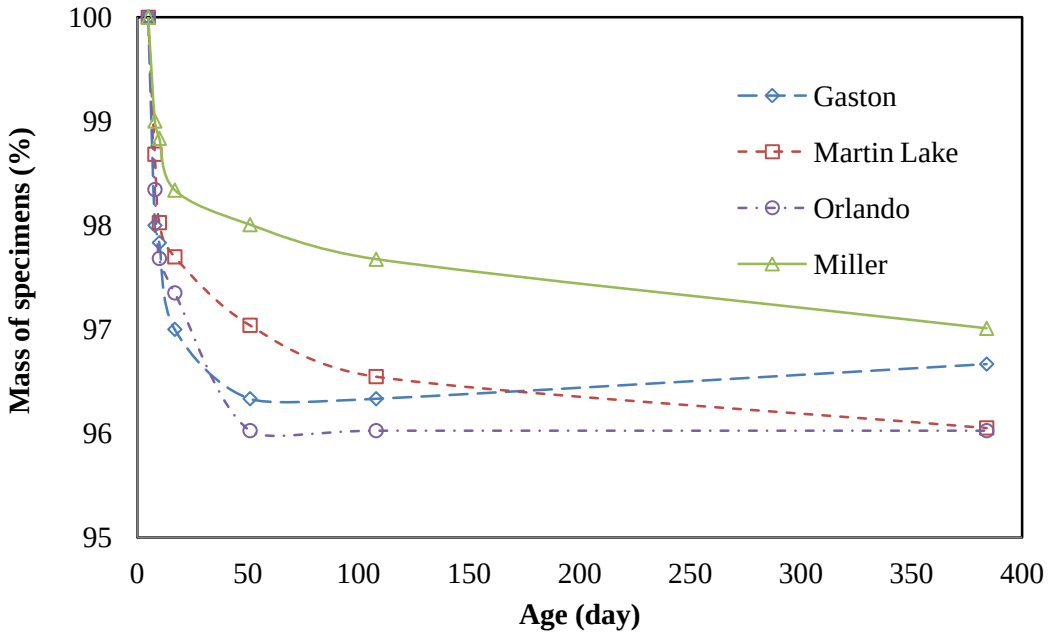

Fig. 10. Moisture Loss of Geopolymer Specimens with Age

The compressive strength of the geopolymer made of the fly ash from Gaston was measured at different age over 84 days. The result is shown in Fig. 11. It can be seen that the compressive strengths of this geopolymer increases with age in the testing period, suggesting that geopolymerization was not finished over this period. This is similar to the hydration of the Portland cement, which can take many years. In fly ash geopolymer specimens, geopolymerization can occur as long as aluminosilicate sources and alkaline activator are present. With new reaction products covering the fly ash particles, it becomes more difficult for the amorphous materials in the fly ash to diffuse through the reaction products and participate in the geopolymerization process. Although Fig. 11 only examines

the compressive strength of age up to 84 days, the geopolymerization of the fly ash did not stop after that as suggested by Figs.10 and 8.

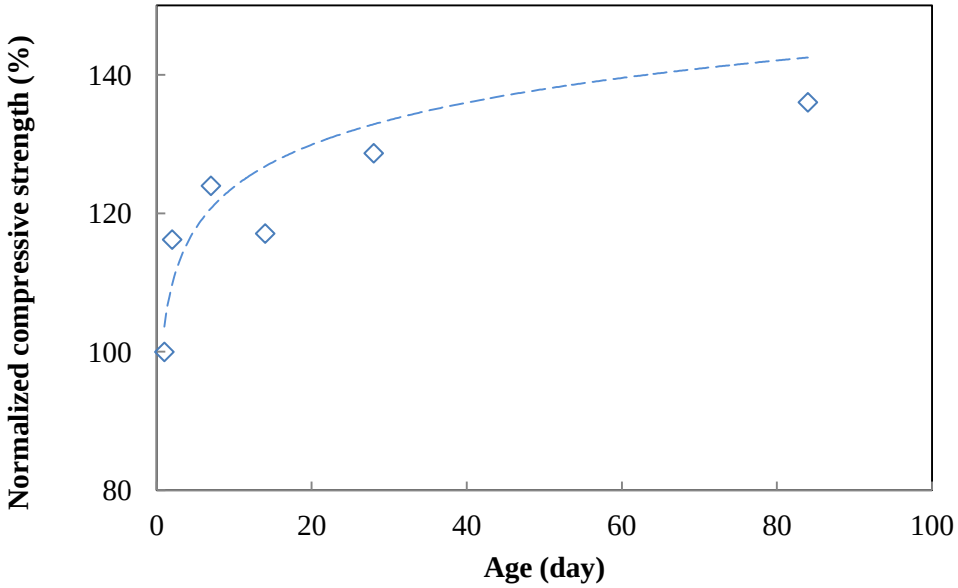

Fig. 11. Strength of Geopolymers Varying with Age

4. CONCLUSIONS

Electrical properties of geopolymers synthesized using four locally available fly ashes were studied by using both the fixed frequency and spectral measurements. The following conclusions can be drawn from this study.

1. Both the magnitude of the electrical impedance and the electrical resistance increase monotonously with the curing time, suggesting that they can be used as an indicator of the degree of geopolymerization.
2. The calcium content plays an important role in the electrical resistance evolution of the geopolymer during curing. The electrical resistance of the geopolymer with higher calcium content increases faster than that of the geopolymer with lower calcium content during the curing.

3. The bulk resistance or the diameters of the high frequency arcs of all geopolymers increase with age over one year, suggesting that the polymerization is a very long process, similar to the hydration process of Portland cement.
4. The bulk electrical resistance of the geopolymer depends on its chemical composition. Geopolymer with lower calcium content has a higher bulk electrical resistance at late age.
5. Electrical resistance or geopolymers at late age can be a few orders of magnitude higher than that at early age.

REFERENCES

Chindaprasirt, P., T. Chareerat, and V. Sirivivatnanon. 2007. "Workability and Strength of Coarse High Calcium Fly Ash Geopolymer." *Cement and Concrete Composites* 29 (3): 224–29.

Cui, Xue-Min, Guang-Jian Zheng, Yao-Cong Han, Feng Su, and Ji Zhou. 2008. "A Study on Electrical Conductivity of Chemosynthetic Al2O3–2SiO2 Geoploymer Materials." *Journal of Power Sources* 184 (2): 652–56.

Davidovits, Joseph. 2008. *Geopolymer Chemistry and Applications*. Geopolymer Institute.

Hanjitsuwan, Sakonwan, Prinya Chindaprasirt, and Kedsarin Pimraksa. 2011. "Electrical Conductivity and Dielectric Property of Fly Ash Geopolymer Pastes." *International Journal of Minerals, Metallurgy, and Materials* 18 (1): 94–99.

Hardjito, D., S. E Wallah, D. Sumajouw, and B. V. Rangan. 2004. "Factors Influencing the Compressive Strength of Fly Ash-Based Geopolymer Concrete." *Civil Engineering Dimension* 6 (2).

McCarter, W. J, T. M Chrisp, G Starrs, and J Blewett. 2003. "Characterization and Monitoring of Cement-Based Systems Using Intrinsic Electrical Property Measurements." *Cement and Concrete Research* 33 (2): 197–206.

McCarter, W. J., and R. Brousseau. 1990. "The A.C. Response of Hardened Cement Paste." *Cement and Concrete Research* 20 (6): 891–900.

Morsy, M. Saad. 1999. “Effect of Temperature on Electrical Conductivity of Blended Cement Pastes.” *Cement and Concrete Research* 29 (4): 603–6.

Schwarz, Nathan, Matthew DuBois, and Narayanan Neithalath. 2007. “Electrical Conductivity Based Characterization of Plain and Coarse Glass Powder Modified Cement Pastes.” *Cement and Concrete Composites* 29 (9): 656–66.

Tamás, Ferenc D. 1982. “Electrical Conductivity of Cement Pastes.” *Cement and Concrete Research* 12 (1): 115–20. doi:10.1016/0008-8846(82)90106-5.

Tamás, Ferenc D., E. Farkas, M. Vörös, and D.M. Roy. 1987. “Low-Frequency Electrical Conductivity of Cement, Clinker and Clinker Mineral Pastes.” *Cement and Concrete Research* 17 (2): 340–48.

Van Jaarsveld, J. G. S., J. S. J. Van Deventer, and L. Lorenzen. 1997. “The Potential Use of Geopolymeric Materials to Immobilise Toxic Metals: Part I. Theory and Applications.” *Minerals Engineering* 10 (7): 659–69. doi:10.1016/S0892-6875(97)00046-0.

SHEAR FORCE TRANSFER BETWEEN CARBON NANOTUBES AND MATRIX

ABSTRACT

This study explores the possibility to reinforce brittle matrix such as geopolymer with Carbon Nanotubes (CNTs). A model of stress transfer from CNTs to the matrix is critical to understand and optimize the reinforcing effect of CNTs. Existing studies are limited to axial force transfer between CNTs and the matrix. No solution is available for the shear force transfer. Aiming to fill the gap, this study proposes an analytical model of shear transfer between a CNT and its surrounding matrix using a simplified displacement field and the principle of minimum potential energy. Finite element analysis (FEA) has been also carried out to verify the model. Numerical results show that the present model reaches good agreement with FEA on the shear stress transfer and the deflection of the CNT induced by the applied shear force. An effective length exists for the CNT, within which the major shear stress transfer occurs. Parametric study also suggests that shear stress transfer is more efficient when the Young's modulus of the matrix is closer to that of the CNT.

1. INTRODUCTION

Geopolymers are amorphous three-dimensional alumino-silicate binder materials. Geopolymers are considered as "green materials" and strong candidates to replace Ordinary Portland Cement (OPC) in selected applications leading to more sustainable infrastructure system. However, two inherent drawbacks of geopolymers, brittleness and low tensile strength restrict their applications as structural materials in place of organic plastics and

metals. Compared with that of organic polymers, the toughness and strain at failure of geopolymers is 1000, and 65 times lower, respectively (Papakonstantinou et al., 2011). Due to high brittleness, their failures are catastrophic. These drawbacks have been shown in fiber-reinforced geopolymer composite. With very low strain capacity, geopolymer resins tend to crack at small load before tensile stress can be effectively transferred to fibers. When used to strengthen concrete beam, they rupture first, leading to premature failure of the strengthening.

To extend the applications of geopolymers, their tensile strength and toughness must be enhanced. One feasible approach to reach this goal is to reinforce and toughen geopolymers using carbon nanotubes. Carbon nanotubes (CNTs) are graphitic sheets seamlessly rolled into tubular structures, with diameters ranging from nanometer to tens of nanometers, and lengths up to centimeters. CNTs have extraordinary mechanical properties, such as strength (tensile strength > 100 GPa), stiffness (Young's modulus of ~ 1.5 TPa), flexibility (20%–30% at failure). All these features, together with high aspect ratios and excellent thermal and electrical properties, make CNT an ideal candidate to reinforce and toughen composite materials. Most of the existing studies on CNTs reinforcing and toughening focus on organic polymer based composites. Recently, CNTs, as well as carbon nanofibers (CNFs) have also been used to reinforce OPC (Shah et al., 2009).

The toughening effect of CNTs is mainly caused by the bridging effect of CNTs, as shown in Fig. 1(a). This bridging effect is dependent on the geometry and content of CNTs used. A model of stress transfer from CNTs to matrix is critical to understand and optimize this bridging behavior. A few existing models use shear lag model to study the stress transfer of CNTs subjected to an axial force, as shown in Fig. 1(c) (Haque and Ramasetty,

2005). No solution is available for the general loading condition shown in Fig. 1(a), in which the bridging CNT is subjected to an axial force, a shear forces, and a bending moment. To fill this gap, an analytical solution inspired by Sun (Sun 1994) has been developed for the stress transfer problem shown in Fig. 1(d). According to the principle of superposition, Fig. 1(b) can be obtained by superposing Fig. 1(c) and Fig. 1(d). Since a number of solutions are available in the literature on Fig. 1(c), this study focuses on Fig.1(d).

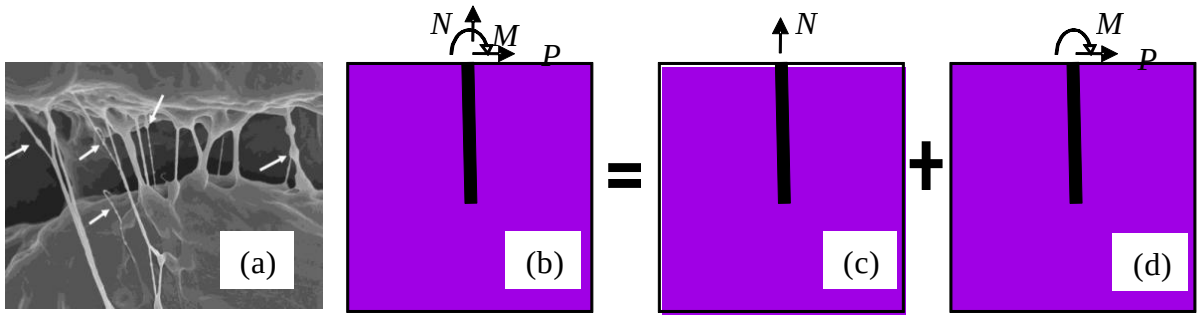

Fig. 1. Model of Stress Transfer from a CNT to Matrix: (a) CNTs Bridging; (b) Theoretical Model; (c) CNT Subjected to Axial Force; (d) CNT Subjected to Shear and Bending Moment in a Half Space.

2. ANALYTICAL MODEL

To model the load transfer of the CNT shown in Fig. 1(d), a cylinder with sufficient size is taken from the composite as shown in Fig. 2, in which a CNT is embedded in the matrix subjected to a shear force P_0 and a bending moment M_0. The length and the radius of the CNT are L and R, respectively. For the convenience of formulation, both the Cartesian and cylindrical coordinate systems are used in the following formulation. In this system, the CNT is molded as an Euler Bernoulli beam and the matrix is modeled as a 3D continuum body. The displacement field of the system shown in Fig. 2 is assumed as proposed by Sun (Sun 1994):

$$u(r,\theta,z) = y(z)\phi(r)\cos\theta, \tag{1}$$

$$v(r,\theta,z) = -y(z)\phi(r)\sin\theta, \tag{2}$$

$$w(r,\theta,z) = 0, \tag{3}$$

where, u, v, w are the displacement in r, θ and z direction, respectively. $y(z)$ has the dimension of length, while $\phi(r)$ is a dimensionless function representing the variation in r direction.

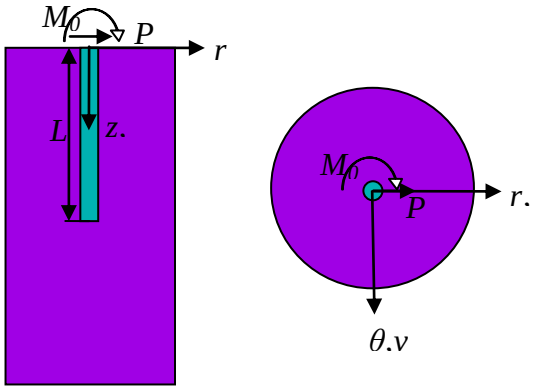

Fig. 2. A Laterally Loaded CNT in Matrix Model

Accordingly, thus the strain field can be written as

$$\begin{Bmatrix} \epsilon_{rr} \\ \epsilon_{\theta\theta} \\ \epsilon_{zz} \\ \gamma_{r\theta} \\ \gamma_{\theta z} \\ \gamma_{rz} \end{Bmatrix} = \begin{Bmatrix} y(z)\phi'(r)\cos\theta \\ 0 \\ 0 \\ -y(z)\phi'(r)\sin\theta \\ -y'(z)\phi(r)\sin\theta \\ y'(z)\phi(r)\cos\theta \end{Bmatrix}. \tag{4}$$

The stress field in the matrix is given by

$$\begin{Bmatrix} \sigma_{rr} \\ \sigma_{\theta\theta} \\ \sigma_{zz} \\ \sigma_{r\theta} \\ \sigma_{\theta z} \\ \sigma_{rz} \end{Bmatrix} = \begin{Bmatrix} (2G_s + \lambda_s)y(z)\phi'(r)\cos\theta \\ \lambda_s y(z)\phi'(r)\cos\theta \\ \lambda_s y(z)\phi'(r)\cos\theta \\ -G_s y(z)\phi'(r)\sin\theta \\ -G_s y'(z)\phi(r)\sin\theta \\ G_s y'(z)\phi(r)\cos\theta \end{Bmatrix}. \tag{5}$$

where G_s and λ_s are the shear modulus and the Lama constant of the matrix. The variation of the strain energy of the CNT-matrix system δU is calculated as

$$\delta U = E_p I_p \int_0^L \frac{\partial^2 y}{\partial z^2} \delta\left(\frac{\partial^2 y}{\partial z^2}\right) dz + \int_0^L \int_0^{2\pi} \int_R^{\infty} \sigma_{ij} \delta\epsilon_{ij} r dr d\theta dz + \int_L^{\infty} \int_0^{2\pi} \int_0^{\infty} \sigma_{ij} \delta\epsilon_{ij} r dr d\theta dz, \tag{6}$$

where E_p, I_p are the Young's modulus and moment inertial of the CNT, respectively. The variation of the strain energy in the CNT (first term on the right hand side of Eq.(6)) can be rewritten as

$$E_p I_p \int_0^L \frac{\partial^2 y}{\partial z^2} \delta\left(\frac{\partial^2 y}{\partial z^2}\right) dz = E_p I_p \left\{ \left[\frac{d^2 y}{dz^2} \delta\left(\frac{dy}{dz}\right) - \frac{d^3 y}{dz^3} \delta y \right]_0^L + \int_0^L \frac{d^4 y}{dz^4} \delta y dz \right\}. \tag{7}$$

Substituting Eqs. (4) and (5) into the part inside the integral of the second term on the right hand side of Eq. (6) yields

$$\sigma_{ij} \delta\epsilon_{ij} r = (2G_s + \lambda_s) y(z) \phi'(r) \cos\theta \, \delta[y(z)\phi'(r)\cos\theta] r - G_s y(z) \phi'(r) \sin\theta \, \delta[-y(z)\phi'(r) \sin\theta] r + G_s y'(z) \phi(r) \delta[y'(z)\phi(r)] r. \tag{8}$$

Integrating Eq. (8) over θ from 0 to 2π gives

$$\int_0^{2\pi} \sigma_{ij} \delta\epsilon_{ij} r \, d\theta = \pi(3G_s + \lambda_s) y(z) \phi'(r) r \delta[y(z)\phi'(r)] + 2\pi G_s y'(z) \phi(r) \delta[y'(z)\phi(r)] r. \tag{9}$$

By substituting Eqs. (4) and (5) into the second term on the right hand side of Eq. (6), we have

$$\int_0^L \int_0^{2\pi} \int_R^{\infty} \sigma_{ij} \delta\epsilon_{ij} r dr d\theta dz = \int_0^L \int_R^{\infty} \pi(3G_s + \lambda_s) y(z) \phi'(r) \delta[y(z)\phi'(r)] r dr dz \tag{10}$$

$$+\int_0^L \int_R^\infty 2\pi G_s y'(z)\phi(r)\delta[\mathrm{y'(z)\phi(r)}]rdrdz.$$

The first term on the right hand side of the above equation can be simplified as

$$\int_0^L \int_R^\infty \pi(3G_s + \lambda_s)y(z)\phi'(r)\delta[y(z)\phi'(r)]rdrdz$$
$$= \pi(\lambda_s + 3G_s)\int_0^\infty \int_R^\infty \left[\left(\frac{d\phi}{dr}\right)^2 y(z)\delta y + y(z)^2 \frac{d\phi}{dr}\delta\left(\frac{d\phi}{dr}\right)\right] r\, dr\, dz. \tag{11}$$

Considering

$$\int_R^\infty \left[\frac{d\phi}{dr}\delta\left(\frac{d\phi}{dr}\right)\right] r\, dr = \left[\frac{d\phi}{dr} r\delta\phi\right]_{R^+}^\infty - \int_R^\infty \left[\delta\phi\, \left(\frac{d^2\phi}{dr^2} r + \frac{d\phi}{dr}\right)\right] dr, \tag{12}$$

and letting

$$\int_R^\infty \phi^2 r\, dr = \xi_1 R^2, \int_R^\infty \left(\frac{d\phi}{dr}\right)^2 r\, dr = \eta_1, \int_0^L (\lambda_s + 3G_s)\, y(z)^2\, dz$$
$$= m_1, \int_0^L G_s\, \left(\frac{dy}{dz}\right)^2\, dz = n_1. \tag{13}$$

Equation (11) can be rewritten as

$$\int_0^L \int_R^\infty \pi(3G_s + \lambda_s)y(z)\phi'(r)\delta[y(z)\phi'(r)]rdrdz$$
$$= \pi(\lambda_s + 3G_s)\eta_1 \int_0^L y(z)\delta y dz + m_1\left\{\left(\frac{d\phi}{dr} r\delta\phi\right)_{R^+}^\infty - \int_R^\infty \left[\delta\phi\, \left(\frac{d^2\phi}{dr^2} r + \frac{d\phi}{dr}\right)\right] dr\right\}. \tag{14}$$

The second term on the right hand side of Eq. (10) can be simplified as

$$\int_0^L \int_R^\infty 2\pi G_s \phi(r)\frac{dy}{dz}\delta\left(\phi\frac{dy}{dz}\right) r\, dr\, dz$$
$$= 2G_s\xi_1 R^2 \left(\frac{dy}{dz}\delta y\right)_0^{L^-} - 2G_s\xi_1 R^2 \int_0^L \frac{d^2y}{dz^2}\delta y dz + 2n_1 \int_R^\infty \phi(r)\delta\phi\, r\, dr. \tag{15}$$

Thus Eq. (10) becomes

$$\int_0^L \int_0^{2\pi} \int_R^\infty \sigma_{ij}\delta\epsilon_{ij} r dr d\theta dz = \pi(\lambda_s + 3G_s)\eta_1 \int_0^L y(z)\delta y dz$$

$$+m_1\left\{\left(\frac{d\phi}{dr} r\delta\phi\right)_{R^+}^{\infty} - \int_R^\infty \left[\delta\phi\left(\frac{d^2\phi}{dr^2} r + \frac{d\phi}{dr}\right)\right] dr\right\} \tag{16}$$

$$+2G_s\xi_1 R^2\left(\frac{dy}{dz}\delta y\right)_0^{L^-} - 2G_s\xi_1 R^2 \int_0^L \frac{d^2y}{dz^2}\delta y dz + 2n_1 \int_R^\infty \phi(r)\delta\phi\, r\, dr.$$

Letting

$$\int_0^\infty \phi^2 r\, dr = \xi_2 R^2, \int_0^\infty \left(\frac{d\phi}{dr}\right)^2 r\, dr = \eta_2, \int_L^\infty (\lambda_s + 3G_s)\, y(z)^2\, dz$$

$$= m_2, \int_L^\infty G_s \left(\frac{dy}{dz}\right)^2 dz = n_2, \tag{17}$$

the third term on the right hand side of Eq. (6) becomes

$$\int_L^\infty \int_0^{2\pi} \int_0^\infty \sigma_{ij}\delta\epsilon_{ij} r dr d\theta dz = \pi(\lambda_s + 3G_s)\eta_2 \int_L^\infty y(z)\delta y dz$$

$$+m_2\left\{\left(\frac{d\phi}{dr} r\delta\phi\right)_{R^+}^{\infty} - \int_R^\infty \left[\delta\phi\left(\frac{d^2\phi}{dr^2} r + \frac{d\phi}{dr}\right)\right] dr\right\} + 2G_s\xi_2 R^2\left(\frac{dy}{dz}\delta y\right)_{L^+}^{\infty}$$

$$-2G_s\xi_2 R^2 \int_L^\infty \frac{d^2y}{dz^2}\delta y dz + 2n_2 \int_R^\infty \phi(r)\delta\phi\, r\, dr \tag{18}$$

$$+m_2\left\{\left(\frac{d\phi}{dr} r\delta\phi\right)_0^{R^-} - \int_0^R \left[\delta\phi\left(\frac{d^2\phi}{dr^2} r + \frac{d\phi}{dr}\right)\right] dr\right\} + 2n_2 \int_0^R \phi(r)\delta\phi\, r\, dr.$$

It is reasonable to assume that $\phi(r) \equiv 1$ $(r \le R)$ within the CNT. Then

$$\int_0^\infty \phi^2 r\, dr = \int_0^R \phi^2 r\, dr + \int_R^\infty \phi^2 r\, dr = \frac{R^2}{2} + \xi_1 R^2. \tag{19}$$

Therefore

$$\xi_2 = \xi_1 + \frac{1}{2}. \tag{20}$$

Similarly,

$$\int_0^\infty \left(\frac{d\phi}{dr}\right)^2 r\, dr = \int_0^R \left(\frac{d\phi}{dr}\right)^2 r\, dr + \int_R^\infty \left(\frac{d\phi}{dr}\right)^2 r\, dr = \eta_1 R^2. \tag{21}$$

Thus

$$\eta_2 = \eta_1. \tag{22}$$

Then Eq. (18) can be rewritten as

$$\begin{aligned}\int_L^\infty \int_0^{2\pi} \int_0^\infty \sigma_{ij}\delta\epsilon_{ij} r dr d\theta dz &= \pi(\lambda_s + 3G_s)\eta_2 \int_L^\infty y(z)\delta y dz \\ &+ m_2\left\{\left(\frac{d\phi}{dr} r\delta\phi\right)_{R^+}^\infty - \int_R^\infty \left[\delta\phi\left(\frac{d^2\phi}{dr^2} r + \frac{d\phi}{dr}\right)\right] dr\right\} \\ +2G_s\xi_2 R^2\left(\frac{dy}{dz}\delta y\right)_{L^+}^\infty &- 2G_s\xi_2 R^2 \int_L^\infty \frac{d^2y}{dz^2}\delta y dz + 2n_2 \int_R^\infty \phi(r)\delta\phi\, r\, dr.\end{aligned} \tag{23}$$

Equation (6) becomes

$$\begin{aligned}\delta U = E_p I_p &\left\{\left[\frac{d^2y}{dz^2}\delta\left(\frac{dy}{dz}\right) - \frac{d^3y}{dz^3}\delta y\right]_0^{L^-} + \int_0^L \frac{d^4y}{dz^4}\delta y dz\right\} \\ +\pi(\lambda_s + 3G_s)\eta_1 &\int_0^L y(z)\delta y dz + m_1\left\{\left(\frac{d\phi}{dr} r\delta\phi\right)_R^\infty - \int_R^\infty \left[\delta\phi\left(\frac{d^2\phi}{dr^2} r + \frac{d\phi}{dr}\right)\right] dr\right\} \\ +2G_s\xi_1 R^2\left(\frac{dy}{dz}\delta y\right)_0^{L^-} &- 2G_s\xi_1 R^2 \int_0^L \frac{d^2y}{dz^2}\delta y dz + 2n_1 \int_R^\infty \phi(r)\delta\phi\, r\, dr \\ +\pi(\lambda_s + 3G_s)\eta_2 &\int_L^\infty y(z)\delta y dz + m_2\left\{\left(\frac{d\phi}{dr} r\delta\phi\right)_{R^+}^\infty - \int_R^\infty \left[\delta\phi\left(\frac{d^2\phi}{dr^2} r + \frac{d\phi}{dr}\right)\right] dr\right\} \\ +2G_s\xi_2 R^2\left(\frac{dy}{dz}\delta y\right)_{L^+}^\infty &- 2G_s\xi_2 R^2 \int_L^\infty \frac{d^2y}{dz^2}\delta y dz + 2n_2 \int_R^\infty \phi(r)\delta\phi\, r\, dr.\end{aligned} \tag{24}$$

Letting $t_1 = \frac{\pi\xi_1 R^2 G_s}{E_p I_p}, t_2 = \frac{\pi\xi_2 R^2 G_s}{E_p I_p}, k = \frac{\pi\eta_1(\lambda_s+3G_s)}{E_p I_p}$, Eq. (24) can be simplified as

$$\begin{aligned}\delta U = E_p I_p \int_0^L \left[\frac{d^4y}{dz^4} - 2t_1\frac{d^2y}{dz^2} + ky(z)\right]\delta y dz + E_p I_p \int_L^\infty \left[ky(z) - 2t_2\frac{d^2y}{dz^2}\right]\delta y dz \\ + \int_R^\infty \left[2(n_1+n_2)r\phi(r) - (m_1+m_2)\left(\frac{d^2\phi}{dr^2}r + \frac{d\phi}{dr}\right)\right]\delta\phi dr \\ + E_p I_p \left[\frac{d^2y}{dz^2}\delta\left(\frac{dy}{dz}\right) - \frac{d^3y}{dz^3}\delta y + 2t_1\frac{dy}{dz}\delta y\right]_0^{L^-} + 2t_2 E_p I_p \left(\frac{dy}{dz}\delta y\right)_{L^+}^\infty \\ + (m_1+m_2)\left(\frac{d\phi}{dr}r\delta\phi\right)_{R^+}^\infty .\end{aligned} \tag{25}$$

The work done by external loads is given by

$$\delta W = -\left[P_0\delta y + M_0\delta\left(\frac{dy}{dz}\right)\right]_{z=0}. \tag{26}$$

By triggering principle of minimum potential energy

$$\delta U + \delta W = 0, \tag{27}$$

we obtain the governing equation of the CNT-matrix system

$$\frac{d^4y}{dz^4} - 2t_1\frac{d^2y}{dz^2} + ky(z) = 0 (0 \le z < L), \tag{28}$$

$$2t_2\frac{d^2y}{dz^2} - ky(z) = 0 (L \le z < \infty), \tag{29}$$

$$\frac{d^2\phi}{dr^2}r + \frac{d\phi}{dr} - \frac{2(n_1+n_2)}{m_1+m_2}r\phi(r) = 0 (R \le r < \infty), \tag{30}$$

and boundary conditions as

$$\left(\frac{P_0}{E_p I_p} - \frac{d^3y}{dz^3} + 2t_1\frac{dy}{dz}\right)\delta y + \left(\frac{d^2y}{dz^2} + \frac{M_0}{E_p I_p}\right)\delta\left(\frac{dy}{dz}\right) = 0 \ (z = 0), \tag{31}$$

$$\frac{d^2y}{dz^2}\delta\left(\frac{dy}{dz}\right)\Big|_{z=L^-} + \left[\left(-\frac{d^3y}{dz^3} + 2t_1\frac{dy}{dz}\right)_{z=L^-} - 2t_2\frac{dy}{dz}\Big|_{z=L^+}\right]\delta y = 0, \tag{32}$$

$$\frac{dy}{dz}\delta y = 0(z \to \infty), \tag{33}$$

$$\frac{d\phi}{dr}\delta\phi = 0(r = R), \tag{34}$$

$$\frac{d\phi}{dr}r\delta\phi = 0(r \to \infty). \tag{35}$$

Letting

$$\frac{2(n_1 + n_2)}{m_1 + m_2} = \left(\frac{\gamma}{R}\right)^2, \tag{36}$$

the solution to Eq.(30) can be obtained as

$$\phi(r) = \frac{K_0\left(\frac{\gamma r}{R}\right)}{K_0(\gamma)}. \tag{37}$$

where K_0 denotes the modified Bessel function of the second kind of order zero. Thus,

$$\xi_1 = \frac{[K_1(\gamma)]^2 - [K_0(\gamma)]^2}{2[K_0(\gamma)]^2}, \eta_1 = \frac{[K_1(\gamma) + \gamma K_0(\gamma)]^2 - (\gamma^2 + 1)[K_0(\gamma)]^2}{2[K_0(\gamma)]^2}. \tag{38}$$

The solution to Ea. (29) is given by

$$y(z) = y(L)e^{-\sqrt{\frac{k}{2t_2}}(z-L)}, \tag{39}$$

in which the boundary condition $y = 0$ $(z \to \infty)$ is already applied. Then

$$\frac{dy}{dz}\Big|_{z=L^+} = -\sqrt{\frac{k}{2t_2}}y(L), \tag{40}$$

$$m_2 = (\lambda_s + 3G_s)\sqrt{\frac{t_2}{2k}}\,[y(L)]^2, \tag{41}$$

$$n_2 = \frac{G_s}{2}\sqrt{\frac{k}{2t_2}}\,[y(L)]^2. \tag{42}$$

3. SOLUTION AND NUMERICAL EXAMPLES

An iteration process is used to solve the governing equations derived in the above section (See Appendix B for the program files written in Mathematica 5.0):

1. Guess an initial γ, denoting as γ_0.
2. Calculate parameters $\xi_i, \eta_i, t_i\ (i = 1, 2), k$ using γ_0.
3. Solve Eq. (28) with boundary conditions given by Eqs .(31) and (32).
4. Calculate m_i and $n_i\ (i = 1, 2)$ using the $y(z)$ obtained in step 3.
5. Recalculate γ.
6. Check if γ against γ_0 to see if they converge. If they converge, the calculation ends. If not, assign γ to γ_0 and repeat step 1~6.

To verify the proposed model, a numerical example has been carried out and compared with finite element analysis (FEA) result. The material properties used in this example are $G_s = 0.893$ GPa, $\lambda_s = 2.08$ GPa, $E_p = 1$ TPa, $R = 0.471$ nm, $L = 50R$, The applied loads are $P_0 = 1 \times 10^{-4} \times E_p \times \pi \times R^2, M_0 = 0$.

FEA was conducted with the commercial software ANSYS 13.0 (See Appendix A for the batch file). Three dimensional 8-node solid element SOLID185 was used in the analysis. Since half-space could not be exactly simulated in FEA, a finite volume was chosen in FEA with the outer radius of the matrix $r_m = 50\,R$, and the depth of the matrix $L_m = 10L$, as

shown if Fig. 3. Only a quarter of the system was molded by (Fig. 3) by applying the boundary conditions as fellows. Symmetric conditions are enforced on the plane of $\theta = 0$, and asymmetric conditions are enforced on the plane of $\theta = \frac{\pi}{2}$. Displacements are assumed zero on the outer perimeter $r = R_m$ where real displacements approach zero. On the very bottom plane of $z = L_m$, displacement in z direction is assumed zero too.

Numerical results are shown in Figs. 4 and 5. From Eq. (5) we can see that, along the perimeter of the CNT, stress changes with $\sin\theta$ or $\cos\theta$. All stresses shown in this numerical example are their amplitudes which are defined as the maximum stress along the perimeter of the CNT. Stresses $\sigma_{rr}, \sigma_{\theta\theta}, \sigma_{zz}$ and τ_{rz} reach their amplitudes at $\theta = 0°$; while $\sigma_{r\theta}$ and $\sigma_{\theta z}$ equal their amplitude at $\theta = 90°$. All stresses are normalized by $\sigma_0 = \frac{P_0}{\pi R^2}$.

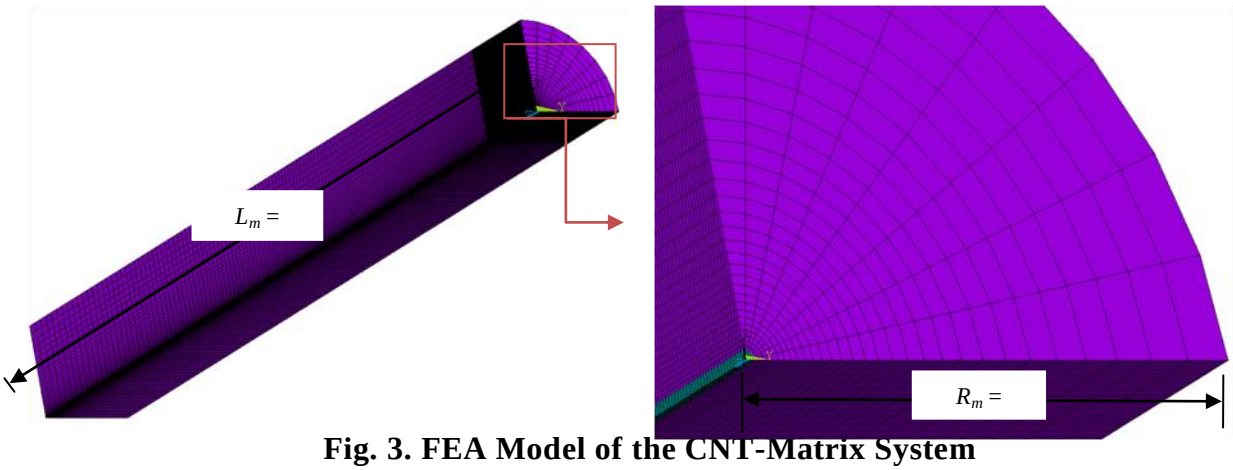

Fig. 3. FEA Model of the CNT-Matrix System

Figure 4 shows the stress distribution along the interface between the CNT and the matrix. Figure 4(a) shows that σ_{rr} concentrates at a small segment at the top, suggesting that lateral force transfer mainly occurs in this area. Therefore, longer CNT is not helpful in shear force transfer. Overall, good agreement has been achieved between the present method and the FEA. The present method seems to over-predict the concentration of σ_{rr} due to the

simplification of the displacement field. FEA result shows a slight concentration of $\sigma_{\theta\theta}$ exists at the top of the CNT (Fig. 4(b)), which is exaggerated by the present model. Figure 4(c) shows that severe concentration of σ_{zz} occurs near the top and reduces to zero quickly at the top of the CNT according to FEA. This strong stress concentration of σ_{zz} in the CNT is resulted from the large curvature of the CNTs at this location caused by the applied shear force P_0. In the present model, displacement in *z* direction is ignored and the other two displacements are assumed uniform in the *r*-direction, leading to underestimating this stress concentration. Figure 4(d) shows that present model reaches excellent agreement with the FEA on $\tau_{r\theta}$ since this stress is not dependent on the displacement in *z* direction. Figure 4(e) shows that shear stress $\tau_{\theta z}$ generated by the transverse shear force applied at the top of the CNT is very small. Figure 4(f) reveals a moderate concentration of τ_{rz} existing at the top of the CNT.

Figure 4 shows that the present model agrees with FEA very well on σ_{rr} and $\tau_{r\theta}$ and deviates from the FEA for other stresses. This is not surprising since the displacement in the *z* direction is not considered in the model (Eq. 3). Because the shear force is only transferred between the CNT and the matrix through $\sigma_{rr.}$, the present model which can predict σ_{rr} correctly provides a useful tool to study the load transfer mechanism between the CNT and the matrix.

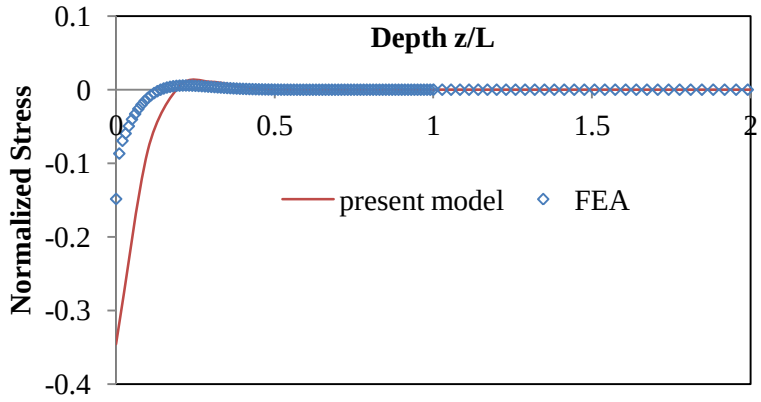
Depth z/L
Normalized Stress
0.1
0
-0.1
-0.2
-0.3
-0.4
0
0.5
1
1.5
2
present model
FEA

(a)

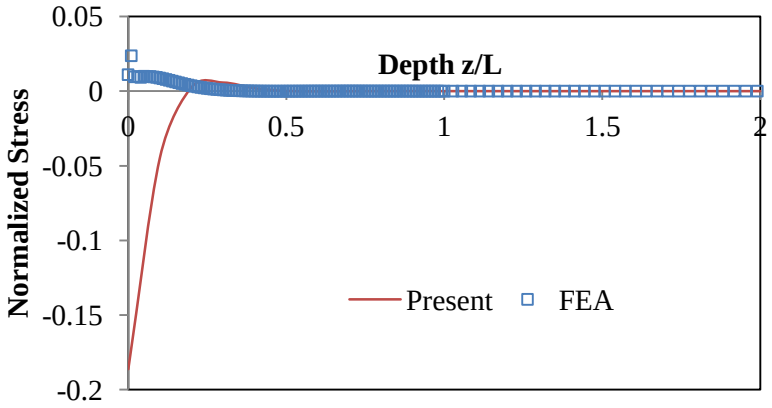
Depth z/L
Normalized Stress
0.05
0
-0.05
-0.1
-0.15
-0.2
0
0.5
1
1.5
2
Present
FEA

(b)

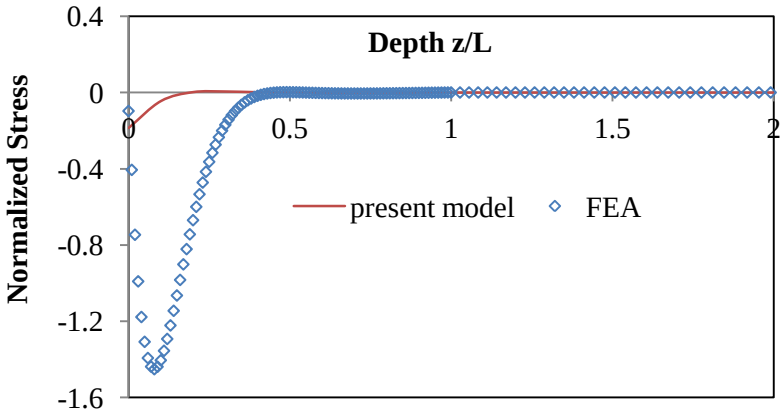
Depth z/L
Normalized Stress
0.4
0
-0.4
-0.8
-1.2
-1.6
0
0.5
1
1.5
2
present model
FEA

(c)

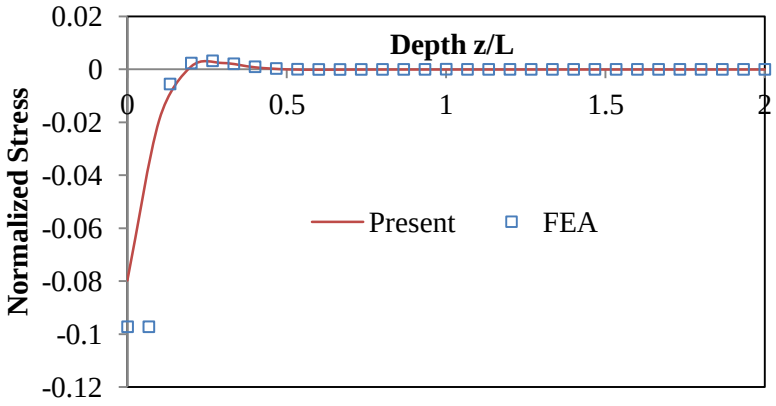

(d)

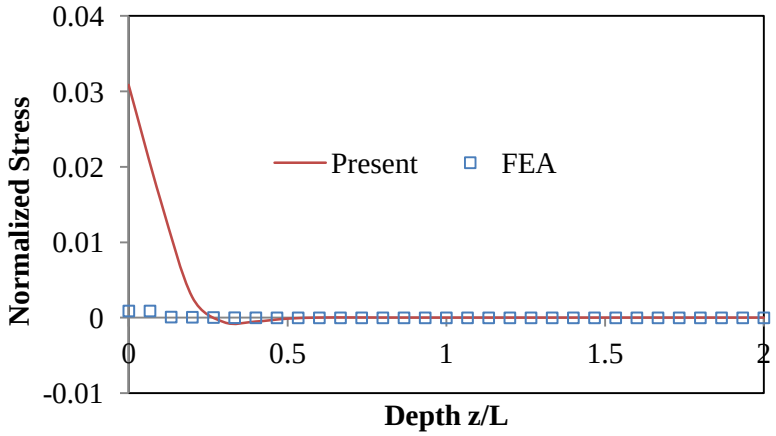

(e)

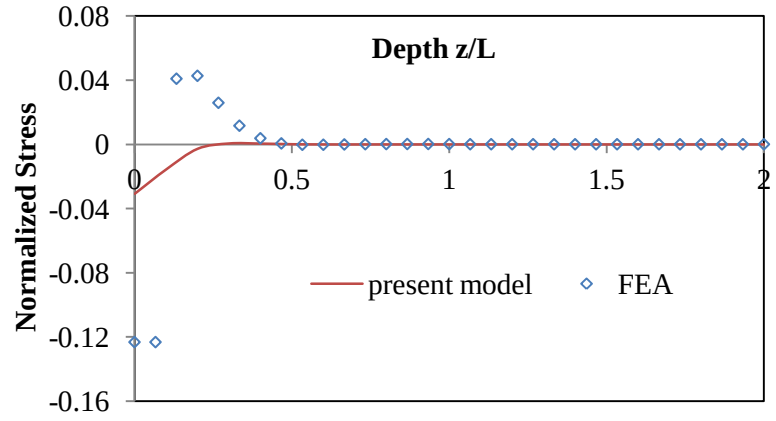

(f)

Fig. 4. Stress Distribution along the CNT ($r = R$): (a) σ_{rr}; (b) $\sigma_{\theta\theta}$; (c) σ_{zz}; (d) $\tau_{r\theta}$; (e) $\tau_{\theta z}$; (f) τ_{rz}

Figure 5 shows the stress distribution within the matrix on the top surface ($z = 0$). As shown in Fig.5(a), σ_{rr} concentrates near the CNT and reduces sharply with the distance from the CNT, suggesting that shear force transfer only affects a small area of the matrix within a distance less than $r/R_0 < 10$. Out of this area, the stress in the matrix induced by the applied shear force P_0 is negligible. Once again, good agreement has been achieved between the present method and the FEA. FEA result shows that $\sigma_{\theta\theta}$ in the matrix is negligible (Fig. 5(b)). Figure 5(c) shows that both FEA and the present model predict that σ_{zz} concentrates near the CNT and reduces quickly to almost negligible within $r/R_0 < 10$. In Fig. 5(d), the present model reaches excellent agreement with the FEA on the distribution of $\tau_{r\theta}$ in the matrix. Similar to the case shown in Fig. 4, the present model fails to reach good agreement with FEA on the shear stress $\tau_{\theta z}$ and τ_{rz} in the matrix due to ignoring the vertical displacement w.

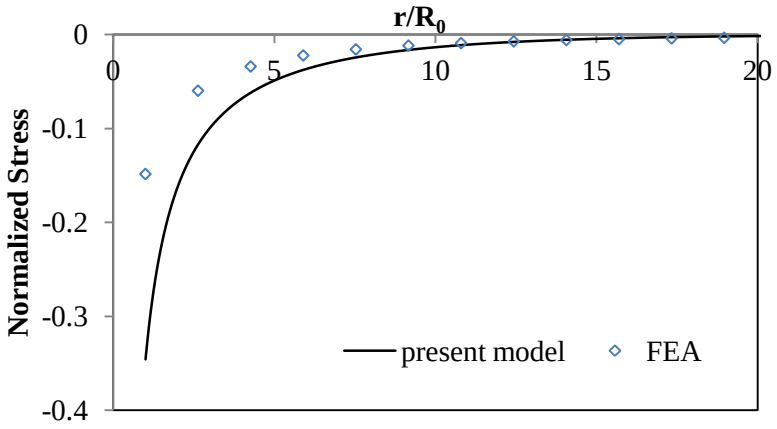

(a)

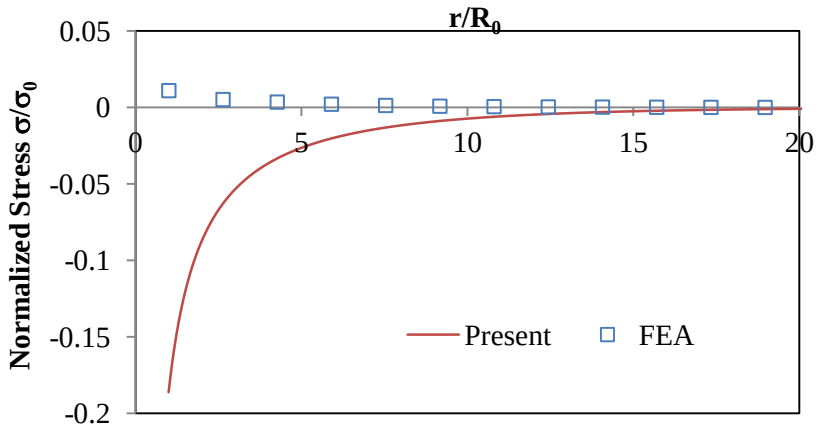
r/R0
0.05
0
-0.05
-0.1
-0.15
-0.2
0
5
10
15
20
Normalized Stress σ/σ0
Present
FEA

(b)

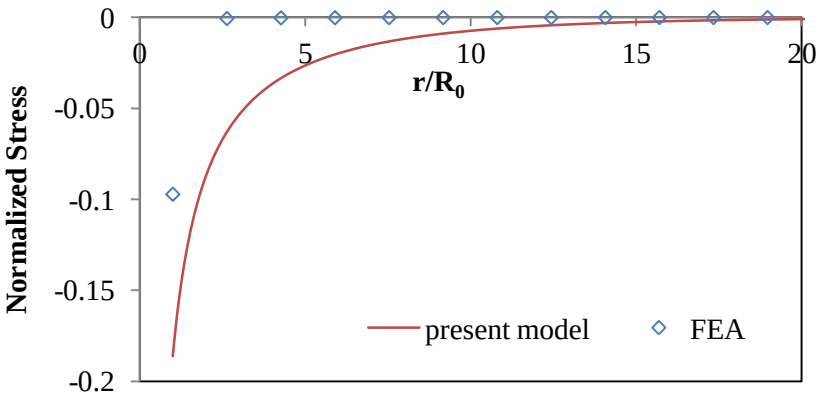
0
-0.05
-0.1
-0.15
-0.2
0
5
10
15
20
r/R0
Normalized Stress
present model
FEA

(c)

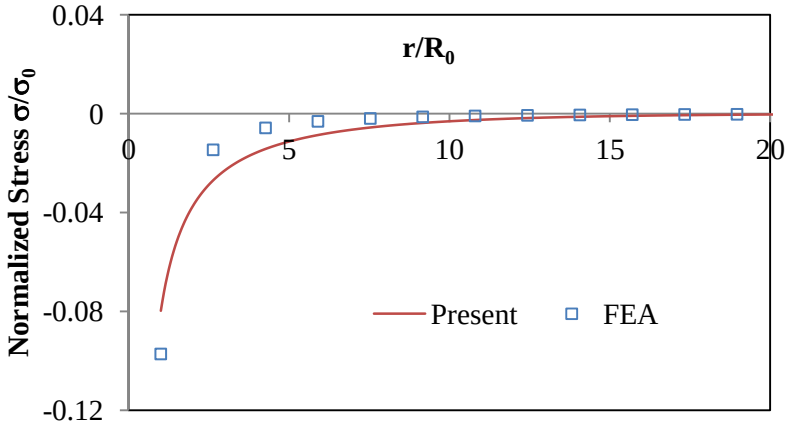
0.04
0
-0.04
-0.08
-0.12
0
5
10
15
20
r/R0
Normalized Stress σ/σ0
Present
FEA

(d)

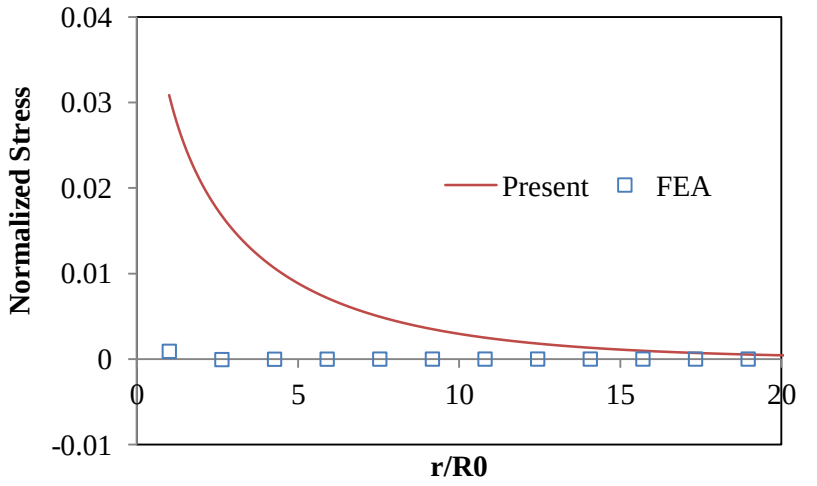

(e)

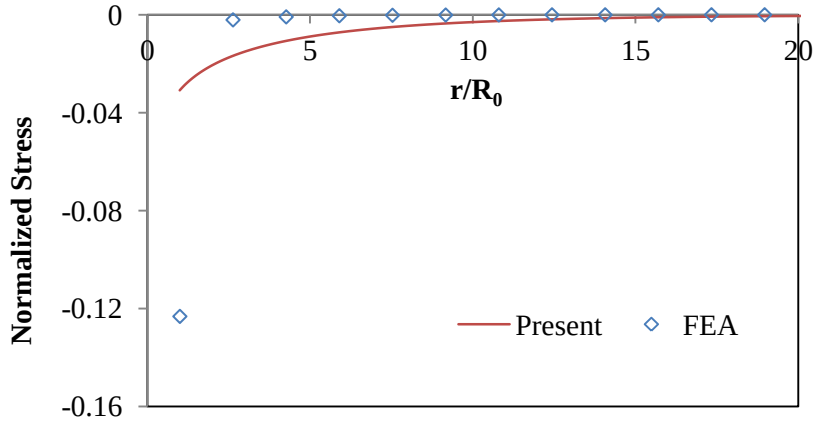

(f)

Fig. 5. Stress Distribution in Matrix (z=0): (a) σ_{rr}; (b) $\sigma_{\theta\theta}$; (c) σ_{zz}; (d) $\tau_{r\theta}$; (e) $\tau_{\theta z}$; (f) τ_{rz}

Lateral deflection of the CNT induced by the transverse shear force P_0 at r = 0 is shown in Fig. 6. In this figure, the deflection is normalized with $y_0 = \frac{P_0 L^3}{3E_p I_p}$, which is the deflection of the tip of a cantilevered beam under the transverse load of P_0 at the tip. It can be seen that excellent agreement with FEA has been achieved by the present model. Both calculations show that the lateral deflection is developed and limited to the upper half of the CNT. Such a lateral displacement can induce large curvature in the CNT, which produces a high

bending moment concentration in this region, as shown in Fig. 7. This bending moment could cause the buckling of the CNT and therefore, leading to a larger lateral deflection of the CNT. From Figures 4(a), 4(d), 6 and 7, we can see that there exists an effective length of the CNT within which the shear stress transfer occurs. No or little shear force transfer occurs in the part of CNT out of this effective length.

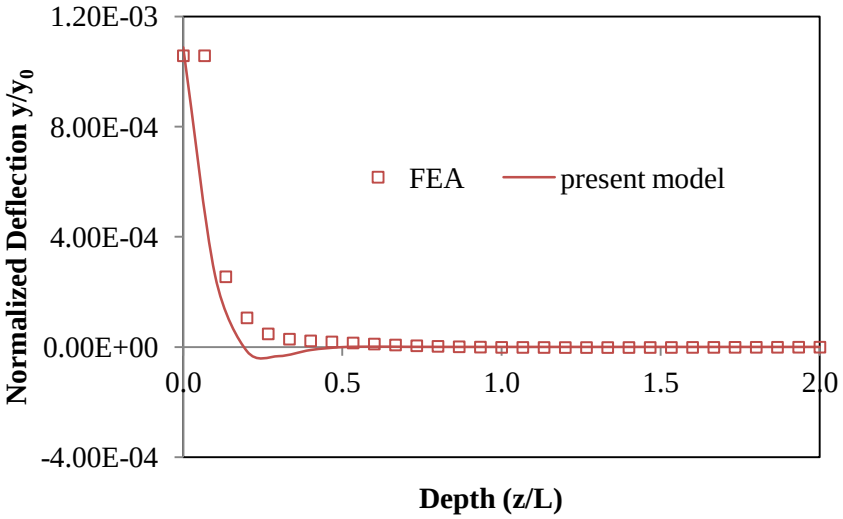

Fig. 6. Deflection at $r = 0$

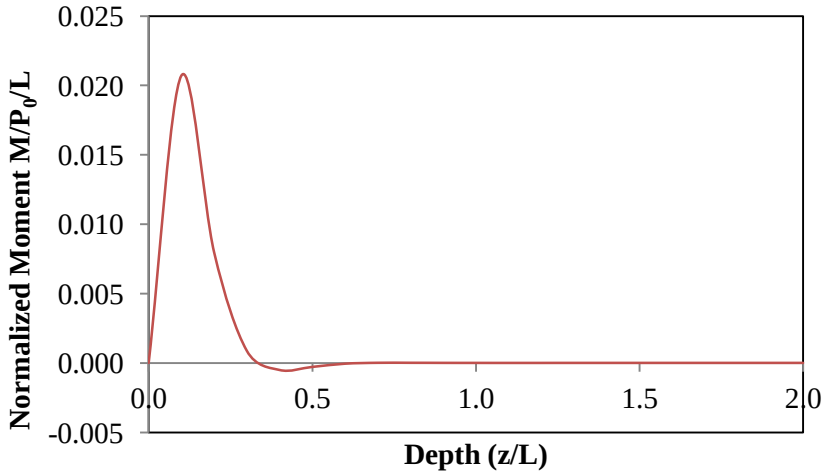

Fig. 7. Moment Distribution along the CNT

Figures 8 and 9 examine the effect of the Young's modulus of the matrix on stress transfer when the CNT is subjected to a transverse force applied at the top. In these figures, the modulus of the CNT is the same as before. The Young's modulus of matrix is changed so that the range of E_s/E_r is between 20 and 800. Within such a range, most commonly used structural materials from epoxy to concrete can be covered. Figure 8 shows the distribution of σ_{rr} within the matrix on the top surface (z = 0). It can be seen that all σ_{rr} concentrate in a small zone near the CNT as revealed in Fig. 5. The effect of the modulus of the matrix on σ_{rr} is clearly shown in this figure. σ_{rr} increases with the Young's modulus of the matrix. This implies that the shear force can be transferred more efficiently if the mismatch of the Young's modulus of the matrix and the CNT is smaller. Similar feature can be observed on the σ_{rr} distribution along the surface of the CNT, as shown in Fig. 9. Figure 9 also shows that the stress transfer region does not change with the Young's modulus of the matrix, which confirms that an effective length of the CNT exist for shear stress transfer.

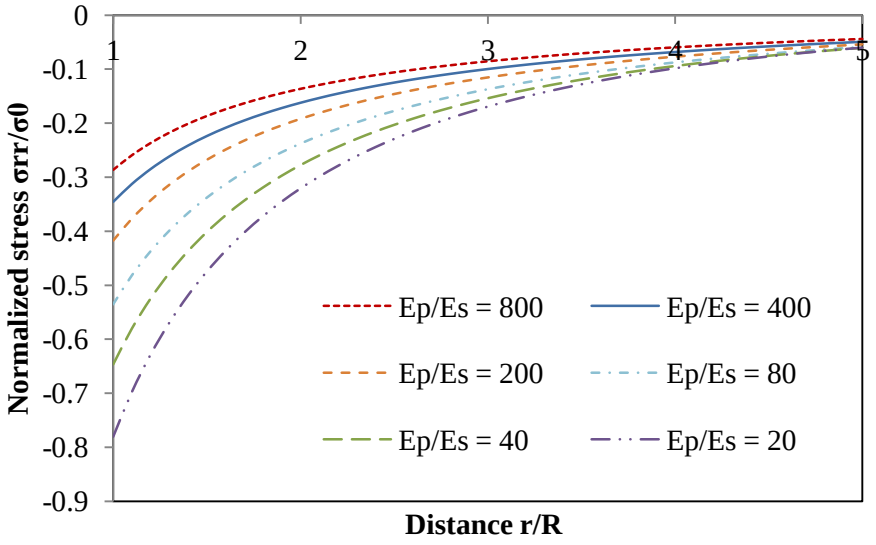

Fig. 8. Effect of E_s on σ_{rr} Distribution within the Matrix

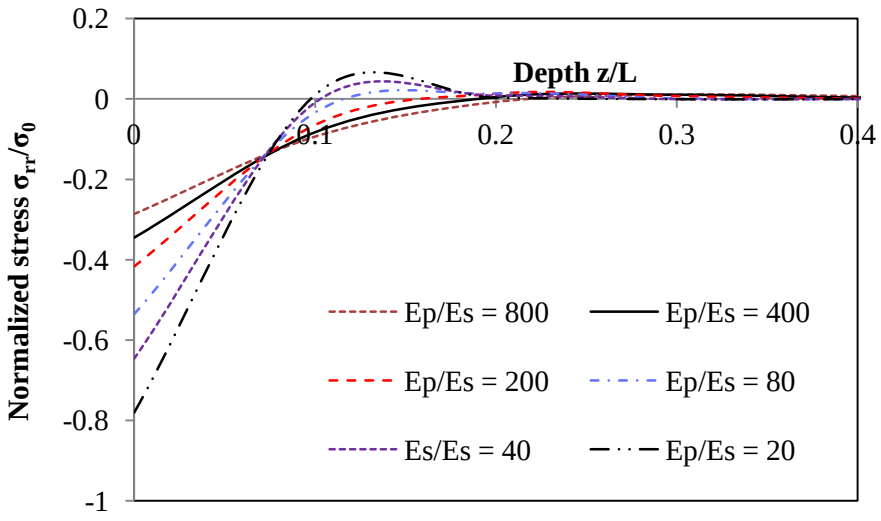

Fig. 9. Effect of *Es* on σ_{rr} Distribution along the CNT

4. CONCLUSIONS

This study proposes an analytical model of shear force transfer between a CNT and its surrounding matrix using a simplified displacement field and the principle of minimum potential energy. Finite element analysis (FEA) has been also carried out to verify the model. A few conclusions can be drawn from this study.

1) The present model agrees very well with FEA on the later stress distribution along the CNT and within the matrix, and deflection of the CNT, suggesting that the present model can be used to study the shear for transfer in CNTs reinforced nanocomposite.
2) There exists an effective length of the CNT within which the shear stress transfer occurs. No or little shear force transfer occurs out of this effective length.
3) Shear stress transfer is more efficient when the Young's modulus of the matrix is closer to that of the CNT.

REFERENCES

Haque, A., and A. Ramasetty. 2005. “Theoretical Study of Stress Transfer in Carbon Nanotube Reinforced Polymer Matrix Composites.” *Composite Structures* 71 (1): 68–77.

Papakonstantinou, Ch, and P. Balaguru. 2006. “Bond Characteristics And Structural Behavior of Inorganic Polymer FRP.” In *Measuring, Monitoring and Modeling Concrete Properties*, edited by MARIA S. KONSTA-GDOUTOS, 735–41. Springer Netherlands
.

Shah, S. P., M. S. Konsta-Gdoutos, Z. S. Metaxa, and P. Mondal. 2009. “Nanoscale Modification of Cementitious Materials.” In *Nanotechnology in Construction 3*, edited by Zdeněk Bittnar, Peter J. M. Bartos, Jiří Němeček, Vít Šmilauer, and Jan Zeman, 125–30. Springer Berlin Heidelberg.

Sun, Keming. 1994. “A Numerical Method for Laterally Loaded Piles.” *Computers and Geotechnics* 16 (4): 263–89.

Zhou, Li-Jun, Yi-Lan Kang, and Jian-Gang Guo. 2011. “Phenomenological Model of Interfacial Stress Transfer in Carbon Nanotube Reinforced Composites with van Der Waals Effects.” *Polymer Composites* 32 (7): 1069–76.

Appendix A

Ansys (version 13.0) batch file for FEA:

```
/clear
  !/UNITS, MPA
  !LEN -- millimeters
  !MASS -- Tonne
  !FORCE -- Newton
  !
  !/UNITS, uMKS
  !LEN -- micro-meter
  !MASS -- Kg
  !FORCE -- micro-Newton
  !Pressure -- MPa
  !
  /UNITS, USER, 1E-9,,,,,,1E-9
  /PREP7

  !R0=.76/2 !inner radius
  R0=0.471 !outer radius in nanometer
  LOR=50 !L/R
  L=LOR*R0 ! length of the fiber
  RR=LOR*R0 !outer radius
  LL=10*L !bottom

  EP=1E6 !in MPa
  NUP=.3

  ES=2.41E3 !in MPa
  NUS=0.35

  /PNUM,KP,0
  /PNUM,LINE,0
  /PNUM,AREA,0
  /PNUM,VOLU,1
  /PNUM,NODE,0
  /PNUM,TABN,0
  /PNUM,SVAL,0
```

```
/NUMBER,1
/PNUM,MAT,1

ET,1, PLANE182
KEYOPT, 1, 1, 2 !reduced integration as per ANSYS
sugguests
ET,2, SOLID185
KEYOPT, 2, 2, 3 !as per ANSYS sugguests

!Pile
MPTEMP,1,0
MPDATA, EX, 1, , EP
MPDATA, PRXY, 1, ,NUP

!Soil
MPTEMP,1,0
MPDATA, EX, 2, , ES
MPDATA, PRXY, 2,,NUS

CYL4, 0, 0, R0, 0, RR, 90
CYL4, 0, 0, 0, 0, R0, 90
KSEL,ALL
NUMMRG, KP, R0/1E5

ASEL, S, AREA,,1
AATT, 2,,,  !AATT, MAT, REAL, TYPE, ESYS, SECN
!
ASEL, S, AREA,,2
AATT, 1,,,  !AATT, MAT, REAL, TYPE, ESYS, SECN

FINE=R0
ASEL, S, AREA,, 2
MSHKEY, 2
MSHAPE, 0, 2D
ESIZE, R0/5, 20
AMESH, 2

LESIZE, 2, ,,30, 1/10
LESIZE, 4, ,,30, 1/10
```

```
ASEL, S, AREA, , 1
!MSHKEY, 1
MSHAPE, 0, 2D
ESIZE, FINE, 20
AMESH, 1

ASEL, S, AREA,, 2
MSHKEY, 2
MSHAPE, 0, 2D
AMESH, 2

NUMMRG, ALL, FINE/1E5

TYPE, 2
ESIZE, R0, 30

TYPE, 2
MAT, 1 !pile
EXTOPT, ESIZE, 2*LOR
ASEL, ALL
VOFFST, 2,L

MAT, 2 !soil
VOFFST, 1,L

EXTOPT, ESIZE, 3* LOR, 4
VOFFST, 3,LL - L !the opposite area of #2
VOFFST, 7,LL - L !the opposite area of #1

NUMMRG, ALL, FINE/1E5
FINISH

/SOLU
DSPOPTION,,INCORE,,,,performance
BCSOPTION,,INCORE,,,,performance
P0=1E-4*EP*3.1415927*R0*R0
ANTYPE, STATIC

SELTOL, 2E-12
```

```
CSYS, 1 !cylindrical coordinate system
NSEL, S, LOC, Y, 90 ! theta = 90 degree
DSYM, ASYMM, X

NSEL, S, LOC, Y, 0
DSYM, SYMM, Y

!bottom
NSEL, S, LOC, Z, LL
D, ALL, UZ, 0
!D, ALL, UX, 0

NSEL, S, LOC, X, RR
D, ALL, ALL, 0 !fix all nodes at the outer
cylindrical surface
!NSEL, S, LOC, x, RR
!NSEL, R, LOC, Y, 0
!D, ALL, UX, 0

ASEL, S, AREA, , 2
NSLA, S, 0 !only interior nodes
!NSEL, S, LOC, X, 0, R0
!NSEL, R, LOC, Y, 0
!NSEL, R, LOC, Z, 0
*GET, NX, NODE,,COUNT
F, ALL, FX, P0/NX/4

ALLSEL
SOLVE
FINISH

/POST1
CSYS, 0 ! back to cartesian coordinate system
write_ux
!PLDISP,1
FINISH
```

Appendix B

Mathematica (5.0) files for the proposed analytical solution

Calculation

Problem parameters

```
(* Ep = Rationalize[20*^9,0]; *)
(* R1= Rationalize[.76/2,0]; *)
R1 = 0; (* inner radius *)
R0 = 1/2; (* outer radius *)
νs = Rationalize[.3, 0];
Ip = π/4 (R0^4 - R1^4);
Gs = Rationalize[4.6*^6, 0];
(* GsStar=(1+3/4νs)Gs; *)
GsStar = Gs;
Es = 2 GsStar (1 + νs);
λs = 2 GsStar νs/(1 - 2 νs);
L = 50 * R0;
Kr = Rationalize[1*^-3, 0];
Ep = Kr Es L^4/Ip;
M0 = 0;
P0 = Rationalize[120*^3, 0];
(*
M0 = Rationalize[120*^3,0];
P0 = 0;*)
```

Iteration process

```
iter[ϒ_] := Module[{ξ, η, t1, t2, k, eqs, yz, y1, m, n},
  ξ = (BesselK[1, ϒ]^2 - BesselK[0, ϒ]^2)/(2 BesselK[0, ϒ]^2);
  η = -(ϒ^2 (BesselK[1, ϒ]^2 - BesselK[0, ϒ] BesselK[2, ϒ]))/(2 BesselK[0, ϒ]^2);
  t1 = (π R0^2 Gs)/(Ep Ip) ξ;
  t2 = (π R0^2 Gs)/(Ep Ip) (ξ + 1/2);
  k = (π (λs + 3 Gs))/(Ep Ip) η;
  Print["ξ = ", N[ξ, 6], ", η = ", N[η, 6],
   ", t1 = ", N[t1, 6], ", t2 = ", N[t2, 6], ", k = ", N[k, 6]];
  Clear[f];
  eqs = N[{f''''[z] - 2 t1 f''[z] + k f[z] == 0,
     f''[0] - M0/(Ep Ip) == 0, 2 t1 f'[0] - f'''[0] + P0/(Ep Ip) == 0,
     f''[L] == 0, f'''[L] - 2 t1 f'[L] - Sqrt[2 t2 k] f[L] == 0}, 200];
  (* Print[eqs]; *)
  y1[x_] = f[z] /. DSolve[eqs, f[z], z][[1]] /. z → x;
  m = (λs + 3 Gs) (∫_0^L y1[z]^2 dz + Sqrt[t2/(2 k)] (y1[L])^2);
  n = Gs (∫_0^L (y1'[z])^2 dz + Sqrt[k/t2] (y1[L])^2/(2 Sqrt[2]));
  Print["m = ", N[m, 6], ", n = ", N[n, 6]];
  m = Re[m];
  n = Re[n];
  {R0 Sqrt[2 n/m], y1[z], t1, t2, k}];

ϒ0 = 10;
```

```
ret = iter[γ0];
γn = ret[[1]];
While[Abs[(γn - γ0)/γ0] > 1*^-3 , γ0 = γn; ret = iter[γ0];
  γn = ret[[1]]; Print["γ0=", N[γ0, 10], ", γn=", N[γn, 10]];];
fz = ret[[2]];
tz1 = ret[[3]];
tz2 = ret[[4]];
kz = ret[[5]];
Print["γn = ", N[γn, 10]];
Print["y[z] = ", N[fz, 10]];
```

OVERALL CONCLUSION AND FUTURE WORK

1. SUMMARY AND CONCLUSION

In this study, fly ashes from four different sources were used to synthesize geopolymer mortars. Comprehensive experimental programs have been carried out to characterize the fly ashes, to examine the critical factors affecting on the mechanical properties of geopolymers, and to evaluate the potentials of four locally available fly ashes as source materials for geopolymers. The nonlinear fracture behavior of the fly ash-based geopolymer has been studied using splitting wedge testing and digital image correlation technique. To gain fundamental understanding of the geopolymerization process, the electrical properties of thegeopolymers are studied. Carbon nanotubes (CNTs) are explored in theory to toughen brittle material such as geopolymer. The following major summary and conclusions can be made based on this dissertation research:

1. Although the same mix design based on the chemical compositions of fly ashes from four different sources was used; the produced geopolymers exhibited different mechanical properties, suggesting that mix design based on chemical composition is not sufficient for geopolymers. This is because fly ashes from different sources can have different reactivity.
2. In order to account for the reactivity of fly ash into mix design, the dissolution degree of fly ashes were measured to determine the effective chemical compositions of each fly ash which participate in the geopolymerization process. By comparing with XRD

analysis, the dissolution testing underestimates the real dissolution degree of some fly ash due to new precipitants and reaction products have been produced during the dissolution testing.

3. At the same chemical composition, the geopolymer made of the fly ash from Gaston has achieved best mechanical properties because it has highest dissolvable reactive content.
4. The compressive strengths of geopolymer specimens increase with age during the whole testing period, suggesting geopolymerization takes a very long time.
5. The fracture of the geopolymer mortar follows a nonlinear behavior similar to the OPC based concrete. A fracture process zone (FPZ) was detected by the full-field displacement measurement existing ahead of the major crack. By inverse analysis, a bi-linear law was retrieved for this FPZ of the geopolymer.
6. The fracture energy of the geopolymer mortar is lower than that of the OPC-based concrete with similar strength.
7. Electrical properties measurement provides an effective way to examine the geopolymerization process. Both the magnitude of the electrical impedance and the electrical resistance increase monotonously with the curing time, suggesting that they can be used as an indicator of the degree of geopolymerization. The bulk resistance or the diameters of the high frequency arcs of all geopolymers increase with age over one year, suggesting that the polymerization is a very long process, similar to the hydration process of Portland cement. The bulk electrical resistance of geopolymers at the late age is at least two orders of magnitudes higher than at the early age.

The analytical model on the shear stress transfer between CNTs and matrix agrees very well with FEA on the lateral stress distribution along the CNT and within the matrix, and

the deflection of the CNT. There exists an effective length of the CNT within which the shear stress transfer occurs. No or little shear force transfer occurs out of this effective length. Shear stress transfer is more efficient when the Young's modulus of the matrix is closer to that of the CNT.

2. FUTURE WORK

The biggest challenge facing the application of fly ash-based geopolymer is lacking of a standard mix design because of the variance in source material, fly ash. In this study, dissolution degree of the fly ash was used to measure the effective chemical composition. As shown before, this method is questionable. New precipitants and reaction products can be produced during the dissolution testing, leading to underestimation of the real dissolution degree of some fly ash. In the future, the dissolution testing procedure should be modified such that those precipitants and new reaction products can be removed from the residues. One possible way is to use strong acid to wash the residue so that calcium-related precipitant and reaction products can be dissolved. Some dissolvable crystalline products in the residue can be quantitatively determined using XRD analysis. In addition, this study only examined one concentration of NaOH. In the future, different concentration of NaOH solution should be used to examine how dissolution degree varies with the alkalinity.

The proposed fracture mechanics testing shows that it may provide an efficient way to study the size effect of geopolymers and other quasi-brittle materials. By using the DIC system to measure CODs at different locations, testing one fracture specimen is equivalent to testing multiple specimens with different crack sizes. Therefore, only one specimen is needed in this study to study the size effect of the fracture of quasi-brittle materials. In the future study, more tests should be carried out to verify this.

The frequency of electrical impedance measurement used in this study is too high so the low-frequency arc of the Nyquist plot was missed. In the future, this test should be carried out again using the appropriate frequency range to capture the low-frequency arc and the bulk resistance. It has been shown in OPC concrete study that the electrical impedance is related to the microstructure of the OPC-based concrete. This may apply to geopolymer too. Therefore, in the future, study should focus on linking the electrical properties to the microstructure development of geopolymers so that deeper insight of geopolymerization process can be obtained.

REFERENCES

ASCE. 2013. “ASCE, 2013 Report Card for America’s Infrastructure.” http://www.infrastructurereportcard.org/a/documents/2013-Report-Card.pdf.

ASTM. 2005. “Specification for Coal Fly Ash and Raw or Calcined Natural Pozzolan for Use in Concrete”. ASTM International.

BAINES, J. 1994. “Ancient Egyptian Concepts and Uses of the Past: 3rd to 2nd Millennium BC Evidence.” *Who Needs the Past?: Indigenous Values and Archaeology*, 131.

Bakharev, T. 2005a. “Resistance of Geopolymer Materials to Acid Attack.” *Cement and Concrete Research* 35 (4): 658–70.

Bakharev, T. 2005b. “Durability of Geopolymer Materials in Sodium and Magnesium Sulfate Solutions.” *Cement and Concrete Research* 35 (6): 1233–46.

Balaguru, P. 1998. “Geopolymer for Protective Coating of Transportation Infrastructures.”

Boxley, C., B. Nair, and P. Balaguru. 2008. “Practical Applications of Geopolymers.” In *Developments in Porous, Biological and Geopolymer Ceramics: A Collection of Papers Presented at the 31st International Conference on Advanced Ceramics and Composites, January 21-21, 2007, Daytona Beach, Florida*, 321.

Cheng, T. W., and J. P. Chiu. 2003. “Fire-Resistant Geopolymer Produced by Granulated Blast Furnace Slag.” *Minerals Engineering* 16 (3): 205–10.

Chindaprasirt, P., T. Chareerat, S. Hatanaka, and T. Cao. 2010. “High Strength Geopolymer Using Fine High Calcium Fly Ash.” *Journal of Materials in Civil Engineering* 1 (1): 134.

Chindaprasirt, P., T. Chareerat, and V. Sirivivatnanon. 2007. “Workability and Strength of Coarse High Calcium Fly Ash Geopolymer.” *Cement and Concrete Composites* 29 (3): 224–29.

Davidovits, J. 1989. “Geopolymers and Geopolymeric Materials.” *Journal of Thermal Analysis* 35 (2): 429–41.

Davidovits, J. 1991. “Geopolymers.” *Journal of Thermal Analysis* 37 (8): 1633–56.

Davidovits, J., and M. Morris. 1988. *The Pyramids: An Enigma Solved*. Hippocrene Books.

Davidovits, Joseph. 2008a. *Geopolymer Chemistry and Applications*. Geopolymer Institute.

Davidovits, Joseph. 2008b. *They Built the Pyramids*. Geopolymer Institute.

Duxson, P., A. Fernández-Jiménez, J. Provis, G. Lukey, A. Palomo, and J. Deventer. 2007. "Geopolymer Technology: The Current State of the Art." *Journal of Materials Science* 42 (9): 2917–33.

Duxson, P., S.W. Mallicoat, G.C. Lukey, W.M. Kriven, and J.S.J. van Deventer. 2007. "The Effect of Alkali and Si/Al Ratio on the Development of Mechanical Properties of Metakaolin-Based Geopolymers." *Colloids and Surfaces A: Physicochemical and Engineering Aspects* 292 (1): 8–20.

Duxson, Peter, and John L. Provis. 2008. "Designing Precursors for Geopolymer Cements." *Journal of the American Ceramic Society* 91 (12): 3864–69.

Duxson, Peter, John L. Provis, Grant C. Lukey, Seth W. Mallicoat, Waltraud M. Kriven, and Jannie S.J. van Deventer. 2005. "Understanding the Relationship between Geopolymer Composition, Microstructure and Mechanical Properties." *Colloids and Surfaces A: Physicochemical and Engineering Aspects* 269 (1-3): 47–58.

Fernández-Jiménez, A., A. Palomo, and M. Criado. 2005. "Microstructure Development of Alkali-Activated Fly Ash Cement: A Descriptive Model." *Cement and Concrete Research* 35 (6): 1204–9.

Fernández-Jiménez, A., A. Palomo, I. Sobrados, and J. Sanz. 2006. "The Role Played by the Reactive Alumina Content in the Alkaline Activation of Fly Ashes." *Microporous and Mesoporous Materials* 91 (1-3): 111–19.

Fletcher, Ross A., Kenneth J.D. MacKenzie, Catherine L. Nicholson, and Shiro Shimada. 2005. "The Composition Range of Aluminosilicate Geopolymers." *Journal of the European Ceramic Society* 25 (9): 1471–77.

Giancaspro, James, P. N. Balaguru, and Richard E. Lyon. 2006. "Use of Inorganic Polymer to Improve the Fire Response of Balsa Sandwich Structures." *Journal of Materials in Civil Engineering* 18 (3): 390–97.

Granizo, M. L, S. Alonso, M. T Blanco-Varela, and A. Palomo. 2002. "Alkaline Activation of Metakaolin: Effect of Calcium Hydroxide in the Products of Reaction." *Journal of the American Ceramic Society* 85 (1): 225–31.

Hajimohammadi, Ailar, John L. Provis, and Jannie S. J. van Deventer. 2008. “One-Part Geopolymer Mixes from Geothermal Silica and Sodium Aluminate.” *Industrial & Engineering Chemistry Research* 47 (23): 9396–9405.

Hardjito, D., S. E Wallah, D. Sumajouw, and B. V. Rangan. 2004. “Factors Influencing the Compressive Strength of Fly Ash-Based Geopolymer Concrete.” *Civil Engineering Dimension* 6 (2).

Harrell, J. A, and B. E Penrod. 1993. “The Great Pyramid Debate-Evidence from the Lauer Sample.” *Journal of Geological Education* 41: 358–358.

Khale, Divya, and Rubina Chaudhary. 2007. “Mechanism of Geopolymerization and Factors Influencing Its Development: A Review.” *Journal of Materials Science* 42 (3): 729–46.

Koloušek, David, Jiri Brus, Martina Urbanova, Jana Andertova, Vaclav Hulinsky, and Jindřich Vorel. 2007. “Preparation, Structure and Hydrothermal Stability of Alternative (sodium Silicate-Free) Geopolymers.” *Journal of Materials Science* 42 (22): 9267–75.

Kong, Daniel L.Y., Jay G. Sanjayan, and Kwesi Sagoe-Crentsil. 2007. “Comparative Performance of Geopolymers Made with Metakaolin and Fly Ash after Exposure to Elevated Temperatures.” *Cement and Concrete Research* 37 (12): 1583–89.

Li, Chao, Henghu Sun, and Longtu Li. 2010. “A Review: The Comparison between Alkali-Activated Slag (Si + Ca) and Metakaolin (Si + Al) Cements.” *Cement and Concrete Research* 40 (9): 1341–49.

Pacheco-Torgal, Fernando, João Castro-Gomes, and Said Jalali. 2008. “Alkali-Activated Binders: A Review. Part 2. About Materials and Binders Manufacture.” *Construction and Building Materials* 22 (7): 1315–22.

Palomo, A., M. W. Grutzeck, and M. T. Blanco. 1999. “Alkali-Activated Fly Ashes: A Cement for the Future.” *Cement and Concrete Research* 29 (8): 1323–29.

Perera, Dan S., Zaynab Aly, Eric R. Vance, and Masahiro Mizumo. 2005. “Immobilization of Pb in a Geopolymer Matrix.” *Journal of the American Ceramic Society* 88 (9): 2586–88.

Phair, John W. 2006. “Green Chemistry for Sustainable Cement Production and Use.” *Green Chemistry* 8 (9): 763.

Provis, John L., Grant C. Lukey, and Jannie S. J. van Deventer. 2005. “Do Geopolymers Actually Contain Nanocrystalline Zeolites? A Reexamination of Existing Results.” *Chemistry of Materials* 17 (12): 3075–85.

Puertas, F., S. Martínez-Ramírez, S. Alonso, and T. Vázquez. 2000. “Alkali-Activated Fly Ash/slag Cements: Strength Behaviour and Hydration Products.” *Cement and Concrete Research* 30 (10): 1625–32.

Rowles, M., and B. O’Connor. 2003. “Chemical Optimisation of the Compressive Strength of Aluminosilicate Geopolymers Synthesised by Sodium Silicate Activation of Metakaolinite.” *Journal of Materials Chemistry* 13 (5): 1161–65.

Roy, Della M. 1999. “Alkali-Activated Cements Opportunities and Challenges.” *Cement and Concrete Research* 29 (2): 249–54.

Shi, Caijun, and Robert L. Day. 1995. “A Calorimetric Study of Early Hydration of Alkali-Slag Cements.” *Cement and Concrete Research* 25 (6): 1333–46.

Shi, Caijun, P. V. Krivenko, and D. M. Roy. 2006. *Alkali-Activated Cements and Concretes*. Taylor & Francis.

Silva, P. De, K. Sagoe-Crenstil, and V. Sirivivatnanon. 2007. “Kinetics of Geopolymerization: Role of Al_2O_3 and SiO_2.” *Cement and Concrete Research* 37 (4): 512–18.

Sindhunata, J. S. J. van Deventer, G. C. Lukey, and H. Xu. 2006. “Effect of Curing Temperature and Silicate Concentration on Fly-Ash-Based Geopolymerization.” *Industrial & Engineering Chemistry Research* 45 (10): 3559–68.

Songpiriyakij, Smith, Teinsak Kubprasit, Chai Jaturapitakkul, and Prinya Chindaprasirt. 2010. “Compressive Strength and Degree of Reaction of Biomass- and Fly Ash-Based Geopolymer.” *Construction and Building Materials* 24 (3): 236–40.

Sun, Peijiang. 2005. “Fly Ash Based Inorganic Polymeric Building Material”. United States -- Michigan: Wayne State University.

Temuujin, Jadambaa, Amgalan Minjigmaa, William Rickard, Melissa Lee, Iestyn Williams, and Arie van Riessen. 2009. “Preparation of Metakaolin Based Geopolymer Coatings on Metal Substrates as Thermal Barriers.” *Applied Clay Science* 46 (3): 265–70.

Van Jaarsveld, J. G. S., and J. S. J. van Deventer. 1999. “Effect of the Alkali Metal Activator on the Properties of Fly Ash-Based Geopolymers.” *Industrial & Engineering Chemistry Research* 38 (10): 3932–41.

Van Jaarsveld, J. G. S., J. S. J. van Deventer, and L. Lorenzen. 1997. “The Potential Use of Geopolymeric Materials to Immobilise Toxic Metals: Part I. Theory and Applications.” *Minerals Engineering* 10 (7): 659–69.

Van Jaarsveld, J. G. S., J. S. J. van Deventer, and G. C. Lukey. 2003. "The Characterisation of Source Materials in Fly Ash-Based Geopolymers." *Materials Letters* 57 (7): 1272–80.

Van Oss, Hendrik G., and Amy C. Padovani. 2003. "Cement Manufacture and the Environment Part II: Environmental Challenges and Opportunities." *Journal of Industrial Ecology* 7 (1): 93–126.

Varela, B., and N. Privorotskaya. 2005. "The Use of Geopolymers as Concrete Coatings for Fire Protection." In *Geopolymer, Green Chemistry and Sustainable Development Solutions: Proceedings of the World Congress Geopolymer 2005*, 209.

Verner, M., and S. Rendall. 2002. *The Pyramids: The Mystery, Culture, and Science of Egypt's Great Monuments*. Grove Pr.

Wallah, Steenie Edward. 2009. "Drying Shrinkage of Heat-Cured Fly Ash-Based Geopolymer Concrete." *Modern Applied Science* Vol. 3 (12): 14–21.

Winnefeld, Frank, Andreas Leemann, Martin Lucuk, Pavel Svoboda, and Markus Neuroth. 2010. "Assessment of Phase Formation in Alkali Activated Low and High Calcium Fly Ashes in Building Materials." *Construction and Building Materials* 24 (6): 1086–93.

Xu, H., J. S. J. van Deventer, and G. C. Lukey. 2001. "Effect of Alkali Metals on the Preferential Geopolymerization of Stilbite/Kaolinite Mixtures." *Industrial & Engineering Chemistry Research* 40 (17): 3749–56.

Yip, C. K., and J. S. J. van Deventer. 2003. "Microanalysis of Calcium Silicate Hydrate Gel Formed within a Geopolymeric Binder." *Journal of Materials Science* 38 (18): 3851–60.

Yip, C.K., G.C. Lukey, and J.S.J. van Deventer. 2005. "The Coexistence of Geopolymeric Gel and Calcium Silicate Hydrate at the Early Stage of Alkaline Activation." *Cement and Concrete Research* 35 (9): 1688–97.

Zhang, Jianguo, John L. Provis, Dingwu Feng, and Jannie S.J. van Deventer. 2008. "Geopolymers for Immobilization of Cr^{6+}, Cd^{2+}, and Pb^{2+}." *Journal of Hazardous Materials* 157 (2-3): 587–98.

Zhang, Zuhua, Xiao Yao, and Huajun Zhu. 2010. "Potential Application of Geopolymers as Protection Coatings for Marine Concrete: I. Basic Properties." *Applied Clay Science* 49 (1-2): 1–6.